STUDIES RELATED TO THE EFFECT OF FRICTION STIR WELDING ON THE MECHANICAL PROPERTIES AND MICROSTRUCTURE DEVELOPMENT IN SINGLE SIDE WELDING ON ALUMINIUM ALLOY 5083

Teză destinată obţinerii
titlului ştiinţific de doctor inginer
la
Universitatea Politehnica Timişoara
în domeniul INGINERIE CIVILĂ
de către

Ing. Horia Florin Daşcău

Conducător ştiinţific: prof.univ.dr.ing. Radu Băncilă
prof.univ.dr.ing. Aleksandar Sedmak
Referenţi ştiinţifici: prof.univ.dr.ing. Vencislav Grabulov
c.s.l. dr.ing. Doru Romulus Pascu
conf.dr.ing. Edward Petzek

Ziua susţinerii tezei: 17.04.2015

Seriile Teze de doctorat ale UPT sunt:

1. Automatică
2. Chimie
3. Energetică
4. Ingineria Chimică
5. Inginerie Civilă
6. Inginerie Electrică
7. Inginerie Electronică şi Telecomunicaţii
8. Inginerie Industrială
9. Inginerie Mecanică
10. Ştiinţa Calculatoarelor
11. Ştiinţa şi Ingineria Materialelor
12. Ingineria sistemelor
13. Ingineria Energetică
14. Calculatoare şi tehn. informaţiei
15. Ingineria materialelor
16. Inginerie și management
17. Arhitectură
18. Inginerie civilă și instalații

Universitatea Politehnica din Timişoara a iniţiat seriile de mai sus în scopul diseminării expertizei, cunoştinţelor şi rezultatelor cercetărilor întreprinse în cadrul şcolii doctorale a universităţii. Seriile conţin, potrivit H.B.Ex.S Nr. 14 / 14.07.2006, tezele de doctorat susţinute în universitate începând cu 1 octombrie 2006.

România, 300159 Timişoara, Bd. Republicii 9,
tel. 0256 403823, fax. 0256 403221
e-mail: editura@edipol.upt.ro

Cuvânt înainte

Teza de doctorat a fost elaborată pe parcursul activităţii mele în cadrul Departamentului de Construcţii Metalice şi Mecanica Construcţiilor al Facultăţii de Construcţii din Universitatea „Politehnica” din Timişoara.

Doresc pe această cale să aduc mulţumirile mele şi profundă recunoștință d-lui. Prof. Dr. Ing. Radu Băncilă şi d-lui Prof. Dr. Ing. Aleksandar Sedmak, conducători ştiinţifici ai prezentei teze de doctorat. De asemenea le sunt recunoscător pentru generozitatea cu care mi-au îndrumat cercetarea, pentru materialul bibliografic pe care mi l-au pus la dispoziţie, pentru indicaţiile competente pe care mi le-au oferit, izvorâte dintr-o inegalabilă experienţă şi valoare, cât şi pentru susţinerea lor în definitivarea acestei teze.

De asemenea doresc să mulțumesc d-lui Ing. Radu Cojocaru pentru sfaturile prețioase din timpul cercetării mele, cât şi pentru documentația care mi-au pus-o la dispoziție.

Mulţumesc referenţilor ştiinţifici Prof. Dr. Ing. Vencislav Grabulov, c.s. I. Dr. Ing. Doru Romulus Pascu şi Conf. Dr. Ing. Edward Petzek pentru acceptul dânşilor de a recenza teza de doctorat şi pentru recomandările făcute.

Le sunt recunoscătoare colegilor din departamentul CMMC că m-au primit şi acceptat în rândul lor, şi o deosebită recunoştinţă am pentru colega mea Dr. Ing. Anamaria Feier fără de care nu aş fi reuşit să rezolv problemele organizatorice.

Nu în ultimul rând doresc să mulţumesc şi familiei mele, care m-a susţinut şi m-a încurajat în realizarea şi, mai ales, în finalizarea tezei.

Timişoara, Aprilie, 2015 Ing. Horia Florin DAŞCĂU

Dașcău, Horia Florin

Studies related to the effect of friction stir welding on the mechanical properties and microstructure development in single side welding on aluminium alloy 5083

Teze de doctorat ale UPT, Seria 5, Nr. 134, Editura Politehnica, 2015, 130 pagini, 119 figuri, 34 tabele.

ISSN: 1842-581X

ISBN: 978-606-554-942-5

Cuvinte cheie: friction stir welding, aluminium alloy, numerical simulation, microstructure, crack propagation, welding parameters, fracture toughness, fatigue crack growth,

Rezumat,
Sudabilitatea şi rezistenţa la oboseală a structurilor sudate din aliaje de aluminiu, realizate prin sudare cu element activ rotitor reprezintă o caracteristică esențială pentru durata de viață a unei structuri. Analiza acestei sudabilități și predicția duratei de viață nu este reglementată în cadrul Eurocodului 9 decât pentru 2 procedee de sudare și pentru sudarea longitudinală. Obiectivul principal al acestei teze îl constituie realizarea unei analize referitoare la posibilitatea sudării în condiţii cât mai bune a aliajului de aluminiu 5083, astfel încât construcțiile realizate să poată beneficia de o durată mai mare de funcționare în condițiile unor tensiuni interne de valoare cât mai redusă. Se prezintă aspecte importante cu privire la parametrii esenţiali care trebuie luaţi în considerare la sudarea materialelor feroase sau neferoase. Aceste aspecte sunt în directă relaţie cu durata de viaţă şi probabilitatea de avarie a unor elemente structurale realizate în construcţie sudată şi trebuie corelate cu metode corespunzătoare de inspecţie, pentru un control al calităţii cât mai eficient. A fost de asemenea analizată influența unghiului pe care pin-ul elementului activ rotitor îl poate avea asupra microstructurii îmbinării sudate şi s-a analizat energia de propagare a fisurii relativ la energia de iniţiere a procesului de fisurare. Simularea numerică a avut în vedere şi 2 tipuri de pin pentru sudarea FSW, fiind analizată distribuţia căldurii în pin şi în materialul de bază. Simulările au avut în vedere modele 3D utilizarea metodei eXtended Finite Element Method (XFEM) şi a funcţiilor Heaviside, corelat cu utilizarea funcţiilor lui Dirichlet pentru condiţiile de limită. Simularea a fost realizată utilizând un software de tip ABAQUS, în cadrul Universităţii Tehnice din Belgrad.

Cuprins

Lista de tabele

Lista de figuri

1 INTRODUCTION

1.1 Friction Stir Welding (FSW)

Friction stir welding (FSW) is a relatively new joining process, invented in 1991, [1]. It is very energy efficient, environment friendly and versatile, and also especially suitable for "difficult" Al alloys [2]. It can used to join aluminum sheets and plates without filler wire or shielding gas, in large range of thickness. Anyhow, there is still a lack of design data and understanding of the failure mechanisms, [3,4].

In friction stir welding a pin connected to a shoulder is rotated and slowly plunged into the joint line between two pieces of sheet or plate material, which are butted together (fig.1-1), although T joint can be welded as well. The parts are firmly clamped to prevent abutting joint faces from being moved apart.

Frictional heat is generated between a wear resistant welding tool (fig. 1-2) and material to be welded. This heat causes the material to soften without reaching the melting point, while the tool translates along the weld line. Plastically deformed material is transferred from the leading edge of the tool to the trailing edge of the tool probe and is forged by the intimate contact of the tool shoulder and the pin profile, leaving a solid phase bond between the two pieces, [5].

Friction stir welding presents several benefits for joining of various alloys, especially of aluminum alloys. One of the significant advantages of FSW is that the process is entirely going on in the solid state. The heat inputs are smaller than in fusion welding processes, including resistance welding. Joining is done at temperature that eliminates the major problems of conventional welding processes, including dissolution of atmospheric gases in the melted material of the joint. The elimination of cracking in the weld fusion and heat affected zones (HAZ), weld porosity, filler material and costly weld preparation are also advantages of FSW. Therefore, materials such as Al alloys that cannot be welded by fusion processes (Al2024 T351) are easily welded by FSW.

On the other hand, FSW has some drawbacks: slower traverse rate than most fusion welding processes can cause exit hole left when tool is withdrawn, it imposes additional requirements on the construction of welding machines, clamping of jointed parts is needed, as well as special design of tools.

Although FSW is performed in solid state, thus avoiding hot cracking and other problems related to melting, there are still some issues with different microstructural features, indicated in fig. 1-3:

A – the nugget zone, also known as the dynamically recrystallized zone,
B – the thermo- mechanically affected zone (TMAZ),
C – the heat affected zone (HAZ),
D – The nugget zone is the region through which the tool piece pin passes.

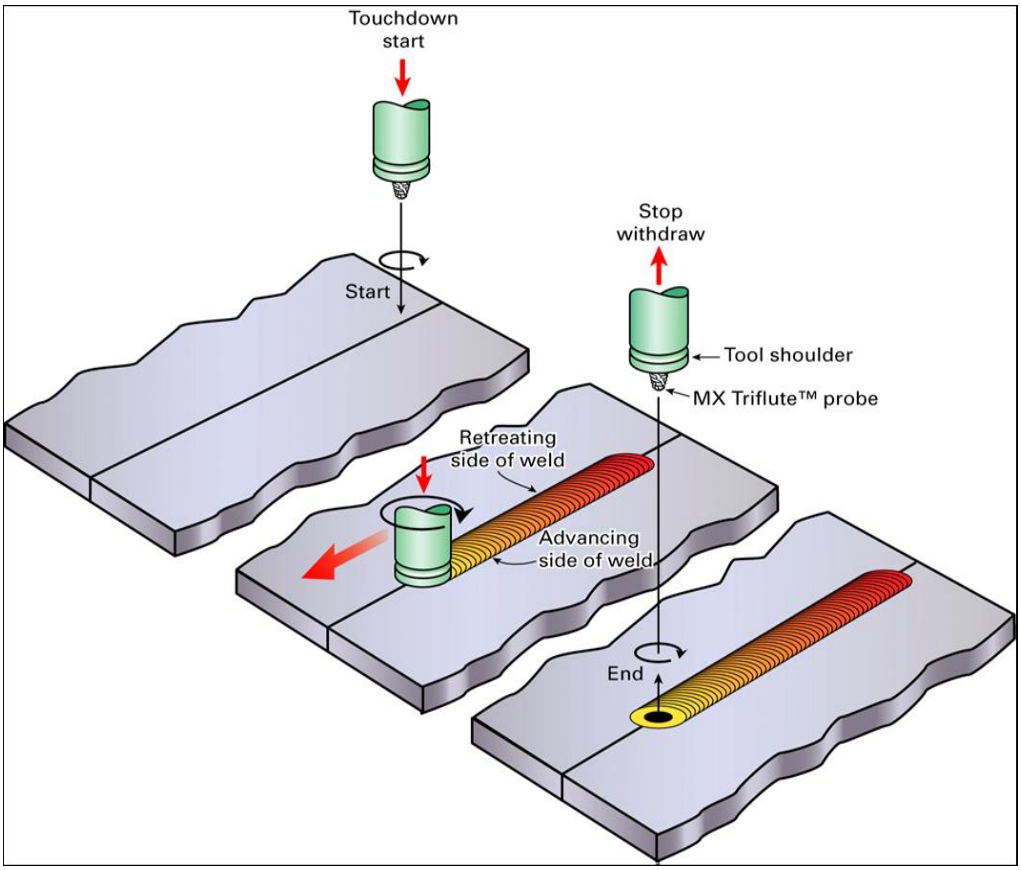

Figure 1—1 Explanation of the Friction Stir Welding Process, [5]

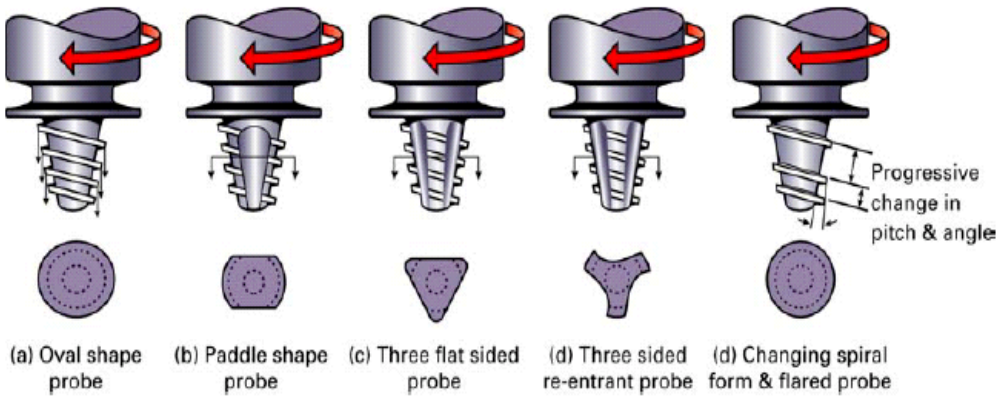

Figure 1—2 Tools of Various Geometry Used in FSW, [5]

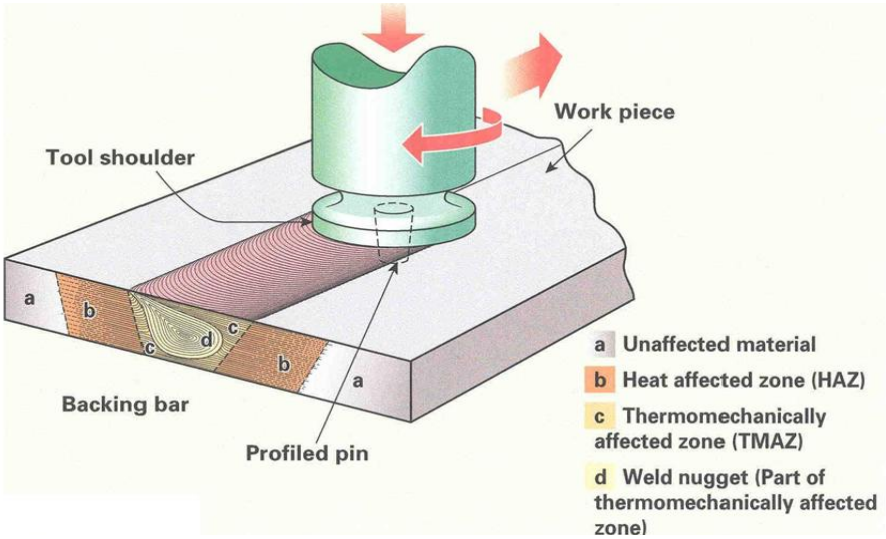

Figure 1—3 Micro-structural feature of FSW, [6]

1.2 Heat generation

In FSW a cylindrical tool, with shoulder and profiled threaded/unthreaded probe or pin assembly, is rotated with high rotation constant speed and plunged between the two pieces of material to be welded. The pin is slightly shorter than the weld depth and the tool shoulder should be in intimate contact with the surface, as shown Fig.1-4(a-c). After the plunge phase is completed, the tool translates along the welding line, at the constant rate, producing the welded joint, Fig.1-4d.

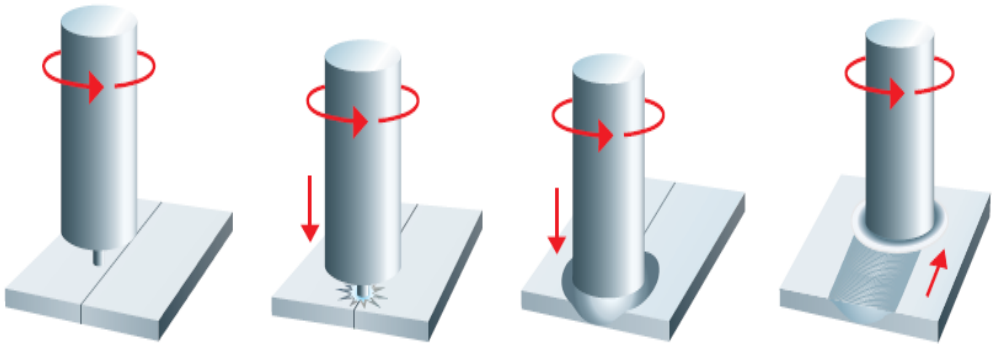

a) b) c) d)

Figure 1—4 Friction stir welding operation, [7]

The frictional heat generated by the welding tool makes the surrounding material softer, enabling the tool to translate along the welding line. The softened material starts to flow around probe, allowing the traversing of the tool along the welding line in a plastically deformed tubular shaft of material. If the pin is moved in

direction of welding, its leading face, assisted by a special pin profile, forces plasticized material to the back of the pin, applying a substantial forging force to form the weld metal at the same time. Stirring action by the rotating tool makes intensively deformed region in the material.

1.2.1 Heat Generations during FSW of Al 5083

Heat generation is a complex process of transformation of energy into heat. During friction stir welding, one part of mechanical energy delivered to the welding tool is consumed in the welding process, another is used for deformation processes and the rest of energy is transformed into heat. The heat generation in FSW can be separated into two parts: frictional heat generated by the tool and heat generated by material deformation near the pin and the tool shoulder region, [14]. The maximum temperature during FSW can be represented by the following equation:

$$\frac{T}{T_m} = k\left(\frac{\omega^2}{v\times 10^4}\right)^{\alpha} \qquad (1.1)$$

where: T is the maximum FSW temperature (^{0}C), T_m is the melting temperature of the material (^{0}C), α is the coefficient in the range from 0.04 to 0.06, k is the material constant, typical values between 0.65 to 0.75, ω is the tool rotational, and *v* is the welding speed. Figure (1-5) shows the relationship between the rotational speed and maximum temperature, whereas the relationship between the traversing speed and the maximum temperature is shown in figure (1-6), obtained by using eq. 1.1, [8].

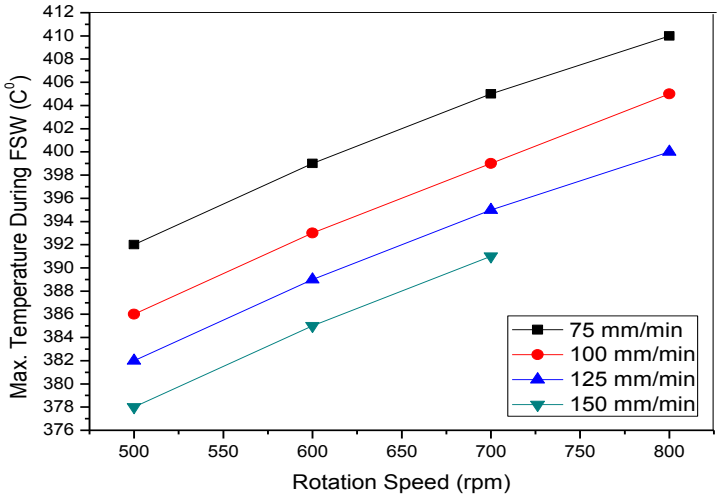

Figure 1—5 The relationship between the rotation speed and max. temperature, [8]

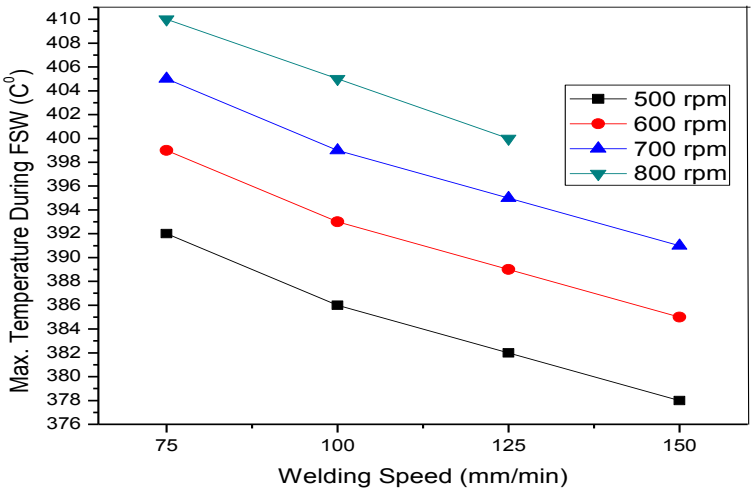

Figure 1—6 The relationship between the welding speed and max. temperature, [8]

Temperature measurements during FSW of aluminum alloys have shown that the process is a solid-state welding process, with T_{max} between 400 and 550 °C for pure aluminum alloy. Temperature T_{max} is observed under the shoulder, where the maximum heat flux exists. Based on the thermocouple measurements, it can be concluded that the temperatures generated are not strongly influenced by the alloy type [9].

1.3 Weld Zones

Threadgill has classified welds into four microstructural zones, as described in [10] and shown in Fig. 1-7, [11]: a) weld nugget (WN), consisting of fine equated grains due to recrystallization b) thermomechanically affected zone (TMAZ), c) heat affected zone (HAZ), d) unaffected base metal (BM). The WN refers to the region previously occupied by the tool pin. The stirring action experienced within the TMAZ/WN leads to the formation of dynamically recrystallized grains in WN and plastically deformed or partially recrystallized grains in TMAZ. Beyond TMAZ, a typically narrow HAZ exists, where only a diminishing thermal-field is experienced until reaching the unaffected BM. Because of the rotation direction of the tool, the weld morphology is asymmetric with some differences between the advancing side and retreating side. Towards the advancing side, where the traverse speed and the tangential velocity component of the rotating tool are in the same direction, the TMAZ/HAZ boundary is sharper compared to the retreating side, where the boundary is more diffuse.

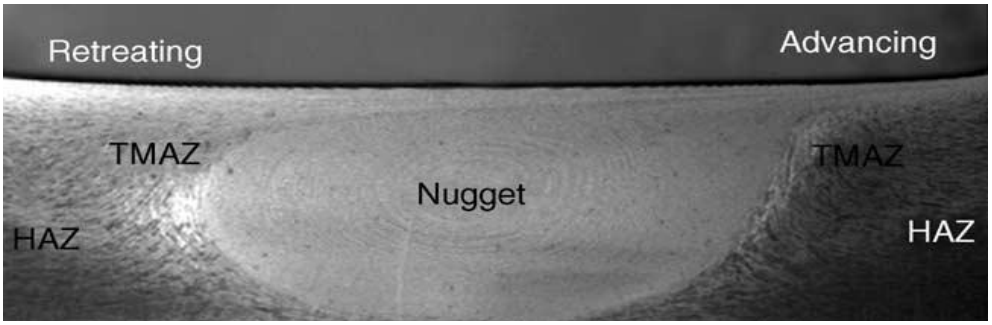

Figure 1—7 Microstructural zone classification in a friction stir weld, [11]

1.4 Advantages and drawbacks of FSW

The solid-state nature of FSW provides several advantages over fusion welding methods since there is no problem associated with cooling from the liquid phase. Therefore, problems such as porosity, solute redistribution, solidification cracking and liquation cracking are not an issue in FSW. In general, FSW produces low concentration of defects and is very tolerant to variations in parameters and materials. One can list a number of benefits of FSW:

- Improved safety due to absence of toxic fumes or the spatter of molten material and low environmental impact.
- No consumables such as filler metal and gas shield is required.
- Easily automated using simple milling machines, enabling lower set-up costs and less training.
- Possibility to weld in all positions (horizontal, vertical, etc.), from the point of view of non-existing weld pool.
- Generally good weld appearance and geometry, reducing the need for expensive machining after welding.

However, some drawbacks of the process have also been identified:

- Exit hole appears when tool is withdrawn.
- Large down forces required with heavy duty clamping necessary to hold the plates together.
- It is less flexible than manual and arc processes, including difficulties with thickness variations and non-linear welds.
- It provides slower traverse rate than some fusion welding techniques although this may be offset if fewer welding passes are required.

1.5 Aluminum alloy [AA5xxx]

The aluminum 5xxx alloy exhibits good corrosion resistance, even to seawater and the marine atmosphere, moderate mechanical properties and satisfying fatigue and fracture resistance. With the growth of aluminum within the welding fabrication industry, and its acceptance as an excellent alternative to

steel for many applications, there are increasing requirements for those involved with developing aluminum projects to become more familiar with this group of materials. To fully understand aluminum, one should become acquainted with the aluminum identification / designation system.

Aluminum alloys are divided into two closes according to the method of production: wrought and cast. The wrought category is a broad one, since aluminum alloys may be shaped by virtually every known process, including rolling, extruding, drawing, forging, and number of other, more specialized processes. Cast alloys are these that are poured molten into sand (sand casting) or high strength steel molds, and allowed to solidity to produce the desired shape. The wrought and cost alloys are quite different in properties; wrought alloys must be ductile, while cast alloys must have high fluidity. In 1974, the designation system for wrought aluminum alloys, according to major alloying elements, has been published, [12], and shown in Fig. 1-8, indicating weldability as well, [13].

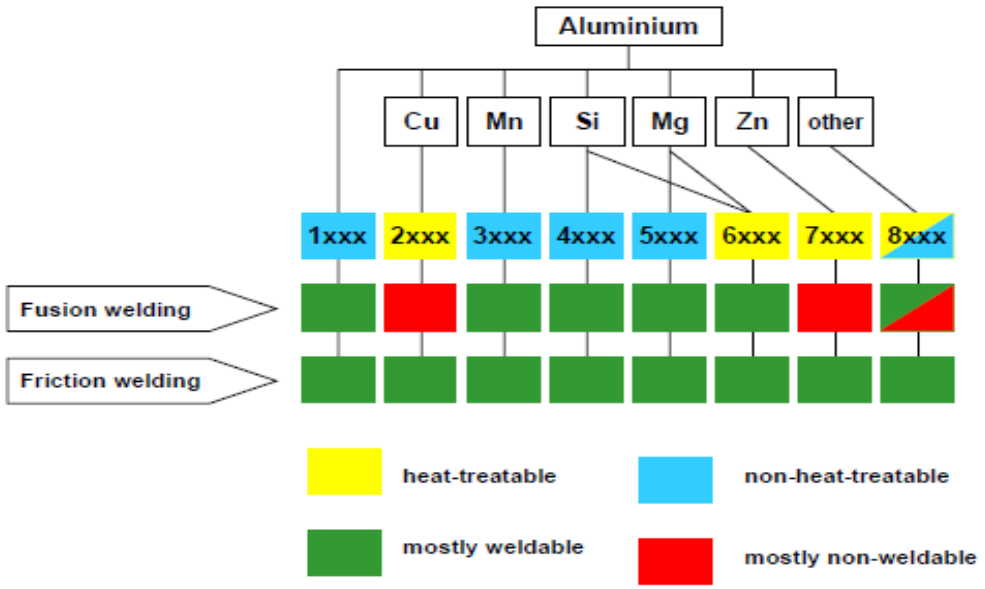

Figure 1—8 Weldability of various Aluminum alloys, [13]

1.5.1 Properties of Aluminum Alloys (AA5083)

The properties of representative group of wrought aluminum alloys are generally presented in two categories: non-heat-treatable and heat-treatable. Non-heat-treatable alloys are these that derive their strength from the hardening effect of elements such as manganese, iron, silicon, magnesium and are further strengthened by strain hardening. Typical chemical and mechanical properties are shown in tables 1-1 and 1-2.

Table 1-1 Chemical Composition of AA 5083

Mg	Mn	Cu	Fe	Si	Zn	Cr	Ti
4.5	0.7	0.02	0.3	0.15	0.05	0.01	0.025

Table 1-2 Mechanical Properties of AA5083 (non-deformed, standard values)

Property	Tensile strength, Rm (MPa)	Yield strength, $R_{0.2(}$MPa)	Elongation A (%)
Minimum	320	180	25

2 CONTRIBUTIONS TO THE DEVELOPMENT OF FRICTION STIR WELDING PROCESS

2.1 Introduction

Friction Stir Welding (FSW) is an innovative method of joining in solid state of materials at low temperatures, below the melting temperature. This allows joining of different types of metals with very different chemical, physical and mechanical properties and avoiding, in the same time, the intermetallic phase formation (undesirable) that normally occur during the fusion welding process.

Here some considerations of friction stir welded alloys, design and execution of machines and FSW welding tools, is presented, as well as the results obtained at ISIM Timisoara, representing own contributions to the development of FSW, as follows: FSW-TIG hybrid welding (welding is done by FSW and preheat of welding materials by TIG process); deposition of functional layers (aluminum alloys) on steel substrate, using the principle of FSW; monitoring of welding process in real time; T joints.

The problem of the developing of new joining processes for advanced material is present at horizontal level in the priority scientific and technological fields of research at the European level. As examples, one can think of those that aim the future fabrication processes, new materials, transports, aeronautic, inclusively, but also those related to the restructuring some of traditional industrial sectors, such as the steel industry and constructions.

The development of these fields impose special requirements to the joining processes from the technical point of view (materials, shapes, sizes, structures, loading), economical (productivity, consumption, cost) and environment (pollution, toxic fumes). The respective requirements, in continuous growth, cannot be entirely met by the welding processes used at present industrial level.

The innovative FSW welding process answers to these high requirements by its extraordinary potential for development.

The process developed rapidly, having a good grip on some prestigious research centers in the world, as well as on leading industrial companies in top sectors such as aerospace or land transport, [15]. Having these considerations as a basis, after Year 2000 the research of welding by the FSW process is included in the scientific program of the institute.

2.2 Performances/results obtained in FSW field

The evolution for researches and achievements in the FSW field can be structured according to the diagram presented in Figure 2-1.

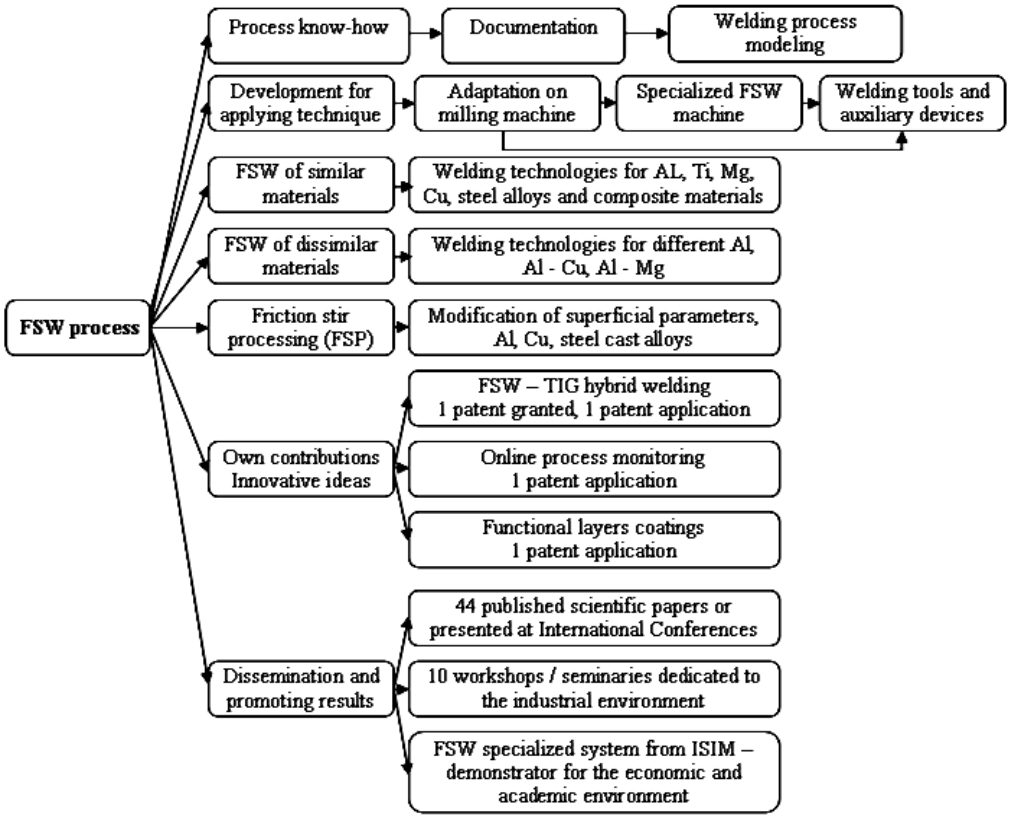

Figure 2—1 Scheme of achievements in FSW field

Preliminary experimental programs were conducted on a system with specific adjustments done for welding on a classic milling machine. The obtained results were considered as the base for the expansion and further research in this area.

Execution and commissioning of the specialized FSW machine in 2008, designing and execution some of specific welding tools, allowed the start of a wide and complex long term research program.

The entire research program in FSW field is based on the use of advanced materials such as aluminum, titanium and magnesium alloys, metallic matrix composite materials, copper alloys, steels, material combinations.

For FSW joining of these similar or dissimilar materials, optimum process parameters were determined and very good results were obtained.

Using the friction stir processing (FSP), the mechanism and effective conditions to modify the materials characteristics, at the micro scale, were studied. The investigation was made (with adapting of the process parameters) for the case of cast aluminum alloys and copper, of hard aluminum alloys and steel, and aimed aspects such as grains, eutectics distribution, hardness and porosity.

Also, experimentally, it was investigated the possibility of repair some of superficial defects such as cracks or pores in composite and cast materials.

Activities to disseminate and promote the results of researches were a very important objective and were focused mainly on the following directions:

- Knowledge, promotion and identifying the opportunities for application of FSW process in the Romanian industry.
- Use of complex technological FSW system, from ISIM Timisoara, as demonstrator for specific industrial applications.
- International visibility increased by publication or presentation at international conferences in the FSW field.
- Knowledge and promotion of the process in university environment by participating in conferences organized by the technical universities, but also through practical demonstrations, for students and masters.
- Protection of innovative ideas/original achievements at worldwide level in FSW field.

2.3 Innovative contributions to FSW development

The innovative character of ideas as own contributions have materialized in the granting of a patent and request for 3 more patent applications filed at OSIM.

2.3.1 FSW-TIG hybrid welding

TIG assisted friction stir welding method is a new FSW technique proposed by team of authors. TIG assisted friction stir welding, represent a development of FSW technique and create an hybrid welding process, in solid state, that integrates the preheating of plates through TIG welding process (figures 2-2 and 2-3).

Experiments were developed for materials that have difficulties at classic friction stir welding: aluminum alloy EN AW 7075-T651 (s1=5 mm), copper Cu 99 (s2=5 mm) and steel S235JR+N (s3=3 mm).

For welding of EN AW 7075-T651 welding tools having threaded cylindrical pin and smooth shoulder were used, made from X38CrMoV5 (AISI H11), heat treated to 52-54 HRC. For welding of copper and S235 steel welding tools having smooth conical pin and smooth shoulder were used, made from tungsten sintered carbides (P20S). Table 2-1 shows the technological parameters used in experimental program for each material.

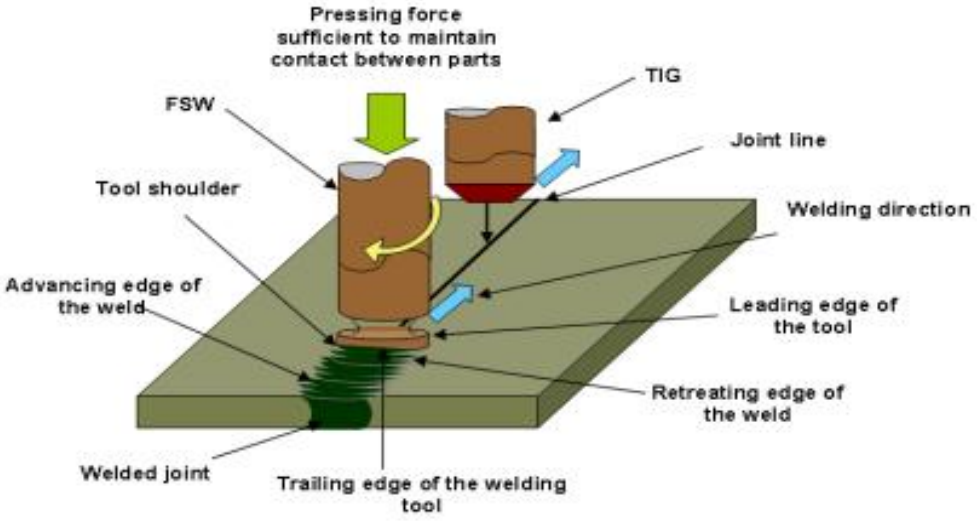

Figure 2—2 FSW-TIG scheme

Figure 2—3 FSW-TIG assembly

Table 2-1 Technological parameters

Welding materials	Procedure	Welding tools		Welding process parameters		
		Characteristics of pin	Caracteristics of shoulder	Rotation speed rot/min	Welding speed m/min	Sense of rotation
EN AW 7075	FSW	threaded cylindrical, M6 l_{pin}= 4,85 mm	smooth, $Ø_{shoulder}$=22 mm	1200	120	anti clockwise
	FSW-TIG			1000	200	
S 235 JR+N	FSW	smooth conical l_{pin}= 2,75 mm	smooth, $Ø_{shoulder}$=20 mm	800	20	
	FSW-TIG			800	100	
Cu 99	FSW	smooth conical l_{pin}= 4,80 mm	smooth, $Ø_{shoulder}$=20 mm	1000	100	clockwise
	FSW-TIG	smooth conical l_{pin}= 4,80 mm	smooth, $Ø_{shoulder}$=25 mm	1200	200	

Using optimized parameters for both methods, classical FSW and FSW-TIG, welded joints without imperfections/defects were obtained. Figure 2-4 shows the macroscopic images of welded joints, in transverse direction on movement direction of welding tool.

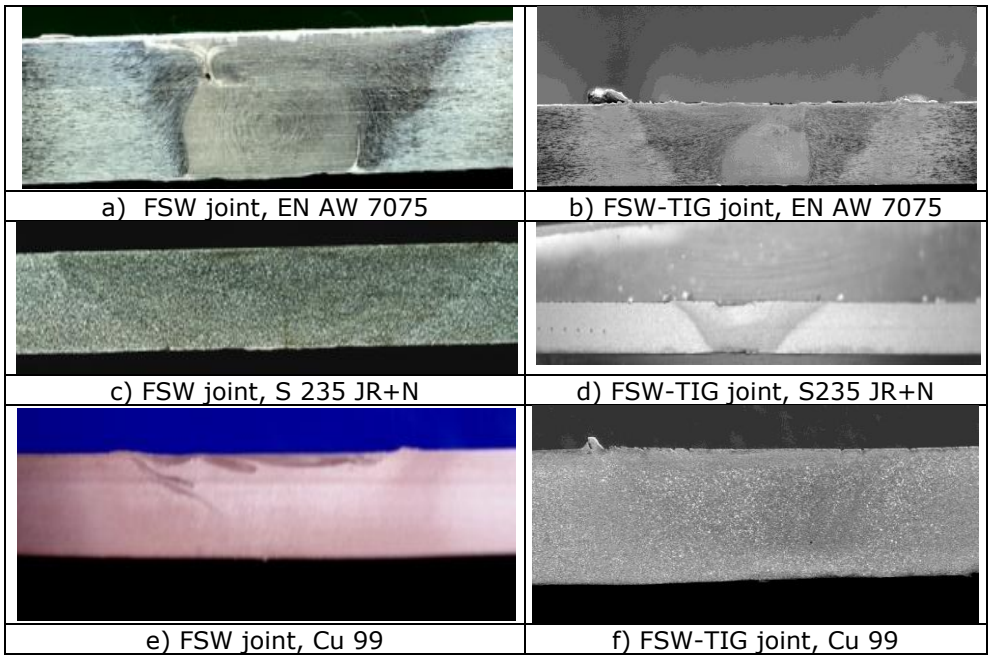

a) FSW joint, EN AW 7075 | b) FSW-TIG joint, EN AW 7075

c) FSW joint, S 235 JR+N | d) FSW-TIG joint, S235 JR+N

e) FSW joint, Cu 99 | f) FSW-TIG joint, Cu 99

Figure 2—4 Macroscopic aspects of welded joints

The mechanical characteristics of welded joints, for both procedures, are presented in table 2-2.

Table 2-2 Mechanical characteristics of welded joint

Material	Procedure	Strength resistance		Degree of deformation	HV5 (HV3) Hardness			
		Rm_{weld} / Rm_{MB}	Breaking place		BM	HAZ	TMAZ	N
EN AW 7075	FSW	0,77	TMAZ	maximum	160	~120	~160	~185
	FSW-TIG	0,75	TMAZ		160	~105	~120	~130
S 235 JR+N	FSW	-	BM		125	~115	~135	~120
	FSW-TIG	-	BM		125	~140	~150	~170
Cu 99	FSW	0,97	N		88	91	91	90
	FSW-TIG	0,98	N		88	90	90	88

At a comparative analyze of mechanical characteristics of FSW welded joints, respectively FSW-TIG, it can be observed that those are similarly, the small differences are negligible.

From point of view of proposed objectives through FSW-TIG welding procedure, following improvements in comparison with classical FSW, are obtained:

- increase of productivity through increasing of welding speed (at EN AW 7075 alloy with ~67 %, at S 235 steel with ~500% and copper Cu 99 with ~200%),
- more stable welding process (without vibrations) that ensure a better protection for machine and welding tools,
- welding tools wear significantly decreased at FSW-TIG hybrid welding, compared with classical FSW.

2.3.2 Deposition of functional layers (aluminum alloys) on steel substrate, using FSW principle

Deposition of functional layers that is a result of consuming of tool, is achieved by combination of three specific movement of welding tools: rotation, vertical translatory motion for ensuring of necessary fluxe of material that will be deposited and translatory movement along the substrate surface, effective formation of functional layer.

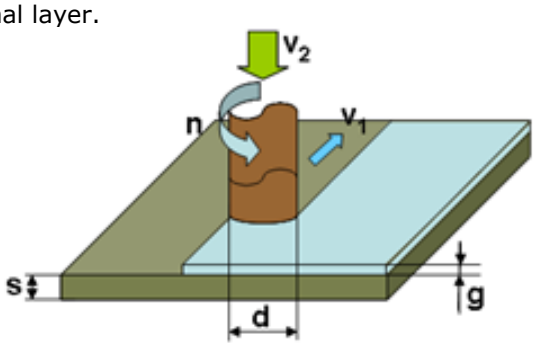

Figure 2—5 Scheme of deposition procedures

Figure 2—6 Deposition of functional layers

One important problem was designing of optimum geometries for consumable welding tools made from aluminum, that using the friction stir welding principle, to allow the generation of aluminum alloys layers on steel substrate:

- cylindrical tools having different diameters, figure 2-7a,
- tubular tools having different outside/inside diameters, figure 2-7b,
- conical tools, figure 2-7c,
- tools with eccentric having different diameters and different value of eccentricity, figure 2-7d.

a) b) c) d)

Figure 2—7 Consumable FSW tools

Tools having different physical and mechanical properties were made from aluminum alloys: EN AW 5086, EN AW 5083, EN AW 6061 and EN AW 7075.

In all experiments, to ensure fast heating of aluminum alloy and achieve the plasticizing temperature, high rotation speed of welding tools, between 1200-1300 rot/min, were used. Speed of movement on vertical direction for consumable tool, that ensure quantity of deposited material, was in range 20-30 mm/min, and speed of movement of tool on substrate surface was in range 60-200 mm/min.

Deposition in one or two layers, using EN AW 7050 material and tool having diameter Φ12 mm, is shown in figure 2-8.

a) one layer | b) two layers

Figure 2—8 Deposition of EN AW 7050, using tool having diameter Φ12mm

From all experiments, this was most stable, fact demonstrated by temperature evolution diagrams during process (figure 2-9).

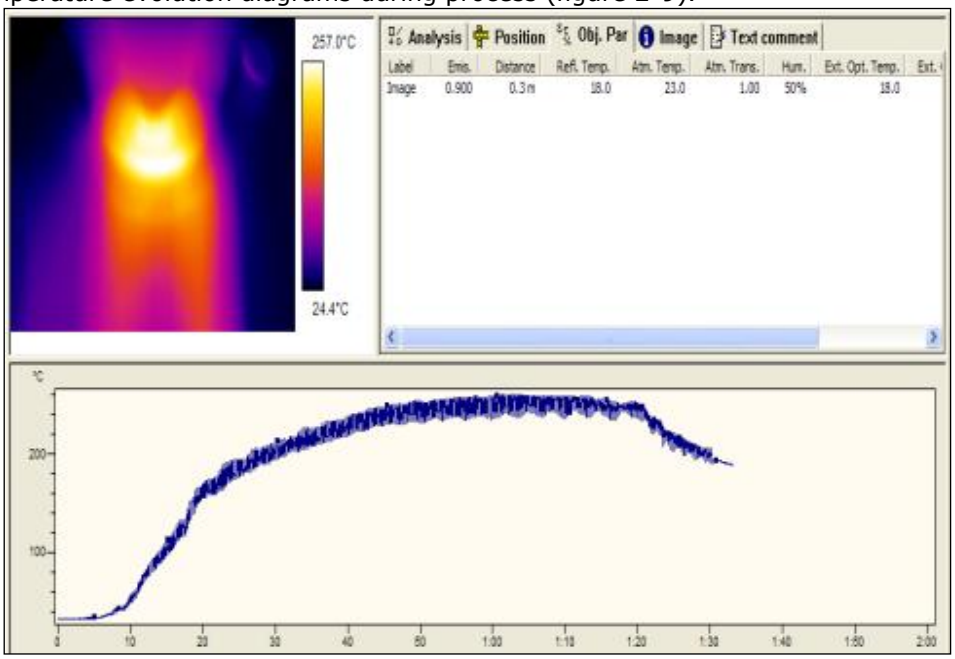

Figure 2—9 Temperature evolution during FSW deposition process, using tools having Φ20 mm, made from EN AW 5086 (v=200 mm/min)

Deposition of layers with thickness between s=1,1-1,5 mm were obtained. Macroscopic aspect of deposition is shown in figure 2-10. Microscopic structure of characteristic zones is presented in table 2-3 and figure 2-11.

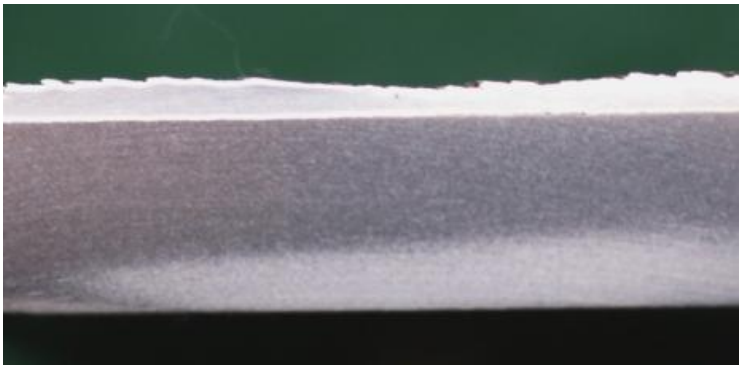

Figure 2—10 Macroscopic aspect of deposition

Table 2-3 Microscopic structure of deposited zone

Examinated zone	**Structure [100×]**	**Etching**
BM 1	Ferrite, pearlite	Nital 2%
HAZ	Ferrite, pearlite	Nital 2%
BM 2	Solide sollution Alα +$CuAl_2$ and fine non metallic inclusions	NaOH 5%

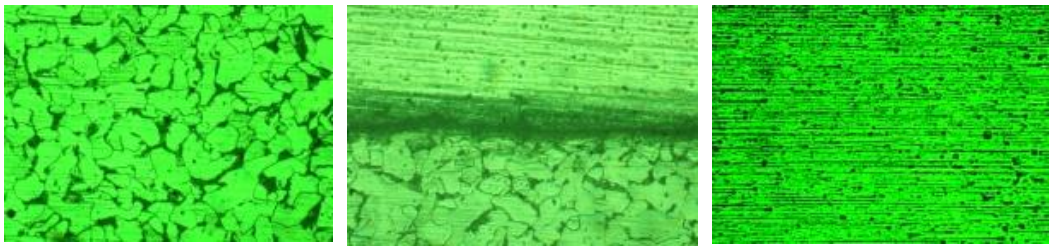

a) BM 1 b) HAZ c) BM 2

Figure 2—11 Microscopical aspect of deposition

Microstructures of welded joints were evaluated through Vickers hardness measurements in a perpendicular plane on direction of movement for consumable tool (perpendicularly to Ox direction).

Due to strong strain hardness of substrate material, and also of material of consumable tool, in heat affected zone, significant changes of hardness were recorded:

- higher hardness value, approx. 24%, for steel,
- higher hardness value, approx. 33%, for aluminum.

The obtained results demonstrated that innovative proposed procedure can be developed through further research and applied if will be followed some basic rules:

- deposited material and substrate are compatible,
- optimized geometry of welding tools are used,
- substrate surface is properly prepared,
- optimal process parameters are used.

2.4 Monitoring in real time of FSW process

The field of components and materials for which friction stir welding procedure can be used is constantly expanding, process quickly became an important industrial technology and environmentally efficient. There are numerous applications especially in naval field, aeronautics and transportation, which requires welded joints on large length (2÷15m). From this reason, monitoring in real time of welding process has became a priority. The worldwide achievements for FSW process monitoring are well known. Excellent results were achieved in particular by using complex systems that ensure monitoring of the forces developed during the process and acting on the welding tools [16], [17].

2.4.1 Monitoring of FSW process using infrared thermography technique

Recent research conducted at ISIM Timisoara, have demonstrated that infrared thermographic technique can be a viable method for monitoring of automatic and semi-automatic processes, applicable also to the friction stir welding process, [18]. The following research methods were used:

- Simulation method of defects type (holes, slots and implants having different sizes), [19].
- Real time tracing method of welding process - welded joints for different materials were made using welding parameters optimized in previous research programs, the diagrams of temperature evolution were analyzed.
- Samples were taken from welded joints, which were non-destructive and destructive analyzed and controlled.

- Comparing the results of analysis diagrams of evolution temperatures measured during the welding process, with results obtained during non-destructive and destruct¬tive control and evaluation of welded joints, for a wide range of types and thickness of metallic materials.

The temperature was recorded in real time, using a Thermo – Vision A 40 M camera, with the acquisition rate of 20 images/s. This camera was placed on the welding equipment, figure 2-12, in order to trace the intersection zone between the tool shoulder and the weld surface, on the back semi-circle zone (π/2). Measurements were made on the joint line at a distance of 1 mm behind the welding tool shoulder (figure 2-12).

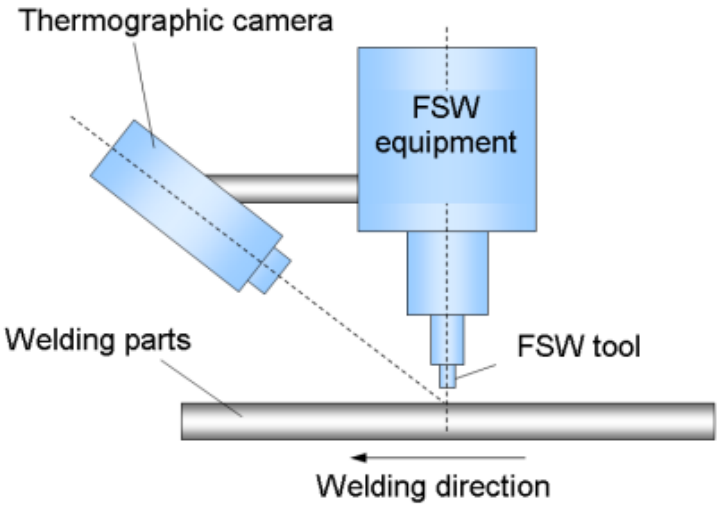

Figure 2—12 Scheme of positioning for thermographic camera on FSW machine

Based on the recorded values from the temperature measurements, done with the infrared thermographic camera, the temperature evolution diagram during friction stir welding process could be obtained.

The monitoring system can provide information on process stability, constancy of welding parameters, inducing some imperfections and/or defects, and also quality analysis of welds through the thermal image, as well as adjustment and optimization of welding parameters by feedback connections.

The check-up of operating principle in terms of identifying imperfections during the welding process, revealed that they can be evidenced through thermographic method because they represent a thermal barrier preventing the heat propagation inside of the object examined in accordance with its thermal characteristics, by having a different thermal conductivity of imperfections compared with thermal conductivity of homogeneous material.

The experiments demonstrated the viability of infrared thermography in detection of the defect during the welding process [20]. The experiments were based on different forms and dimensions for the artificial defects made in the welded sheets. The sketch with the positions and the dimensions, for the case of simulated artificial defects having elliptical slits with variable width 2-6 mm and constant depth h= 4 mm, are presented in fig. 2-13.

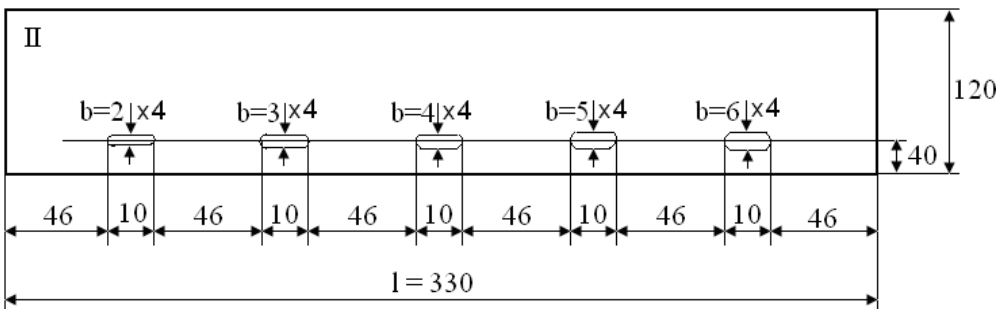

Figure 2—13 Sketch of samples with simulated defects, [19]

In respect to the temperature evolution, recorded by thermographic camera, for welds done over the open slots, the recording T = f(l), presented in figure 2-14 was obtained. Significant for the experiments are the "jumps" that appear on the temperature graphic, in front of the slits, due to the local overheating.

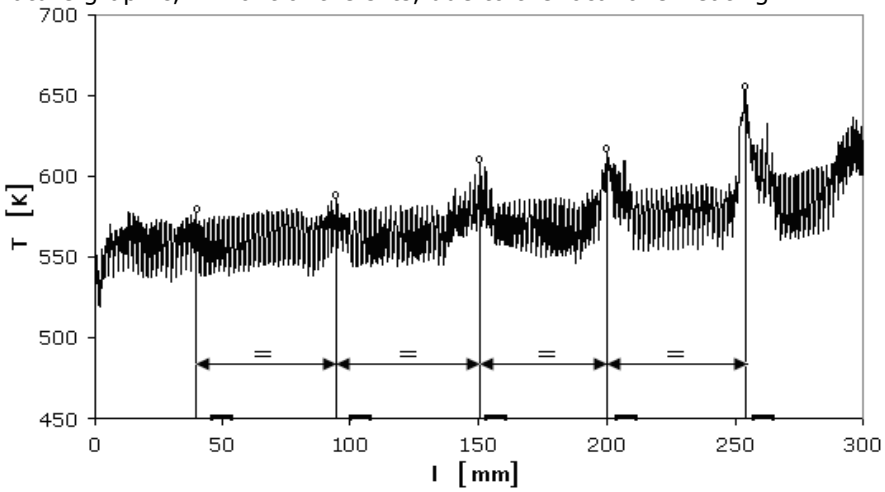

Figure 2—14 MIT recording of the process, [19]

The appearance of the peaks of temperature on the length of the welded joint and their systematic localizations in the defects zone, and in the working area of the welding tool respectively, was determined by the suddenly modification of the tem-perature gradient, caused by the thermal conductivity variation.

Also, it was concluded that, no matter the shape of the artificial defect, the minimum necessary volume to obtain a good evaluation of the thermographic recording can be determined, [19].

In the concrete application, for AISI 304L stainless steel, after the 80-100 mm from the beginning of the effective welding process, the temperature was constantly evolving around 980-1000 0C (stable welding process), figure 2-15.

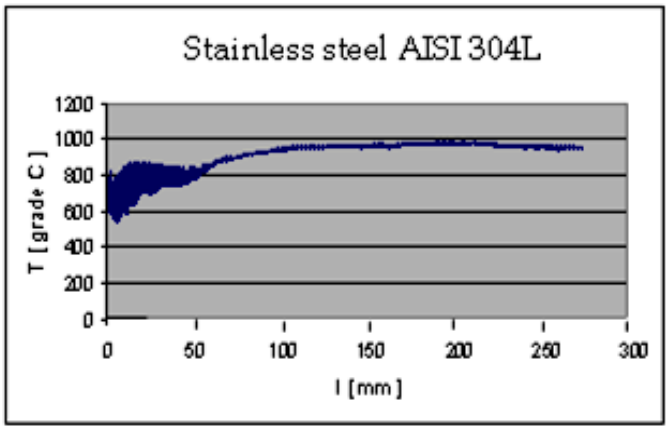

Figure 2—15 Evolution of temperature – AISI 304L, monitoring by infrared thermographic camera, [18]

Through X-Rays analyze and macroscopic analyze it has demonstrated that welded joint without defects was obtained and also formation of nuggets well consolidated in center of the weld.

A particular case was observed to another experiment for welding of AISI 304L stainless steel. Analyzing the evolution of temperature diagram from figure 2-16 is noted that approximately 150 mm welding there was a disturbance (area A).

Subsequent verifications of welded sample showed that there in that area was damage in 20% of the pin (broke a volume of approx. 20% of pine, which remained „implanted" in the welded material, figure 2-17, the area marked B.

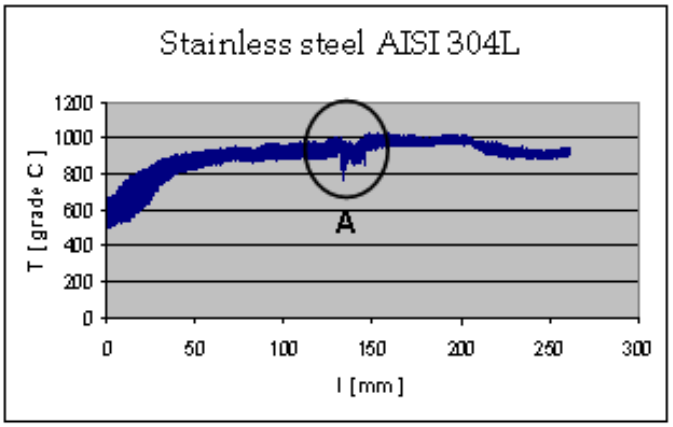

Figure 2—16 Detection of defect by thermography [18]

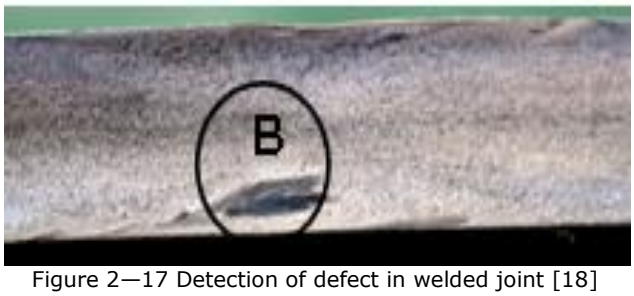

Figure 2—17 Detection of defect in welded joint [18]

This incident supports the theory that the infrared thermography technique can be used for monitoring in real time of FSW welding process.

2.4.2 Monitoring of FSW process by real time control of energy consumption

Completion the FSW machine (figure 2-18) with monitoring in real time and control system of the FSW process through control of energy consumption can provide information on process stability, constancy of welding parameters, inducing some imperfections and/or defects, and also quality analysis of welds through the

thermal image, as well as adjustment and optimization of welding parameters by feedback connections.

The experimental stand was used to measure of current consumed by FSW equipment or some of its components (engines), as well as for computerized data acquisition. It consists of (figure 2-18): FSW welding machine (position 3), welding tool (position 5), type UT 70B multimeter (position 8), computer for data acquisition, respectively for recording of measurement (position 9), computer monitor (position 10). Measurements to M1 (pos.2), M2 (pos.6) and M3 (pos.1) were done.

In the experimental program were used welding materials and FSW tools with different characteristics for which, in the previous experiments, optimization of the welding parameters was achieved.

Rotational speed has an very important role regarding to quantity of heat developed during welding process in welding materials, as well as on plasticization grade of their and forming mechanism of welded joint.

In the analysed case, M2 is the engine that provides the rotational motion of the welding tool. M2 is the most loaded engine because of:

- continuous functioning in entire time of cycle (figure 2-19)
- transmit the movement to welding tool, is directly connected to the main spindle of the FSW machine. This is necessary because of high rotational speed which are used for welding tools (400 ÷ 2000 rot/min). This fact allows to introduce some of specific modules (eg. worm gear) in cinematic chain, which could reduce the high impact of welding process on the engine (M2).

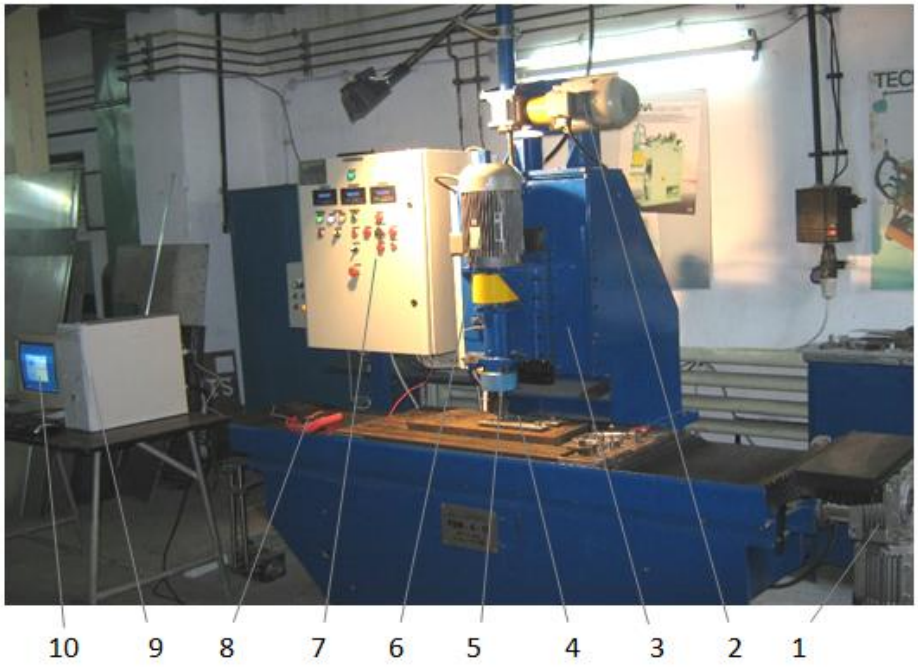

Figure 2—18 Monitoring system to determine the energetic consumption

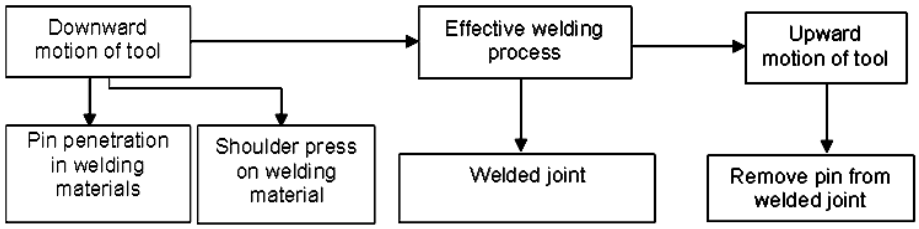

Figure 2—19 Sequences and stages of FSW process

The values recorded in principal sequences of process were tracked, namely:

- control start engine M2;
- contact between welding pin tool – welding material;
- contact between welding tool shoulder – welding materials and start effective welding process;
- welding process;
- complete the welding process ;
- remove the pin tool from welding materials

For example, when welding sheets from EN AW 6082-T651 aluminum alloy, having g=6 mm thick, there quite large variations of measured values were recorded, especially in the analysed sequences (except during effective welding process). In figure 2-20, these variations are within the range 6,3÷10 A.

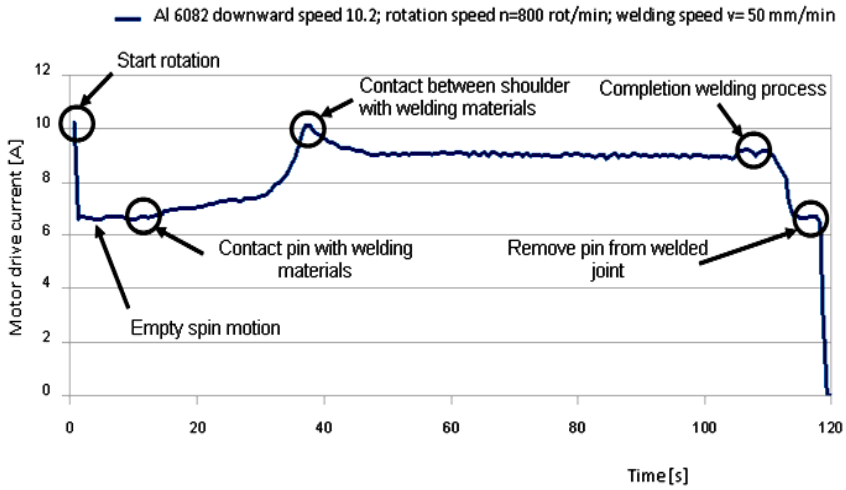

Figure 2—20 Evolution of measured consumption at M2 engine

The highest values (≈10 A) were recorded at transmission of command for rotation (start rotating tool), respectively in moment of the optimal contact (necessary and sufficient) between tool shoulder and welding materials.

Also, zones corresponding to other sequences of process are clearly dis¬tinguished: contact between pin and welding materials, completion of welding process (stop M3 engine which execute the motion with prescribed welding speed for

welding materials in relation with tool), remove of the pin tool from welding materials.

The stable evolution of values of current (≈9 A) during effective welding process is noticeable.

If the disturbance factors appeared accidently during the welding process (eg. pin broken, change of optimal position between the welding tool shoulder and the welding materials, modification of welding speed, etc.), certainly they would be influenced the stable evolution of diagram corresponding to effective welding process.

The results obtained demonstrate that through analysis of functioning behaviour of engine M2, to join the EN AW 6082-aluminum alloy, can be monitored the FSW process using optimized welding parameters (tool geometry, rotational speed and welding speed), as follows:

- shoulder of the welding tool is pushed in the welding materials until a optimal value of current, that is experimentally established, is recorded (in the analyzed previous case-10A),
- it follows that during effective welding process, optimal value of current, that is experimentally determined, to be stable (in the analyzed case ≈ 9 A).

These values can be experimentally determined for different type and thickness of material. The method is used at worldwide to determine the downforce optimal values of welding tool on welding materials. These values are used to monitoring in real time of FSW process (through downforce).

2.5 FSW of T joints

T-joints produced by FSW can be obtained by joining two or three working plates, as shown in [21]. They are used for strengthening the pressure vessels and for con¬structions of the fuselages. Figures 2-21 and 2-22 show simplified examples of position of the welding tool and model of fixture for fabricating T-joint by FSW.

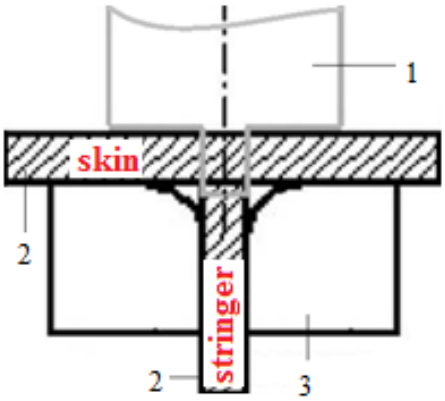

Figure 2—21 Simplified representation of FSW T-joint, positioning of 1- tool, 2-working plates and 3-backing plates [22]

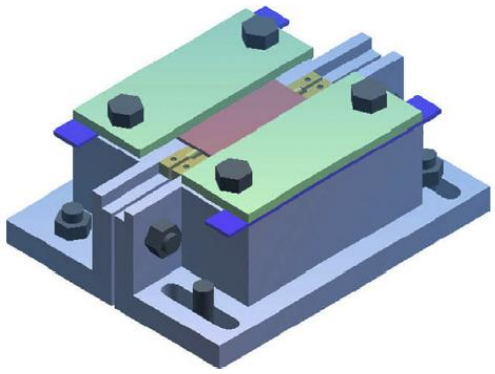

Figure 2—22 3D model of clamping tool used in FSW of T-joint, [23]

Proper selection of the tool geometry is essential. There are five welding parameters that affect the quality of welded joints and control of FSW process: the speed of rotation of the tool, welding speed, vertical (pressing) force to work materials, tool tilt-angle, tool-plunge depth and tool geometry. Here optimal combination of welding parameters is investigated in order to obtain sound T joint of Al alloy 5052-H32 and AA 5754-H111.

Experimental welding was performed on the milling machine AG-400 MINA. Rated power of the machine is 12 kW, the maximum rotational speed is 2500 o/min, the maximum feed rate is 4500 mm/min and working space is x=600 mm, y=400 mm i z= 300 mm. The first T-joint was produced by friction stir welding two plates of aluminum alloy 5052-H32 which dimensions were 30x175x5mm. Chemical composition and mechanical properties of the first T-joint are shown in Table 2-4 and Table 2-5, respectively. The second T-joint was produced by welding two plates of AA 5754-H111, which dimensions were 32x200x5mm and whose chemical composition is given in Table 2-6, and the mechanical properties are in Table 2-7. The following limits are given according to EN 485-2 and EN 573-3 standard.

Table 2-4 Chemical composition of alloy EN AW 5052-H32 [12]

%	Cu	Mn	Mg	Si	Fe	Zn	Ti	Cr
min.	0	0	2,2	0	0	0	0	0,15
max.	0,1	0,1	2,8	0,25	0,4	0,1	0,01	0,35

Table 2-5 Mechanical properties of alloy EN AW 5052-H32 [13]

Property	**$R_{p0,2}$ [MPa]**	**R_m [MPa]**	**A [%]**	**HV5**
Value	130	210-260	12	67

Table 2-6 Chemical composition of alloy EN AW 5754-H111 [12]

%	Mg	Mn	Si	Cu	Fe	Zn	Ti	Cr
min.	2,6	0	0	0	0	0	0	0
max.	3,6	0,5	0,4	0,1	0,4	0,2	0,015	0,3

Table 2-7 Mechanical properties of alloy EN AW 5754-H111 [13]

Property	**$R_{p0,2}$ [MPa]**	**R_m [MPa]**	**A [%]**	**HB**
Value	80	190-240	18	52

Special tool made of H13 tool steel was used for experimental welding. Table 5 shows the chemical composition of the tool material. The special FSW tool has cylindrical shoulder and tapered probe with a cone angle of 20°. Probe was etched curvaceous right coil whose tilt is 5°, which promotes better mixing and secondary flow of sof¬te¬ned material. Top of shoulder is concave, with a tank, as shown in Fig. 2-23a, while part of schematic drawing of tool with basic dimensions is given in the Fig. 2-23b. The process parameters used for wel¬d¬ing both of the T-joints were the same, and are given in Tab. 2-9.

Table 2-8 Chemical composition of steel H13

Element	**C**	**Si**	**Mn**	**P**	**S**	**Cr**	**Mo**	**V**
%	0,4	1	0,38	≤0.03	≤0.02	5,25	1,4	1

Table 2-9 Process parameters for T-joints

$v_{rot}\left[\frac{o}{\min}\right]$	$v_{wel}\left[\frac{mm}{\min}\right]$	**Tool tilt-angle α [°]**	**Tool-plunge depth, mm**
950	30	1	5,8

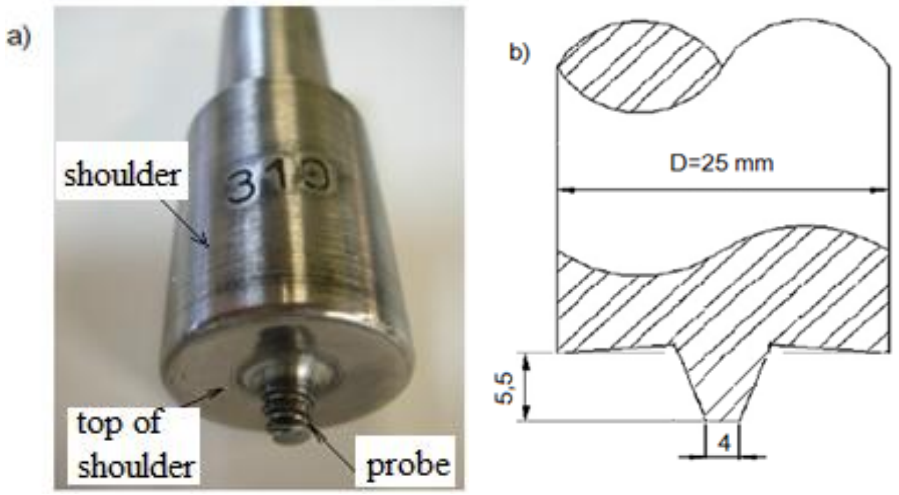

Figure 2—23 a) Photo of the tool with basic elements, and b) the part of schematic drawing of welding tool with basic dimensions

Construction of clamping tool for working plates was the same for both T-joints. Radiuses of backing plates were 2 mm. However, for welding the first T-joint

the material of clamping tool was carbon steel S355 according to EN 10025/2004 standard. Material of clamping tool for welding the second T-joint was stainless steel 1.430.

Experimental FSW included three phases. The first phase implies plunge probe of the welding tool which rotates in the working plate (first in the skin, and then in the skin and stringer). During this process, temperature was constantly increased as consequence of direct contact between surface of the rotating tool and working plates. Process continues to a temperature which causes the softening of working plates. Soften material flows around the probe of the tool due to its rotation and penetration into the working plates. Then, there is direct contact with the surface of the top of shoulder and working plate (skin). Tool plunge in working plates lasted 1.5 min, while retaining the tool in the working plates (tool only rotates) was 0.5 min. Next is the phase of the welding process. The tool is translating, with a given welding speed, with a constant rotation. Softened material of working plates is transported around the probe, and along the longitudinal axis of the tool, between the top of the shoulder and solid-state walls of working plates. Model of this phase is given in Figure 2-24. During the third phase of the welding tool translation, it stops, extracts away from the working plates, thus leaving behind a cylindrical hole, so-called key-hole.

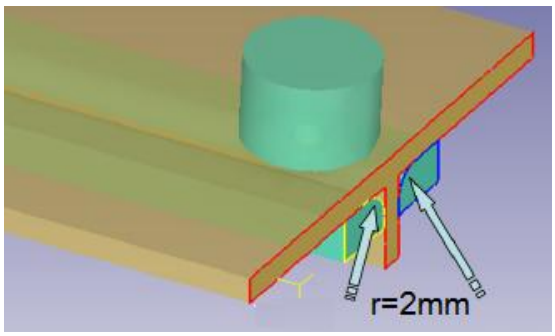

Figure 2—24 3D model of the second welding phase

Welded T-joints were examined using visual inspection, metallographic macrostructure observation and micro¬hardness testing.

2.5.1 Quality and microstructural zones of T joints

When welding process was completed, first performed a visual inspection of the face and root sides of the weld metal. On the face of the weld metal, as shown in Figure 2-25, indicates tunnel, but could not be sure to confirm its presence without metallographic examination. A higher flash of material on retreating side of the weld metal has been observed. Flash is a phenomenon that with a proper choice of tools can be minimized but not eliminated. Figure 2-26 gives face appea¬rance of AA 5754-H111. The surface of the face is smooth and tunnel type defect is not noticed.

Metallographic examination of macrostructure was observed structural changes, as well as the flow of materials. Figures 2-27 and 2-28 show structural

zone of FSW T-joint, and these are: heat affected zone (HAZ), thermo-mechanically affec¬ted zone (TMAZ) and nugget zone (NZ). The samples are cutting perpendicular to the direction of welding direction.

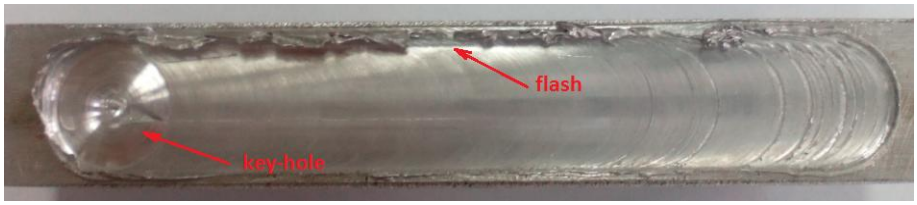

Figure 2—25 The face of weld metal of first T-joint

Figure 2—26 The face of weld metal of the second T-joint

Tunnel was observed on advancing side of the weld (Fig. 2-27). This defect occurs due to lack transport of softened material from retreating side toward advancing side of weld metal, i.e. insufficient mixing softened material due to improper welding parameters. On root side of the weld, in the immediate vicinity of nugget, a defect type called kissing bond is present. Kissing bond usually occurs due to insufficient penetration of the tool into working plates. This defect usually makes the initial crack in nugget. Second FSW T-joint of AA 5754-H111 is without imperfections.

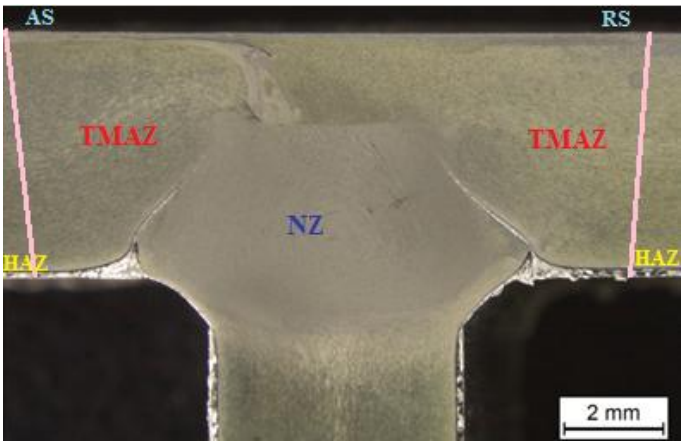

Figure 2—27 Macroscopic view of section of first FSW T-joint

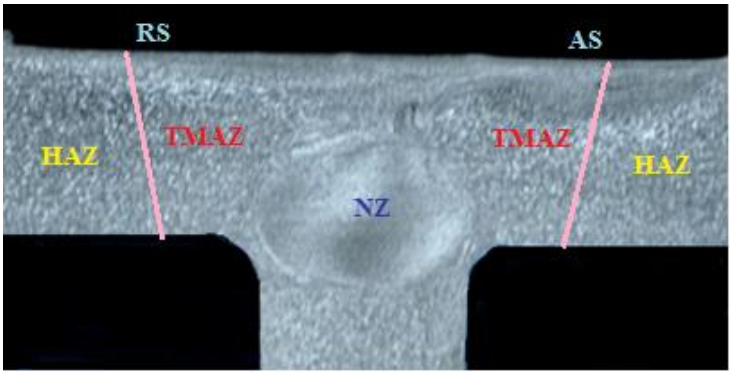

Figure 2—28 Macroscopic view of section of second FSW T-joint

Structure of nugget is characterised with concentric circles. These concentric circles, called onion rings, are charac¬te¬ristic for this area (Fig. 2-27 and 2-28). In the nugget zone, and part of thermo-mechanical affected zone near nugget structure is recrystallized and fine-grained. This is because grains are roughly mixed in this part of weld. The structure in the heat affected zone is similar to the base material.

2.5.2 Hardness distributions

Hardness was determined by micro-hardness measurement with force 10 N. Optical stereo microscope with software were used for image ac¬quisition and processing. Micro-hardness of AA 5052-H32 is measured near the face of the weld metal, as shown in Fig. 2-29.

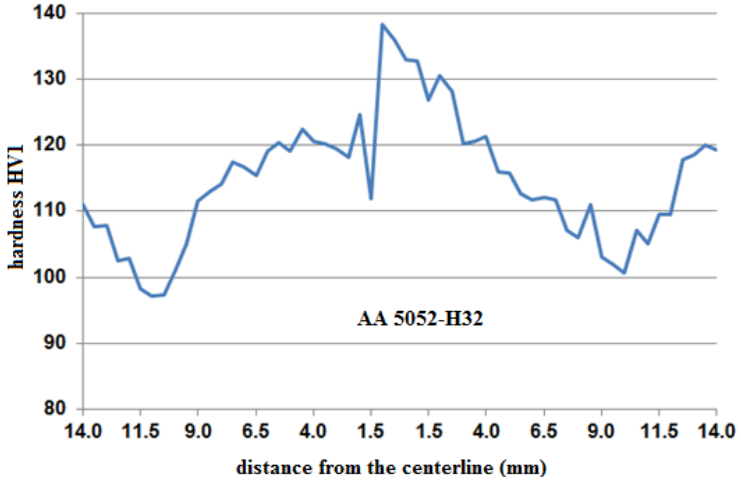

Figure 2—29 Hardness distributions of Al alloy 5-52-H32

With used welding parameters it was possible to make a sound T-joint by FSW process. The visual examination of T-joint of AA 5052-H32 has not revealed the presence of defects. Macroscopic examination noticed two types of defects:

tunnel and kissing bonds on root side of weld. Based on the experience gained during experiment, these defects are caused by incorrect choice of welding parameters and lack of generated heat at the joining zone. One of the main cause of occurrence of these defects is a great heat conduction during FSW of T-joint, which is largely determined the choice of material type for the backing plates and clamping tool. Therefore, in order to obtain T-joint without defects with applied tool and welding parameters, the material of the clamping tool (carbon steel class S355) should be replaced by a material that less conducts heat. T-joint of AA 5754-H111 is also without imperfections. Stainless steel 1.4301 and 1.4541 have proved to be good materials for backing plates and clamping tool.

2.6 Concluding remarks

- Since year 2000, the researches for friction stir welding process were included in scientifical program of ISIM Timisoara.
- Applying the innovative FSW-TIG hybrid welding, relative to classical FSW assure: productivity increase, through considerable increase of welding speed; machine protection and FSW welding tools, through reducing of forces that are developed during FSW process (obtaining a stable welding process), significantly reducing of wear for welding tools.
- The feasability of depositing the functional layer of aluminum alloy on steel substrate, using friction stir welding principle was demonstrated. The rotating active element is a consumable tool.
- Monitoring in real time of the welding process is important owing to use FSW process in many industrial applications (especially those requiring long lengths of welded joints). Two innovative methods, based on experiments, were developed for this. These evidenced that:
  - There are the real possibilities, qualitative and quantitative for detection of defects from FSW welded joints through infrared thermography. On one side, a good re-pro¬ducibility of results relative to defects localization, was evidenced, and on the other side a dependence of temperature variations of the volume displaced by defects.
  - Good results can be achieved by monitoring of functioning behaviour for engine that assure rotation speed of welding tool, obtaining of information about current consumption in the main sequences of FSW process: start rotation - contact between pin tool and welding materials - contact between tool shoulder and welding materials - effective welding process - completion of process and remove of welding tool from welded joint.
- Friction Stir Welding of T joints has also been successfully performed, as the latest contribution, in cooperation with GOSA, Smederevska Palanka, Serbia. Sound welded joint, with full penetration, have been obtained and tested, providing good results and indicating strong potential for further developments.

3 EXPERIMENTAL WORK

3.1 Preparation of material

The material used in this study was aluminum 5083 alloy, hot rolled plates of thickness 6 mm, length 1000 mm and width 500 mm. The chemical and mechanical properties are given in tables 3-1 and 3-2.

Table 3-1 The chemical composition of Aluminum 5083 alloy

Mg	Mn	Cu	Fe	Si	Zn	Cr	Na	Ti	Zr
5.13	0.718	0.013	0.337	0.108	0.513	0.008	0.0005	0.0254	0.0202

Table 3-2 The mechanical properties of Aluminum 5083 alloy

Deformation [%]	Thickness of specimens mm	Yield strength [MPa]	Ultimate strength [MPa]	Elongation max [%]
16.6	6	301	369	9.8

3.2 Tool shoulder and tilt angle

The shoulder is designed as a relatively large, when compared to the probe, profiled surface. Although the probe makes the initial contact with the pre-welded material the shoulder has a larger contact area and produces more friction.

Figure 3—1 Tool shoulder

The tool tilt angle favors the material movement towards the travel direction and also the mixing of the plasticized material flow in the weld zone. The material movement along the travel direction plays an important role in the bond formation. The tool edges are represented by 'a' and 'b' in Fig. 3-2, which shows the schematic diagram of the tool tilt angle influence on the work plate.

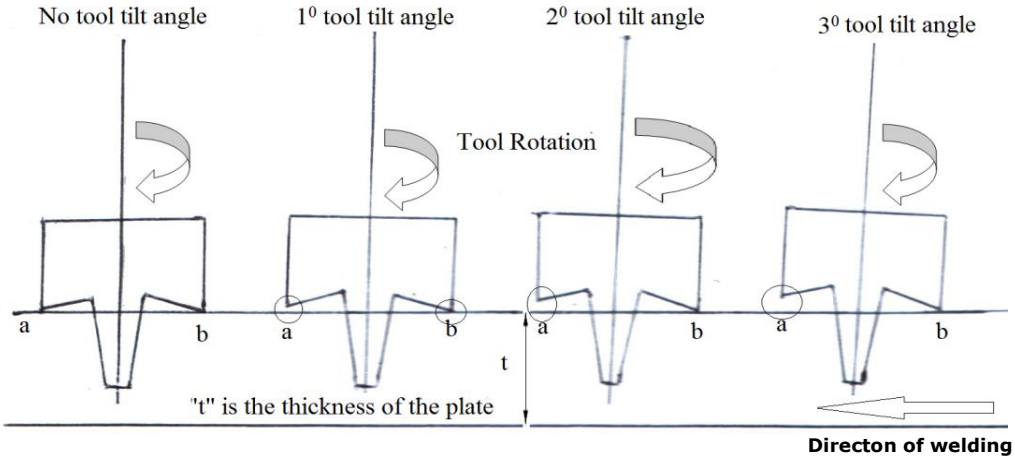

Figure 3—2 Schematic representation of tool tilt angle

When the tool is tilted 1° towards the feed direction, the edge 'a' touches the work plate and 'b' slightly penetrates the plate. If the tool tilt angle is further increased to 2° the tool lifts up at 'a' and 'b' penetrates deeply into the work plate, if the tool angle increased to 30 or more the edge 'a' more lift up and 'b' in retreating side into more deeper in work piece when start FSW of alloys.

3.3 Operation of FSW Process

Shoulder tool with profiled probe is rotated and slowly plunged into the joint line between two pieces of plate material, which are fixed and butted together, figure 3-3. The tool was slowly plunged into the workpiece at the butt line, until the shoulder of the tool forcibly contacted the upper surface of the material and the pin was a short distance from the back plate. The depth of penetration was controlled by the length of the profiled pin below the shoulder of the tool. The initial plunging friction contact heated the adjacent metal around the probe, as well as a small region of material underneath the probe, whereas the friction between shoulder and material interface generated significant additional heat to the weld region.

Figure 3—3 Clamps of work piece to machine FSW.

Different welding speeds were used (75, 100 and 125 mm/min), as well as different rotation speeds (500, 600 and 700 rpm), in addition to different tool angles.

3.4 Charpy Test

The Charpy test specimens had 10 x 6 x 55 mm3 dimensions, a 450 V notch of 2 mm depth and a 0.25 mm root radius, figure 3-4. Two specimens were tested from the same combination of parameters like rotational speed, welding speed, and tilt angle. The absorbed energy required to produce two fracture surface was recorded and separated into the initiation and propagation energy, using standard testing device, in the Aeronautical Military Institute, Belgrade.

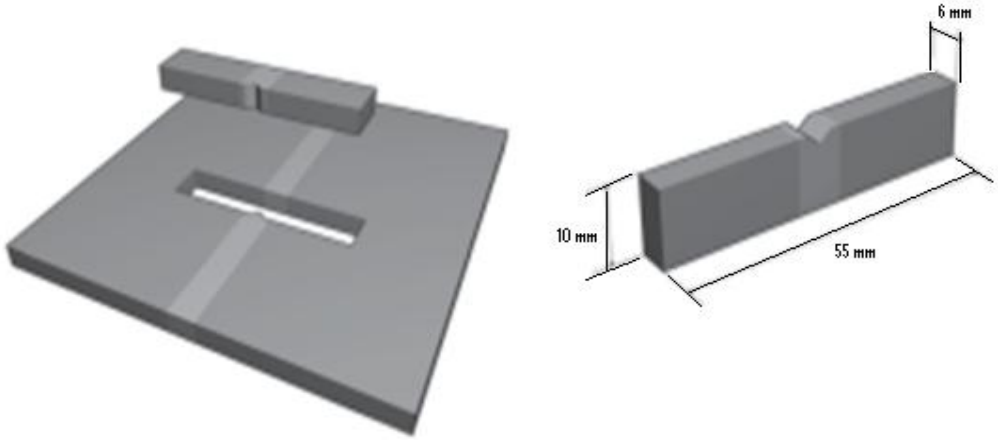

Figure 3—4 Scheme of the machining of Charpy specimens from FSW plates

Schematic presentation of the instrumented Charpy pendulum is shown in Fig. 3-5, its appearance in Fig. 3-6, whereas the separation into the initiation and propagation energy is shown figure 3-7.

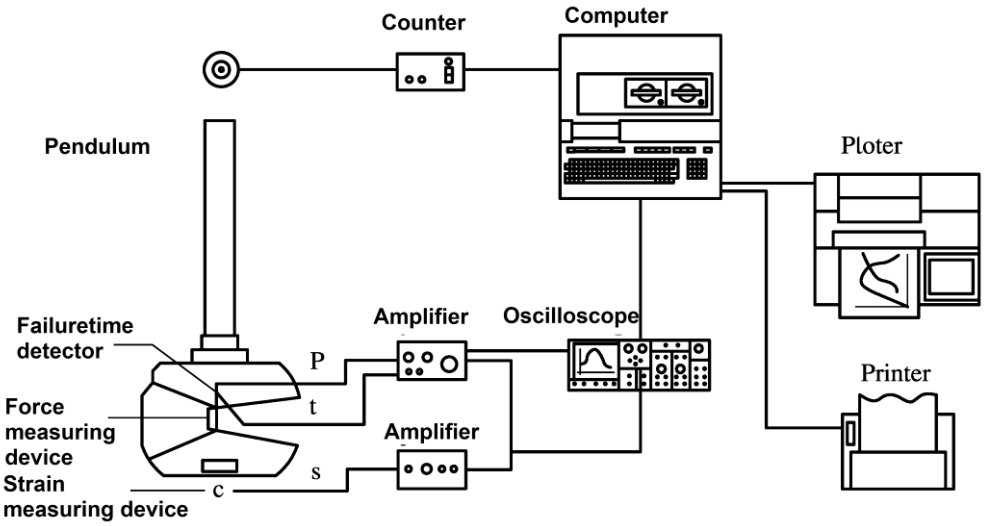

Figure 3—5 Schematic presentation of the instrumented Charpy pendulum

Figure 3—6 The instrumented Sharpy pendulum SCHNECK TREBEL 300 J

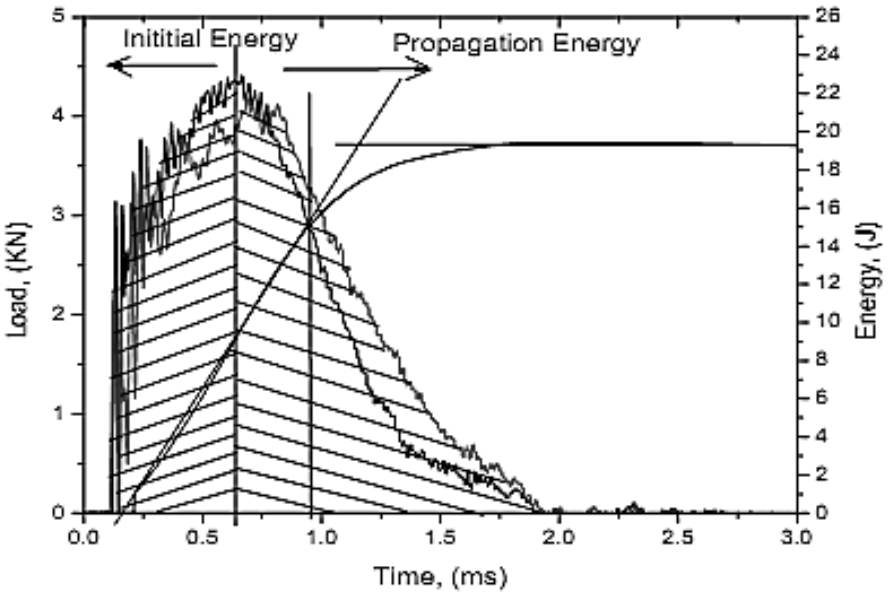

Figure 3—7 Diagramme Load vs. time with separation of energies

One should notice that separation of energies in this thesis has been done slightly different than the usual way, Fig. 3-7. Namely, as explained in [30], the time at the maximum force is not always the best way to separate the initiation and propagation energies, because propagation actually starts a bit sooner. This was overcome in [30] by using energy-time diagramme instead, but here the new technique was applied, based on the change of slope of force just ahead of its maximum value.

3.5 Testing of FRACTURE TOUGHNESS K_{Ic}

Fracture mechanics testing was done in order to determine critical value of stress intensity factor, KIc. Specimens for three point bending (SEB) were used for the testing. Their geometry is defined by the ASTM E399 standard, [24], as shown in Fig. 3-8. The notch was positioned in the weld metal, and the crack was produced by standard procedure.

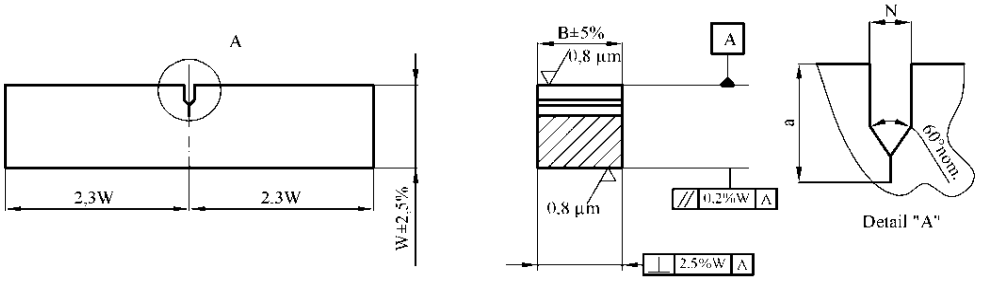

Figure 3—8 Specimen for fracture mechanics testing

The testing itself was performed, at the room temperature, on the electro-mechanical testing machine SCHENCK TREBEL RM 100 in the Aeronautical Military Institute, Belgrade. Crack tip opening was registered by the special extensometer KLIP-GAGE DD1, which measuring accuracy is ±0,001 mm.

The fracture toughness, KIc, was determined using the critical value of J integral, fracture toughness measure, JIc, by testing according to the ASTM E813-89 [25]. Testing method of a single specimen successive partial unload were used for the J integral determination. Points of the curve are obtained from the pair of data, acting force, F, crack tip opening, δ. The J - Δa diagram, as defined by standard, including valid and invalid data points, is shown in Fig. 3-9.

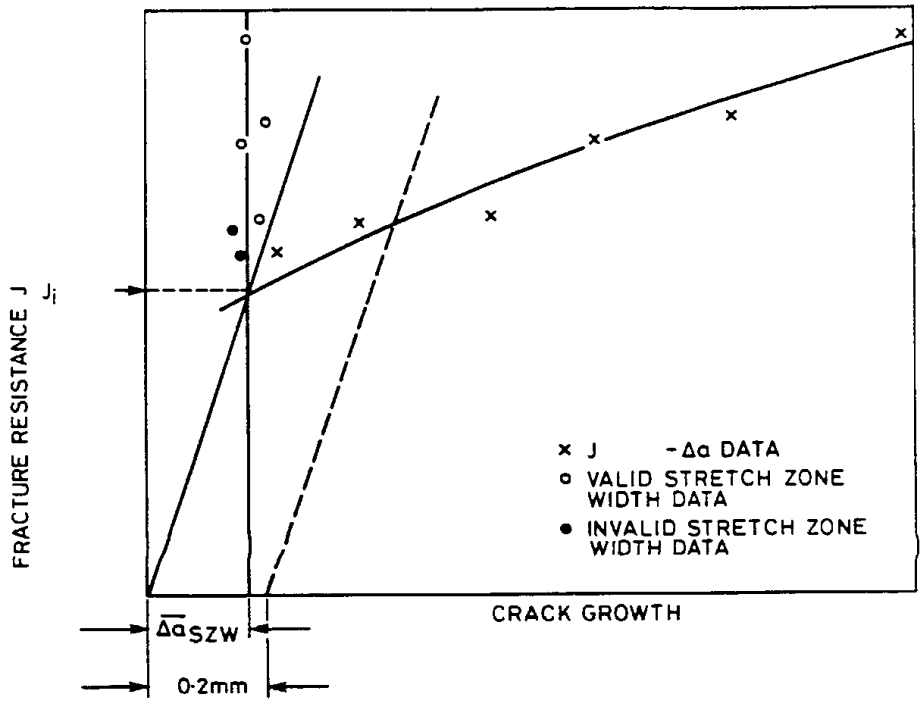

Figure 3—9 The J-Δa diagram

Knowing the values of the critical JIc integral, the value of critical stress intensity factor or fracture toughness at plane strain, K_{Ic}, can be calculated as:

$$K_{Ic} = \sqrt{\frac{J_{Ic} \cdot E}{1-\nu^2}} \qquad (3\text{-}1)$$

3.6 Taguchi method for the optimization of process parameters

A large number of experiments have to be carried out when the number of input and output parameters increases. To solve this task, the Taguchi method uses a special design of orthogonal arrays to reduce number of experiments to a reasonable level.

The flowchart of the Taguchi method for DOE is illustrated in Figure 3-10.

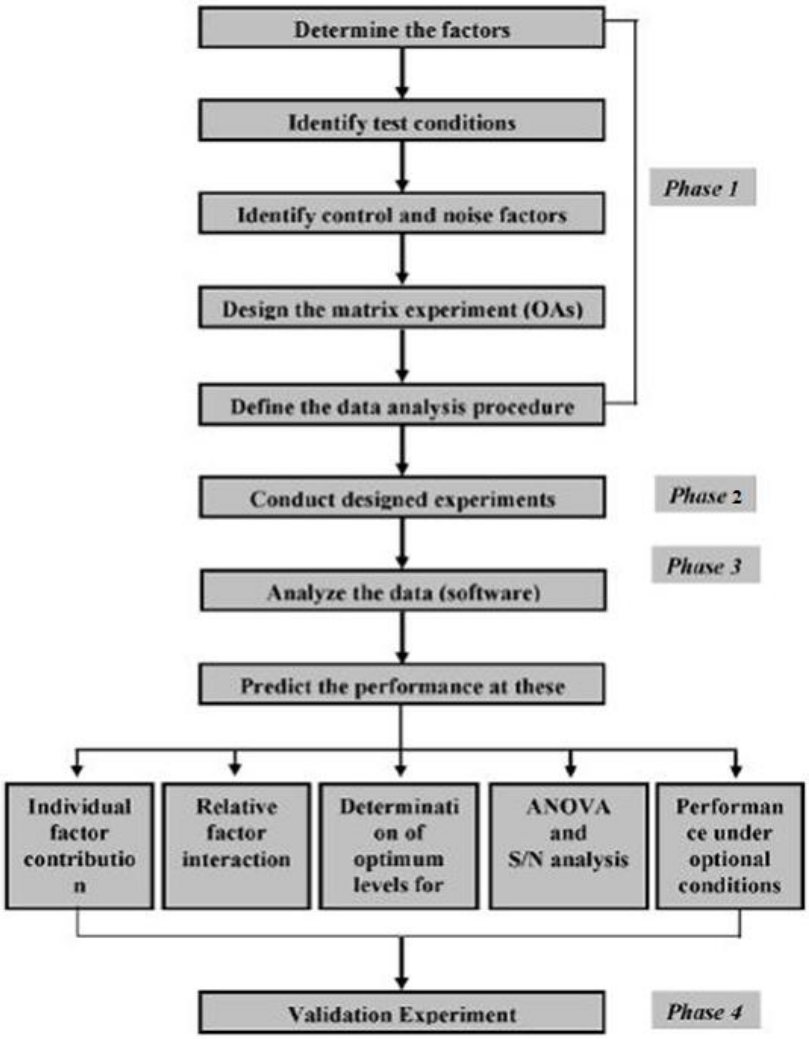

Figure 3—10 Taguchi method for DOE – the flowchart, [26]

Usually, there are three categories of the quality characteristic in the analysis of the S/N ratio, i.e. lower-the better, higher-the-better and nominal-the better. The S/N ratio for each level of process parameters is computed based on the S/N analysis. Regardless of the category of the quality characteristic, a larger S/N ratio corresponds to a better quality characteristic. Therefore, the optimal level of the process parameters is the level with the higher S/N ratio. Furthermore, a statistical analysis of variance (ANOVA) is performed to see which parameters are statistically significant. The optimal combination of the parameters can then be predicted.

3.6.1 Signal to noise (S/N) ratio

There are three forms of signal to noise (S/N) ratio that are of common interest for optimization of statistical problems. Here we consider "Larger-the-better", when the loss function of the higher the better quality characteristic can be expressed as:

$$L_{ij} = \frac{1}{} \sum_{=1} \frac{1}{y_{ijk}^2}$$

where L_{ij}, is the loss function of the i-th quality characteristic in the j-th experiment, n the number of tests, and yijk the experimental value of the ijth quality characteristic in the jth experiment at kth test, being equal to:

$$-10\log_{10}[mean\ of\ sum\ of\ squares\ of\ reciprocal\ of\ measured\ data]$$

3.6.2 Analysis of Variance ANOVA

The purpose of ANOVA is to investigate which process parameters significantly affect the quality characteristics. This is accomplished by separating the total variability of the S/N ratios, which is measured by the sum of squared deviations from the total mean of the S/N ratio, into contribution by each of the welding process parameter and the error. The percentage contribution by each of the welding process parameters in the total sum of the squared deviations can be used to evaluate the importance of the process parameter change on the quality characteristic.

Mean of sum of main characteristic (yijk) is given by the following formula:

$$m = \sum(y_{ijk1} + y_{ijk2} + \cdots + y_{ijkn}) \quad (3.2)$$

The average values of the mean are given as follows, for 3x3 scheme:

$$\begin{aligned}
mA1&=(y_{ijk1}+y_{ijk2}+y_{ijk3})/3;\\
mA2&=(y_{ijk4}+y_{ijk5}+y_{ijk6})/3;\\
mA3&=(y_{ijk7}+y_{ijk8}+y_{ijk9})/3;\\
mB1&=(y_{ijk1}+y_{ijk4}+y_{ijk7})/3;\\
mB2&=(y_{ijk2}+y_{ijk5}+y_{ijk8})/3;\\
mB3&=(y_{ijk3}+y_{ijk6}+y_{ijk9})/3; \quad (3.3)\\
mC1&=(y_{ijk1}+y_{ijk6}+y_{ijk8})/3;\\
mC2&=(y_{ijk2}+y_{ijk4}+y_{ijk9})/3;\\
mC3&=(y_{ijk3}+y_{ijk5}+y_{ijk7})/3;
\end{aligned}$$

Other formulas used for Taguchi method are given as follows:

Grand total sum of squares:

$\sum_{i=1}^{4} n_j^2$ (3.4)

Sum of squares due to mean:

$\sum_{I=1}^{4} m^2$ (3.5)

Total sum of squares:

$\sum_{i=1}^{4} (n_j - m)^2$ (3.6)

Sum of squares due to A:

$\sum_{i=1}^{4} (m_{Ai} - m)^2$ (3.7)

Sum of squares due to error:

$\sum_{i=1}^{4} e_i^2$ (3.8)

3.6.3 Optimization

Optimization of process parameters is the key step in the Taguchi's method to achieve high quality without increasing cost, [27]. This is because, optimization of process parameters can improve quality characteristic and optimal process parameters obtained from Taguchi method are insensitive to the variation of environment conditions and other noise factors. In the problem analysed here, 9 trials are used, as defined in Table 3-3, to replace 27 experiments (3 parameters, 3 values, 27=33).

Table 3-3 The experiment scheme

Trial	**1**	**2**	**3**
1	1	1	1
2	1	2	2
3	1	3	3
4	2	1	3
5	2	2	1
6	2	3	2
7	3	1	2
8	3	2	3
9	3	3	1

3.7 Results and discussion

The parameters of FSW used to welded material alloys were:

- rotation speeds 500, 600 and 700 rpm
- weld-tool travel speeds 75, 100 and 125 mm/min,
- tilt angles 1, 2 and 30.

As explained in #3.6, only 9 experiments were needed instead of 27, as presented in table 3-4, where results for the impact energy is given (two specimens and their average value) and in Table 3-5, where results for fracture toughness are given in the same way. Some of the results for impact toughness (first three rows) are presented also in [28, 29, 30].

Table 3-4 Average (two measurements) absorbed Energy Recorded from Charpy Test.

No. of Sample	Rotation Speed (rpm)	Welding Speed (mm/min)	Tilted Angle (^{0})	Average Energy (J)	First measurement (J)	Second measurement (J)
1 1 1	500	75	1	15.05	14.9	15.2
1 2 2	500	100	2	19.25	19.0	19.5
1 3 3	500	125	3	22.9	22.7	23.1
2 3 2	600	125	2	21.5	21.5	21.5
2 2 1	600	100	1	16.4	16.1	16.7
2 1 3	600	75	3	17.3	17.0	17.6
3 2 3	700	100	3	21.9	21.4	22.4
3 1 2	700	75	2	21.65	21.5	21.8
3 3 1	700	125	1	23.75	23.6	23.9

Statistical analysis of results for the impact energy, including separated values for initiation and propagation, is given in tables, 3-6, 3-7 and 3-8, respectively. Only average values have been used, since the difference between individual values is small.

Table 3-5 Average separated energy from Charpy Test.

No. of Sample	Rotation Speed (rpm)	Welding Speed (mm/min)	Tilted Angle (^{0})	Average Energy (J)	Initiation energy (J)	Propagation energy (J)
1 1 1	500	75	1	15.05	7.05	8.0
1 2 2	500	100	2	19.25	8.8	9.45
1 3 3	500	125	3	22.9	10.8	12.1
2 3 2	600	125	2	21.5	9.5	12.0
2 2 1	600	100	1	16.4	5.8	10.6
2 1 3	600	75	3	17.3	6.5	10.8
3 2 3	700	100	3	21.9	9.7	12.2
3 1 2	700	75	2	21.65	9.25	12.4
3 3 1	700	125	1	23.75	10.15	13.6

Table 3-6 Statistical analysis of the impact energy

m	**1**	**2**	**3**	**$\Sigma diff^2$**	**%**
mA	19.1	18.4	22.4	27.4	27.4/63.7=43
mB	18.0	19.2	22.7	35.7	35.7/63.7=56
mC	19.5	20.1	20.0	0.6	0.6/63.7=1

Table 3-7 Statistical analysis of the initiation energy

m	**1**	**2**	**3**	**$\Sigma diff^2$**	**%**
mA	8.9	7.3	9.7	8.96	8.96/21.14=42
mB	8.7	7.9	9.1	4.04	35.7/63.7=19
mC	7.6	9.5	8.8	8.14	0.6/63.7=39

Table 3-8 Statistical analysis of the propagation energy

m	**1**	**2**	**3**	**$\Sigma diff^2$**	**%**
mA	9.8	11.1	12.7	12.66	12.66/20=63
mB	10.7	10.8	12.2	4.23	4.23/20=21
mC	10.4	11.7	11.6	3.14	3.14/20=16

Table 3-9 Average (two measurements) fracture toughness test.

No. of Sample	**Rotation Speed (rpm)**	**Welding Speed (mm/min)**	**Tilted Angle (^{0})**	**Average KIc MPa√m**	**First measurement MPa√m**	**Second measurement MPa√m**
1 1 1	500	75	1	55	53	57
1 2 2	500	100	2	60	58	62
1 3 3	500	125	3	70	69	71
2 3 2	600	125	2	72	71	72
2 2 1	600	100	1	66	64	67
2 1 3	600	75	3	72	70	73
3 2 3	700	100	3	75	74	77
3 1 2	700	75	2	76	75	77
3 3 1	700	125	1	67	66	69

The results for the fracture mechanics testing is given in Table 3-9. The same procedure for statistical analysis has been applied in the case of fracture toughness, also using only the average values, for the same reason.

Table 3-10 Statistical analysis of the fracture toughness

m	**1**	**2**	**3**	**$\Sigma diff^2$**	**%**
mA	60.2	70.0	72.7	259.58	259.58/295.82 = 88
mB	67.3	67.3	69.7	11.52	11.52/295.82 = 4
mC	67.7	66.3	69.7	24.72	24.72/295.82 = 8

Figure 3-11 shows the relationship between load and displacement for one pair of specimens, as an example. The load rises rapidly to maximum value and drops suddenly. This drop in load marks the boundary line of two distinct phases i.e., fracture initiation and fracture propagation phase of the total fracture event. In fact, specimen having the biggest area under the curve, also has the highest toughness. Other diagrammes are given in the Appendix 1.

The J - Δa diagram for specimen with a crack in the weld metal (WM- NZ) is shown in Fig. 3-12, as an example of fracture toughness testing, performed in the scope of this thesis (trial 1). Other diagrammes are given in the Appendix 2.

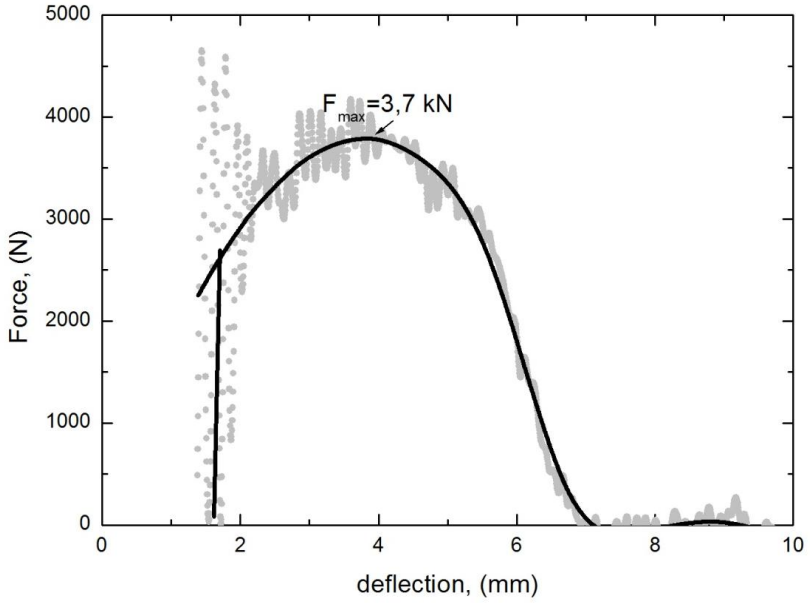

Figure 3—11 Load displacement curve for the trial 1b sample

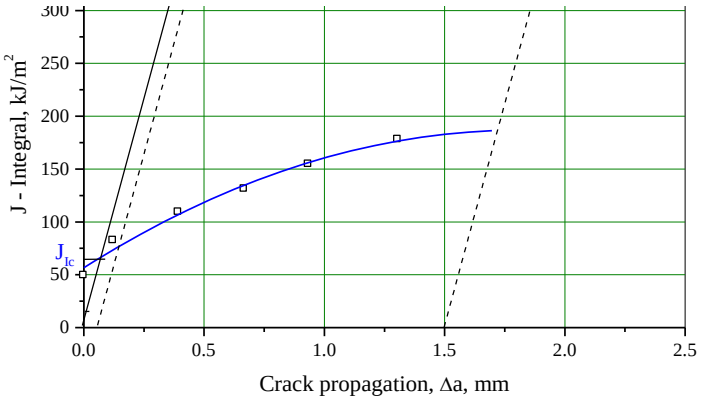

Figure 3—12 The J-Δa diagram for the trial 3a sample

3.8 Microstructural examination

Microstructural examination has been performed in the Laboratory for Metalography, Institut Vinca. These results serve here only for the purpose of completing the overall insight in the problem and are also presented in [28, 30]. The surfaces of friction stir weldments are shown in the Fig. 3-13(a,b), where solid, overlapping scratches can be seen along the welding zone. Here, the tool was driven to the left-side direction, with the clock-wise rotation. These scratches clearly indicate discontinuous nature of frictions stir process.

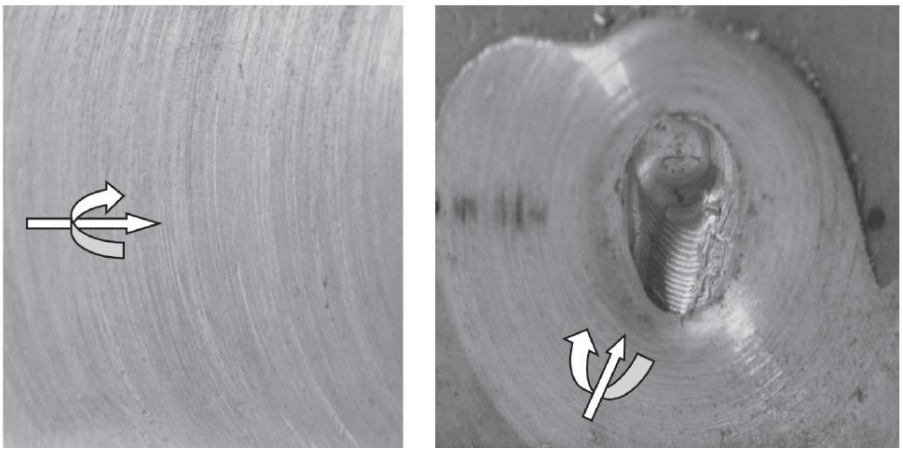

Figure 3—13 Welding surface (a), and the exit-point of the tool from the weld (b). Arrows indicate directions of rotational and welding speed

In the HAZ, remote from the centre of the weld, there is no obvious change to the grain structure, and the HAZ is detected only by a change in hardness and generally by a change in etching response by different rotation speed. In

precipitation hardened alloys it is widely accepted that some coarsening of precipitates is occurring, and possible dissolution at higher temperatures, [31]. In work hardened alloys, dislocation networks may recover, and this may cause some low angle cell boundaries to form. Furthermore as the weld centre is approached, clear evidence of plastic deformation can be seen in the grain structure. In the outer part of the TMAZ, the original grains remain identifiable in the deformed structure, with the formation of subgrain structures and significant associated rotation of the parent grains.

A common observation from the nugget region in FSW is the appearance of a series of circular or elliptical features in metallographic sections (Figure 3-14), often termed as 'onion rings' (as the sections reveal a slice through a set of nested layers of roughly hemispherical shape, like an onion), [31]. Cyclic fluctuations in the amount of material extruded past the tool and being deposited are to be expected with profiled tools as shown in Figure 3-14. The practical significance of the phenomenon remains rather limited as the mechanical properties of the nugget are generally good, and the fracture paths in mechanical tests are seldom associated with the onion rings, [32].

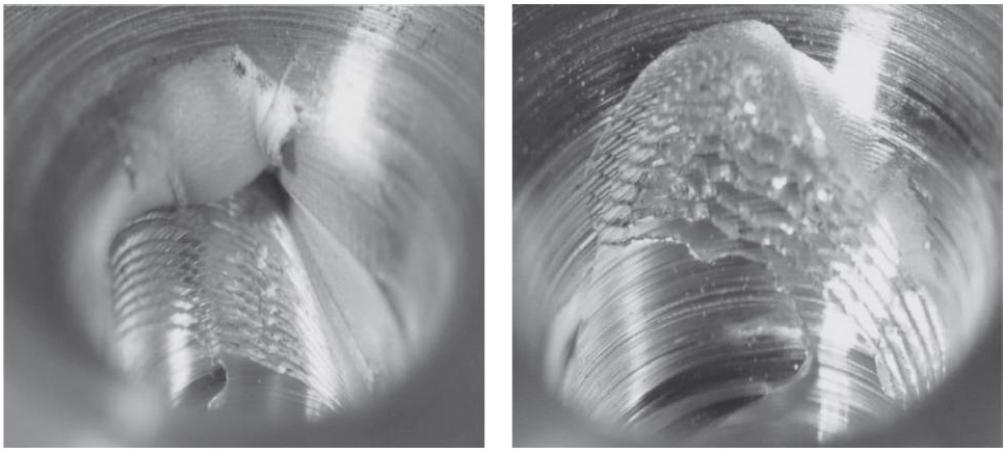

Figure 3—14 (a,b): Material flow and onion rings in exit keyhole.

A distinctive feature of the microstructure of friction stir welds in aluminum alloys is the development of a fine grain structure in the centre of the nugget region. On the basis of these observations, it has been concluded that the nugget consists of dynamically recrystallised grains, and not subgrains. High values of forward tool motion per revolution produce harder microstructures, but generally similar grain size. In a study carried out in the region of the tool pin exit hole in a sample of AA5083 alloy it has been argued that the structure of the weld nugget is one of dynamically recovered subgrains, [33]. Plastic deformation continues with the repeated introduction of dislocations and the process continues until the end of the thermomechanical cycle, at which point partial recovery takes place, [34].

Detailed SEM investigations were performed to better understand fracture mecha-nism during Charpy impact tests. Example of these investigations are shown in Fig. 3-15a-i. The fracture surface of specimen previously welded by rotational speed 600 rpm, welding speed 75 mm/min and tilt angle 10 is shown. It was

distinguishing ductile fracture with existing microvoids near the notch (Fig. 3-15c). Also, the upper side the specimen (Fig. 3-15i,g,h) was subjected to more heating than the lower, opposite side due to contact with shoulder and pin. Moreover, from the figure can be observed that ductile fracture is prevailing with existing microvoids in the nugget zone. Also is shown the appearance of shear or cleavage in the lower surface of specimen. The type of tearing close to notch was more-to-brittle then propagation fracture in nugget zone. Also, similar tearing of specimens were detected at specimens that were welded by 700 rpm, 75 mm/min and tilt angle 10. Overall observations suggest that if absorbed welding energy is higher, the specimens dispose more fracture toughness.

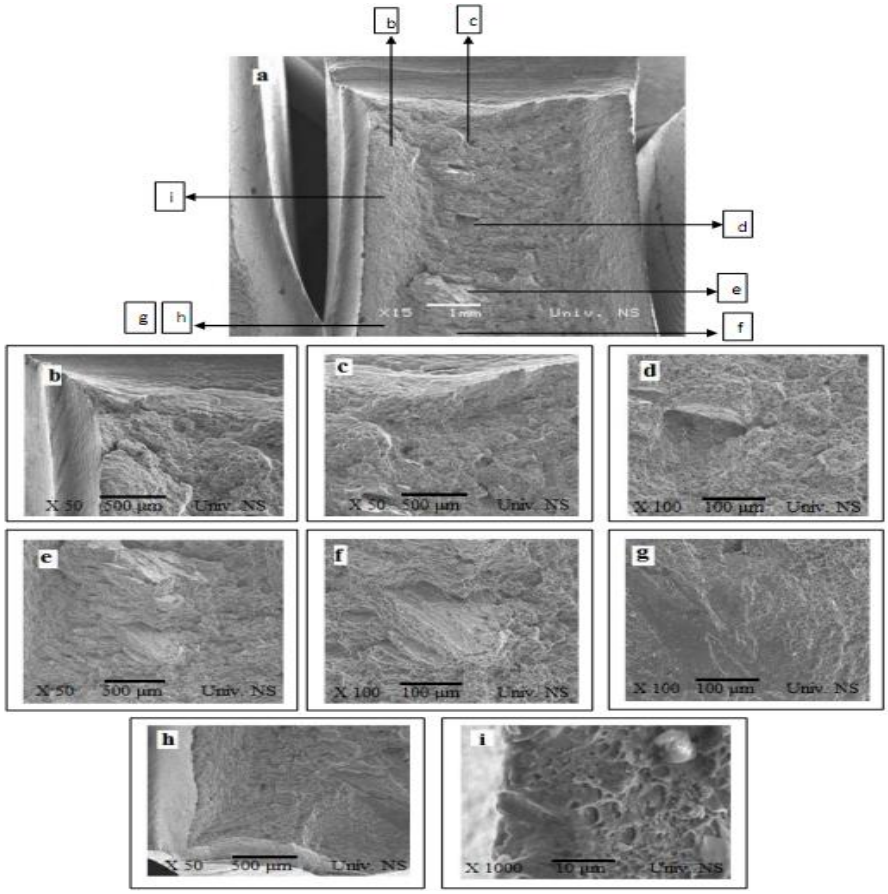

Figure 3—15 (a-i). SEM examinations of impact fractured specimen. Friction stir welding con¬ditions: rotational speed 600 rpm, welding speed 75 mm/min and tool-tilt angle 10.

The influence of FSW parameters on the formation of the stir zone and the toughness of friction stir welded 5083 Al alloy was examined in the present study. The stir zones expose onion-rings microstructure that were connected to the tool "advance-per-rotation" phenomena. The impact toughness of the stir zone is found to be depen-dent on welding parameters. It is attributed to the material and frictional heat flow within the stir zone and its influence on the grain size and

recrystallisation. The SEM fracto-graphic investigations have revealed distinctive fracture modes transitioning within the stir zone.

3.9 Fatigue testing

The fatigue crack growth under variable loads can be described by the following equation, usually known as the Paris law,

$$\frac{da}{dN} = C \cdot \Delta K^m \tag{3-9}$$

Here the stress intensity factor range, ΔK, is defined as

$$\Delta K = K_{\max} - K_{\min} \tag{3-10}$$

where K_{max} and K_{min} are maximum and minimum stress intensity factors corresponding to the maximal load, P_{max} (or maximal nominal stress, σ_{max}) and minimal load, P_{min} (or minimal nominal stress, σ_{min}) in a cycle. Values C and m in Eq. (3-9) are constants obtained empirically, and depend on the properties and material microstructure, fatigue frequency, mean stress, the environment, loading mode, stress state and the applied temperature. The empirical law of crack growth, expressed by Eq. (3-9) and presented in Fig. 3-16 as a sigmoidal curve, is a most frequently used form for the characterisation of crack growth rate for a broad spectrum of engineering materials and testing conditions.

Three different regimes of crack growth can be recog¬nised from the diagram in Fig. 3-16. In the regime A, the average increment of crack growth is smaller than one lattice spacing per cycle, connected to a threshold stress intensity factor range, ΔKth. Below this threshold, the crack either does not grow, or grows very slowly, followed by a very steep increase of da/dN with ΔK. The Paris law, Eq. (3-9), indicating the linear relation¬ship in regime B between log(da/dN) and log(ΔK), is applied only on the segment of the growth curve related to stable fatigue growth. Regime C corresponds to high ΔK values, when the crack propagates fast to final fracture, after reaching the critical stress intensity factor value Kc.

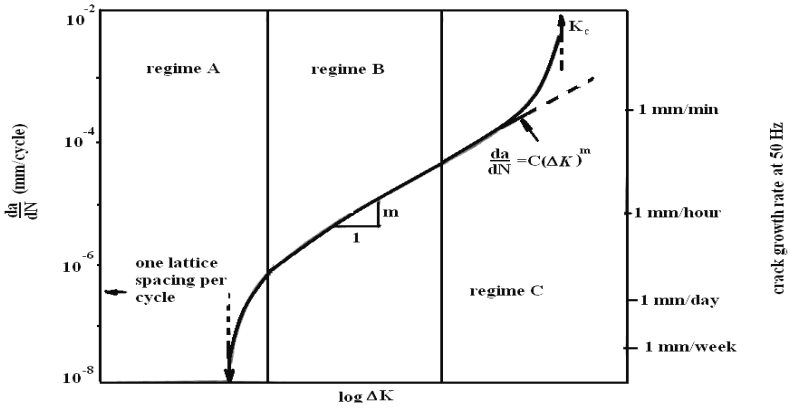

Figure 3—16 Different regimes of stable fatigue crack propagation

3.9.1 Fatigue testing

Specimens were mechanically prepared before testing and foil-strain gauges, used for a crack increment monitoring, were installed on the prepared specimens. 5 mm long, RMF A-5, foil gauges were used in testing procedure. The device for a crack increment registration, FRACTOMAT, Fig. 3-17, was used for monitoring the crack propagation with a foil gauge. The system for a crack increment measuring, FRACTOMAT, and foil gauge register the change in electrical resistance within a foil gauge. Gauge is a thin, resistant, measuring foil installed on a specimen the same way as classic strain gauges. The appearance of the specimen prepared for the testing is shown in Fig. 3-18. As a fatigue crack propagate beneath the foil gauge, it reaps following the fatigue crack tip, which causes the electrical resistance of the foil to linearly alternate with the change of the crack length.

Figure 3—17 High-frequency pulsator FRACTOMAT

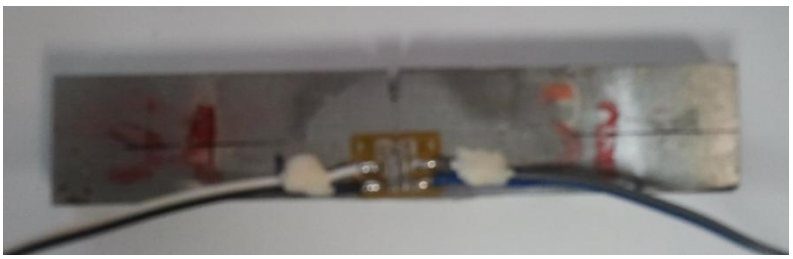

Figure 3—18 Appearance of the prepared specimen for the testing of the fatigue crack growth parameters

The a-N curves are used for a crack propagation rate determination. Calculation procedure consists of approximation in seven consecutive points, with a second degree parabola, starting with the first point of a - N dependence, using the least square method:

$$a_I = b_0 + b_1 N + b_2 N^2 \qquad (3\text{-}11)$$

and then the first derivative is determined in a middle point of a segment. That means that the real curve is approximated by a series of parabolas, from which first goes through the points 1-7, second goes through the points 2-8, third goes through the points 3-9 and so on. The crack propagation rate is determined as a derivative in a middle point (point 4 for the first parabola, 5 for the second, 6 for the third and so on):

$$\frac{da}{dN} = b_1 + 2b_2 N \qquad (3\text{-}12)$$

This way the propagation rate is obtained for the first parabola:

$$a_I = b_{0I} + b_{1I} N_I + b_{2I} N_I^{\,2}, \left.\frac{da_I}{dN_I}\right|_4 = b_{1I} + 2b_{2I} N_{I4} \qquad 3\text{-}13)$$

Propagation rates for other parabolas are determined the same way. Determination of the dependence of a fatigue crack propagation rate, da/dN, and the range of the stress intensity factor, ΔK, comes down to the determination of the coefficient C and the exponent m in the Paris equation. The range of the stress intensity factor, ΔK, which depends on a specimen geometry and crack length, and on the range of the variable force $\Delta F = Fh - Fl$, should be ascribed to the fatigue crack propagation rate for a current crack length, a. Following expression is used for the determination of the stress intensity factor range:

$$\Delta K = \frac{\Delta F \cdot L}{B \cdot \sqrt{W^3}} \cdot f(a/W) \qquad (3\text{-}14)$$

where:

$$f(a/W) = \frac{\sqrt[3]{\frac{a}{W}}}{2\left(1+2\frac{a}{W}\right)\left(1-\frac{a}{W}\right)^{3/2}}\left[1{,}99 - \frac{a}{W}\left(1-\frac{a}{W}\right)\left(2{,}15 - 3{,}93\frac{a}{W} + 2{,}7\left(\frac{a}{W}\right)^2\right)\right] \qquad (3\text{-}15)$$

L - support span, B - specimen thickness, W - specimen width, a- crack length.

Dependences log da/dN = log (ΔK) are calculated and plotted, based on the testing progress. Diagramme for the fatigue crack propagation rate, da/dN, vs. the stress intensity range alteration, ΔK, is shown in Fig. 3-19 for a specimen with a notch in BM. Values of the coefficient C and m for the WM - NZ specimen are given in Table 3-11, together with the BM and HAZ.

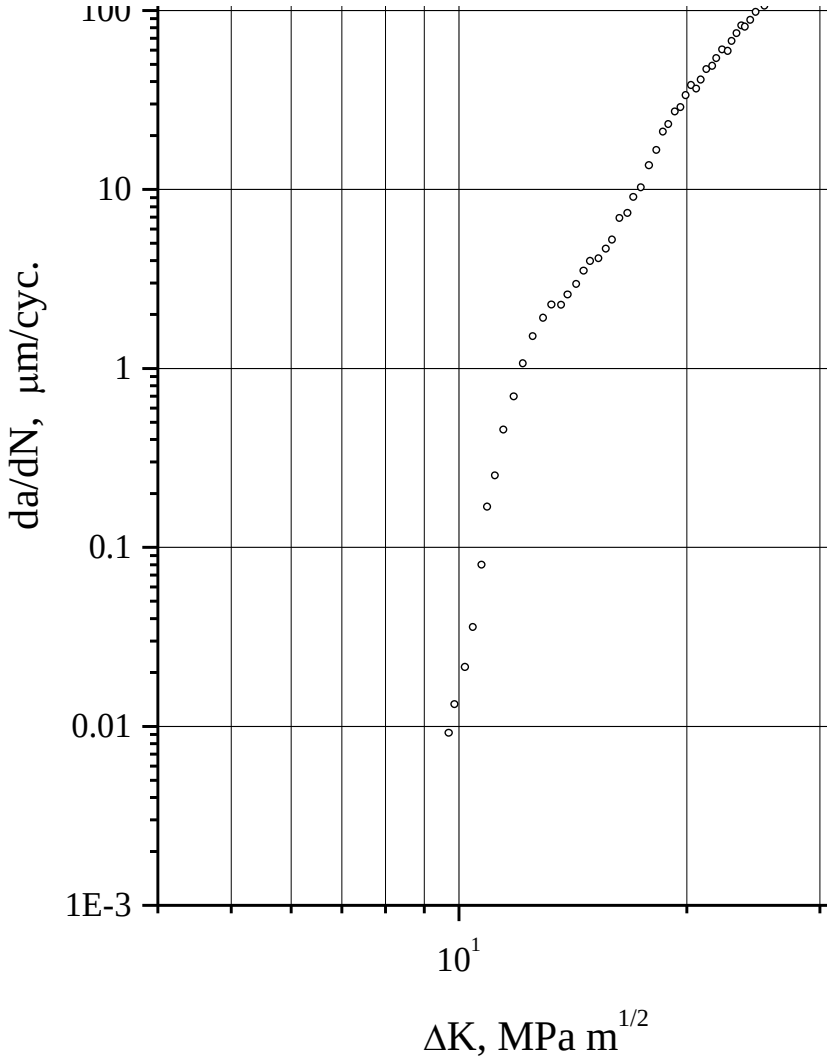

Figure 3—19 Crack growth rate da/dN - ΔK dependency diagram for the BM

Table 3-11 Coefficients in Paris equation for different zones

Propagation zone	**Coefficient C**	**Coefficient n**
WM - NZ	$1.28 \cdot 10^{-10}$	3.1
TMAZ	$1.18 \cdot 10^{-10}$	2.85
HAZ	$1.32 \cdot 10^{-10}$	2.95
BM	$1.22 \cdot 10^{-10}$	2.9

3.10 Stress-strain true curve – application of DIC and ARAMIS

In engineering practice, strain measuring can be performed in various ways. In general, strain measuring techniques can be divided into: contact measuring, i.e. direct measuring (using extensometers, strain gauges…) and non-contact measuring (lasers, cameras, stereography). Non-contact methods have been rapidly developed in recent decades and there is currently a large number of these methods. Some of them include techni¬ques such as "Digital Image Correlation (DIC)", in combination with the ARAMIS system, [63]. This technique is very suitable for strain measurement in heterogeneous materials, such as welded joints, which can be observed as a combination of zones with different properties - base metal (BM), weld metal (WM) and heat affected zone (HAZ), often divided into subzones, [64]. Local properties in different zones of a welded joint can be determined by making micro-specimens and subjecting them to standard testing methods.

Digital Image Correlation is a technique for obtaining numerous data about the deformation of the tested specimen. Measuring is based on comparing series of consecutive images obtained in a specific time interval during testing. Depending on the testing requirements, DIC method can be applied as 2D, using a single camera, or as 3D, using two cameras.

Major advantages of DIC are:

- It is a non-contact technique, making it capable of testing large structures, as well as structures with complex geometry.
- High accuracy, thanks to a type of calibration used in this method, which is adjusted according to the volume of the measured space.
- Post-processing enables different types of results for a single experiment.

The system is applied in solving problems when analyzing structure integrity, determining properties of materials, verifying and refining numerical calculations. Aramis delivers complete 3D surface, displacement and strain results, where a large number of traditional measuring devices are required (strain gauges, LVDTs exten-someters). This software provides all results for static and dynamic tests even at high speeds for smallest to largest components.

Aramis helps to better understand material and component behavior and is well suited to monitor experiments with high temporal and local resolution.

Tracking of coordinates, allows the use of mathematical formulas for determining components of deformation or displacement. Measurements of displacement or deformation can be monitored with one camera - 2D technique or two cameras - stereometric method (Fig. 3-20). Digital cameras continuously monitor components of the structure, for example, a critical section. It is necessary to adequately prepare the observed area before starting the test. When the structure is subjected to load, referent points start to displace, and the grid deforms. Pairs of digitalized images are entered in an ascribed timely fashion by the recording software, and based on differences in displacement of grid points, one can calculate the strain, Fig. 3-21.

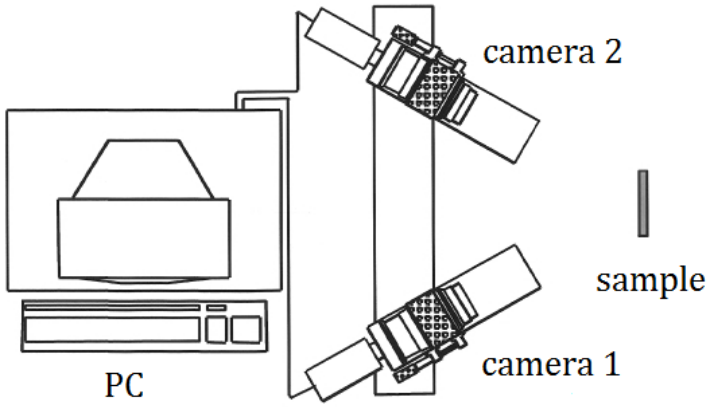

Figure 3—20 Scheme of the system for 3D digital image correlation - stereometric method

Figure 3—21 DIC hardware and software.

Experiment was conducted using 3D system Aramis 2M (GOM, Braunschweig, Germany) and Universal Testing Machine (Instron, USA). In accordance with specimen dimensions, the measuring volume of 100 x 100 x 75mm was defined, and based on it, a calibration panel CP20 90 x 72 was selected. Calibration was performed in thirteen steps, by moving the calibration panel in order to obtain dimensional consistency of the system. Calibration deviation was 0.038

pixels. Prior to recording, a layer of white paint was applied to the measuring surface, followed by a layer of finely dispersed black points (Kenda Color Acril-207ico, Kenda Farben).

Figure 3-22 shows the experiment setup, indicating the jaws of tensile test machine (No. 1), cameras (No. 2), the specimen (No. 3) and the lamp (No. 4). The lamp is used as a source of constant light in order to avoid the influence of variable outside lighting. Figure 3-18 shows the positions of measuring lines. Dotted lines are sections 1 and 2 and represent fusion lines and denote the border between WM and HAZ areas. Measuring lines 2, 3, 5 and 6 were placed 2 - 3 mm away from the HAZ, in the WM. Line 1 is located at the root of the WM, whereas line 4 is located in the same plane as lines 2 and 3 but in the WM front zone.

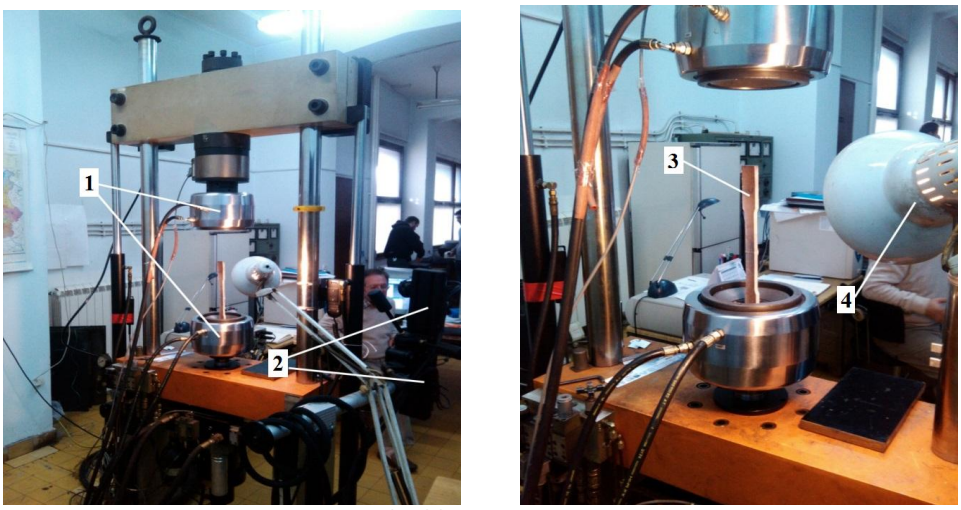

Figure 3—22 Experiment setup

Using measured strains and applied stress, one can get stress-strain curve, as well as true stress – true strain curve if contraction and elongation is also taken into account. The results are shown in Table 3-12 for WM-NZ, in Table 3-13 for TMAZ, in Table 3-14 for HAZ, and in Table 3-15 for PZ.

Table 3-12 Results for true stress and strain for WM-NZ

$\varepsilon \cdot 10^6$	330	600	900	1125	1575	2400	3225	4125
σ (MPa)	22.8	38.5	52.2	68.5	97.8	140.2	215.2	249.0

Table 3-13 Results for true stress and strain for TMAZ

$\varepsilon \cdot 10^6$	525	923	1200	1500	2325	3375	4275
σ (MPa)	37.8	56.9	80.2	98.3	139.7	201.8	248.3

Table 3-14 Results for true stress and strain for HAZ

$\varepsilon \cdot 10^6$	300	750	945	1125	1500	2100	3285	4185	6735
σ (MPa)	18.8	43.5	62.2	71.2	97.5	131.2	210.0	247.5	360.0

Table 3-15 Results for true stress and strain for PZ

$\varepsilon \cdot 10^6$	225	675	1050	1575	2550	3750	4350	12600	24000
σ (MPa)	15.0	33.8	67.5	93.8	165.0	225.0	240.	330.0	365.2

3.11 Concluding remarks

Charpy testing was conducted on a high-speed data acquisition instrument, using instrumented pendulum to separate energies for crack initiation and propagation. Two specimens were used, providing results close enough, so that the average value was used as the relevant one, without noise analysis. This has simplified application of DoE method, since it was possible to make it without calculating (S/N) ratio.

Average values of the total impact energy, as obtained for the 9 experiments, chosen according to the orthogonal matrix, indicated that the travel (welding) speed has the biggest effect (56%), followed by significant effect of the rotational speed (43%), whereas the tool angle has very small effect (1%).

Different effects are obtained when separated energies are considered. In the case of the initiation energy, the rotational speed is the most influential (42%), closely followed by the tool angle (39%), whereas the effect of the welding speed if smaller (19%), but not negligible. In the case of the propagation energy, the rotational speed is still the most influential, even more pronounced (63%), whereas both the tool angle and welding speed effects are significantly lower (21% and 16%, respectively).

The effects of tool angle on the individual energies cancel each other, so the effect on the total energy is negligible.

Another crack resistant property, fracture toughness, has shown similar behaviour, as in the case of the propagation energy, which was reasonable to expect, since in both cases it is crack dominated behaviour, whereas the influence of loading type is obviously small (also reasonable for material which is not exactly brittle). Anyhow, one should notice more pronounced effects, since the rotational speed was rated at 88%, whereas the welding speed and tool angle were rated only at 4% and 8%, respectively. One can conclude that the rotational speed has almost exclusive effect for crack resistance under static loading, keeping its dominance in the case of crack resistance under impact loading, but at the smaller scale.

Microstructural examination revealed all typical characteristics of FSW fracture surface, like onion rings, dimples, shear and cleavage marks, micropores and microvoids, specific grain shape and size. Also, characteristic appearance of different zones were identified (WM-NZ, TMHAZ, HAZ, PM). From the microstructural point of view, the effect of input parameters on crack resistance is not of any significance (min. and max. toughness is 15.05 to 23.75 J, and fracture toughness is even in the smaller range, 55 to 75 MPa$\sqrt{m}$, both indicating mixed mode of fracture with some characteristics of ductile behaviour.

Fatigue crack growth revealed surprisingly small differences meaning that crack resistance fatigue loading is not sensitive to different microstructure. Contrary to other crack resistance testing, where crack was positioned in the WM-NZ, as the most critical region, for different welding conditions, in this case the same welding conditions were chosen (trial 1) to evaluate the effect of microstructure. Anyhow,

not only was this effect small, but it also turned out that the resistance to crack growth in the BM is sufficient for the example used in this thesis, since the crack growth was limited to BM only.

Finally, true stress-strain curves have been identified for all regions of welded joint by using the Digital Image Correlation technique and ARAMIS system. It has been applied as the most suitable for local measurements for strains, enabling evaluation of true stress – true strain curves, needed as an input in the numerical simulation.

4 NUMERICAL SIMULATION OF THE PLUNGE STAGE IN FRICTION STIR WELDING

Numerical modeling is believed to be an reliable method to predict the microstructures and properties of FSW welded joint. A number of publications dealing with numerical investigations of the FSW process can be found in the literature [36-47]. For example, Zhang and co-workers carried out semi-coupled thermomechanical finite element analyses of the FSW process and the associated microstructural changes [37, 38]. In several references, the main objective was to examine the effect of various FSW process parameters (including tool design) on the heat/mass transport processes (e.g. [39-40]). Song and Kovačević [41] and Chen and Kovačević [42, 43] presented numerical thermomechanical modeling of friction stir welding for both similar and dissimilar joints. Some simplified analyses can also be found, such as Dong et al. [44], where several models were developed to separately deal with the thermal and mechanical aspects of the friction stir welding.

Complex thermo-mechanical conditions exists in the near field matrix around the tool during the process which is categorized as thermo-mechanically affected zone (TMAZ) in the welding plate. This is also the zone that affects successful weld formation without a void. TMAZ is mostly in the plastic state and it is experimentally difficult to determine the temperatures in the welding plate due to large deformation of the material. Understanding of the complex thermo-mechanical conditions prevalent during the process in this zone can lead to better control of the weld formation process.

In majority of the literature, the emphasis is on the simulation of the welding process, i.e. the linear welding phase, while plunge stage is rarely examined [36,47,49, 50]. However, plunging is a vital phase of the FSW process, because it creates the initial thermo-mechanical conditions in the material, i.e. conditions prior to the start of the linear welding phase. Also, numerical modeling of the plunging process is very demanding due to the pronounced mesh distortion under the pin, [36,47]. Therefore, besides the numerical analysis, here we compare the numerical results of the temperature change during the plunge stage of the FSW with the experimental data obtained by thermal imaging.

4.1 The basic equations of FEM – thermal problem

The heat generation in the friction stir welding is assumed to be a combination of two different mechanisms: (1) the friction at the tool and work piece interfaces, and (2) the plastic shear deformation of the weld metal in the vicinity of the pin. The heat produced during welding is dissipated via conduction into the work piece, the tool and the backing plate as well as via convection and radiation from the work piece surfaces. The heat loss due to radiation is presumably negligible because of the low temperatures involved with the process and can be combined with the convective heat transfer from the top surface of the plate to the

ambient by utilizing a slightly elevated heat transfer coefficient. The governing equation for heat transfer process during the plunge phase of FSW process can be written as:

$$\rho c\frac{\partial T}{\partial t}=\frac{\partial}{\partial x}\left[k_x\frac{\partial T}{\partial x}\right]+\frac{\partial}{\partial y}\left[k_y\frac{\partial T}{\partial y}\right]+\frac{\partial}{\partial z}\left[k_z\frac{\partial T}{\partial z}\right]+\dot{q}_p \qquad (4.1)$$

where ρ is the density, c is the specific heat, k is heat conductivity, T is the temperature, t is the time, $\dot{q}_p$ is heat generation coming from plastic energy dissipation due to shear deformation, and x, y, and z are spatial coordinate. The rate of heat generation due to plastic energy dissipation, $\dot{q}_p$ is computed from

$$\dot{q}_p=\eta\sigma\dot{\varepsilon}^{pl} \qquad (4.2)$$

where η is the factor of converting mechanical to thermal energy (0.9), [51], σ is the shear stress, and $\dot{\varepsilon}^{pl}$ is the rate of plastic strain.

Heat generation of frictional heating between tool and workpieces can be written as:

$$\dot{q}_f=\frac{4}{3}\pi^2\mu PNR^3 \qquad (4.3)$$

where $\dot{q}_f$ is the frictional heat generation, μ is the coefficient of friction, P is the traction, N is the rotational speed and R is the surface radius.

Application of the finite element method includes domain discretization (division into finite elements), interpolation of all quantities inside finite elements, integration over all elements and solution of the resulting equation system.

By introducing the isoparametric interpolation functions, one can write:

$$T^e(x^i,t)=N^k(x^i)\,T_k(t) \qquad (4.4)$$

where $N^k(x^i)$ is the interpolation function and Tk the nodal temperature.

Now, one can write:

$$\frac{\partial T^e}{\partial x^i}=\frac{\partial N^k}{\partial x^i}T^k=N_i^kT_k;\qquad \frac{\partial T^e}{\partial t}=N^k\dot{T}_k \qquad (4.5)$$

where N^k denotes matrix of nxr order (n is space dimension and r number of elements).

By multiplying eqn. (4.5) by weight function, which is chosen to be identical to N^k, and by integration over each finite element, i.e. by applying the Galerkin procedure, one obtains:

$$\int_{\Omega^e}\left[\frac{\partial}{\partial x^i}\left(k\frac{\partial T}{\partial x^i}\right)+Q-\rho c\dot{T}\right]N^k\,d\Omega=0 \tag{4.6}$$

Integration of the first term requires application of the Gauss theorem, in order to define boundary conditions:

$$\int_{\Omega^e}\frac{\partial}{\partial x^i}(k\frac{\partial T}{\partial x^i})N^k\,d\Omega=\int_{\Omega^e}\frac{\partial}{\partial x^i}(k\frac{\partial T}{\partial x^i}N^k)\,d\Omega-\int_{\Omega^e}k\frac{\partial T}{\partial x^i}N_i^k\,d\Omega=$$

$$=\int_{S^e}k\frac{\partial T}{\partial x^i}n^iN^k\,dS-\int_{\Omega^e}k\frac{\partial T}{\partial x^i}N_i^k\,d\Omega \tag{4.7}$$

Surface integral over S^e is divided according to the boundary division into S1, S2, S3 and S4, which corresponds to the temperature, heat flux, heat convection and radiation boundary conditions:

$T=T_s(x^i)$ at S_1
$q^in^i=qs$ at S_2 (4.8)
$q^in^i=h\,(T_s-T_\infty)$ at S_3
$q^in^i=\sigma\cdot\varepsilon\cdot(T_s-T_\infty)$ at S_4

Taking into account the equations (4.4-4.8) one gets:

$$\int_{G^e}q^in^iN^k\,dG=\int_{S_1}hN^k\,dG-\int_{S_2}q_sN^k\,dG+\int_{S_3}h(T_S-T_\infty)N^k\,dG+\int_{S_4}\sigma\varepsilon(T_S^4-T_\infty)\,dG \tag{4.9}$$

leading to the discretized heat conduction equation:

$$\int_{\Omega^e}\rho cN^kN^i\dot{T}_j\,d\Omega+\int_{\Omega^e}k\delta_{ij}\frac{\partial N^k}{\partial x^i}\frac{\partial N^i}{\partial x^i}T^j\,d\Omega+\int_{s_3}hN^kN^jT_j\,dS+\int_{s_4}\sigma\varepsilon T^4N^k\,dS=$$

$$=\int_{\Omega^e}QN^k\,d\Omega-\int_{s_1}hN^k\,dS+\int_{s_2}q_sN^k\,dS+\int_{s_3}hT_\infty N^k\,dS+\int_{s_4}T_\infty^4\sigma\varepsilon N^k\,dS \tag{4.10}$$

which can be written in matrix form as follows:

$$C^{kj}\dot{T}_j+(K_c^{kj}+K_h^{kj}+K_r^{kj})T_j=R_Q^k+R_T^k+R_q^k+R_h^k+R_r^k \tag{4.11}$$

where C^{kj} denotes heat capacity matrix, K_c^{kj}, K_h^{kj}, K_r^{kj} heat conduction, convection and radiation transfer matrices, respectively (the last two matrices are determined only for the elements where appropriate boundary conditions are defined) and R_Q^k, R_T^k, R_q^k, R_h^k, R_r^k heat load vector due to volume heat source, prescribed temperature, heat flux, convection and radiation, respectively.

Equation (4.11) can be solved by explicit or implicit procedure, asdefined in ABAQUS.

In Abaqus/Explicit the heat transfer equations are integrated using the explicit forward-difference time integration rule [8] and [9]:

$$T_{i+1}^{N} = \Delta t_{i+1}\theta\dot{T}_{i}^{N} + T_{i}^{N} \tag{4.12}$$

where TN is the temperature at node N and the subscript i refers to the increment number in an explicit dynamic step. The forward-difference integration is explicit in the sense that no equations need to be solved when a lumped capacitance matrix is used. The forward Euler scheme does not have to solve equations when the lumped capacitance matrix is used. This makes it explicit. The discretized equation for heat balance is

$$S = C\dot{T}_{i}^{N} + BT_{i}^{N} \tag{4.13}$$

where S is the applied nodal thermal source vector, C is the lumped capacitance matrix and B is the conductance matrix. Combining equations (4.12) and (4.13) gives the final expression for the temperature:

$$T_{i+1}^{N} = \Delta t_{i+1}\left[C^{-1}\left(S - BT_{i}^{N}\right)\right] + T_{i}^{N} \tag{4.14}$$

4.1.1 Governing Equations for Mechanical Analysis

The equation of motion or mechanical response of the welding plate is given by:

$$p = \rho\ddot{u} + ku \tag{4.15}$$

where ρ is the density, k the stiffness coefficient, p the body force and u is the displacement vector. In an FE framework, equation is discretized into

$$P = M\ddot{u} + Ku \tag{4.16}$$

where M is the discrete mass matrix, K the stiffness matrix, P the vector of external discrete forces, which include body forces, surface forces and concentrated loads acting on the system, and u, ů and ü are the nodal displacement, velocity and acceleration vectors, respectively. The nodal acceleration vector in the beginning of a time increment is obtained as:

$$\ddot{u}_{i}^{N} = M^{-1}(P - Ku_{i}^{N}) \tag{4.17}$$

where i denotes the time step. The equation for the velocity of the body is integrated using an explicit central difference scheme as follows:

$$\dot{u}_{i+\frac{1}{2}}^{N} = \frac{\Delta t_{i+1} + \Delta t_{i}}{2}\ddot{u}_{i}^{N} + \dot{u}_{i-\frac{1}{2}}^{N},\quad u_{i+1}^{N} = \Delta t_{i+1}\dot{u}_{i+\frac{1}{2}}^{N} + u_{i}^{N} \tag{4.18}$$

Combining equations (4.16), (4.17), and (4.18) gives the final explicit expression for the velocity:

$$u_{i+1}^{N} = \Delta t_{i+1}\left[\frac{\Delta t_{i+1} + \Delta t_i}{2}\left\{M^{-1}(P - Ku_i^N)\right\} + \dot{u}_{i-\frac{1}{2}}^{N}\right] + u_i^N \qquad (4.19)$$

4.2 The application of FEM

Here we investigate a plunge phase, which is schematically shown in Fig. 4-1, using 3D finite element model. A coupled thermo-mechanical three-dimensional FE model has been developed in ABAQUS/Explicit using the arbitrary Lagrangian–Eulerian formulation and the Johnson-Cook material law, [52]. The contact forces are modeled by Coulomb's Law of friction, making the contact condition highly solution dependent.

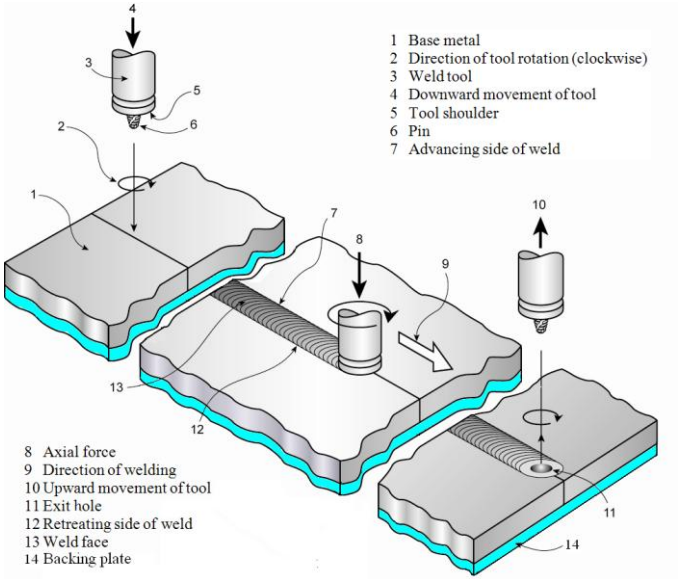

Figure 4—1 Schematic illustration of FSW process

The purpose of this investigation was to investigate the effect of different shapes of tools. Therefore, two different shapes of tools are used, the first one with a conical shoulder with angle of 10° and the second one with a flat shoulder. The welding plate in the numerical model is dimension 50 x 50 mm and 6 mm in thickness. A coupled thermo-mechanical model was developed to study the temperature fields of alloy AA5083-H116 under rotating speed of 400 r/min, during the friction stir welding (FSW) process, [36,47]. A three-dimensional finite element model (FEM) of the plunge stage was developed using the commercial code ABAQUS to study the thermo-mechanical processes involved during the plunge stage, [36, 47].

In this analysis, temperature, displacement and mechanical responses are determined simultaneously. The heat generation in FSW can be divided into three

parts: frictional heat generated by the tool shoulder, frictional heat generated by the tool pin, and heat generated by material plastic deformation near the pin region.

Tools consist of a shoulder and a pin. The design of shoulder and pin is very important for the quality of weld. Pin generates the heat and stirs the material, and shoulder also plays an important part by providing additional frictional treatment, as well as preventing the plastically deformed material to escape from the weld region. Numerical results indicate that the maximum temperatures of the plunge stage in friction stir welding are higher by using tool with a flat shoulder than by using tool with a conical shoulder for the same rotation speed. The plastically deformed material is extruded from the leading to the trailing side of the tool but is trapped by the conical shoulder which moves along the weld to produce a smooth surface finish.

Friction stir welding has two different stages including a plunge and a linear welding phase as shown in Figure 4-1. In the plunge stage, a FSW tool penetrates the workpieces to be welded. In the linear welding phase, the tool moves along the joint line. The whole process adds frictional heat with intense plastic deformation to generate joints and the plunge stage of FSW process is crucial since most of the thermomechanical conditions are initiated and the highest temperature and forces are required in this stage during the whole process. Here the plunge stage using three-dimensional finite element mode and two different tools was investigated.

4.2.1 Material properties

In the present work, material of the welding plate is AA5083-H116. The thermal and mechanical properties used in this model are given in Table 4-1.

Table 4-1 Material properties of AA5083-H116 [2]

MATERIAL PROPERTIES OF AA5083-H116	
Young's Modulus of Elastic. (GPa)	71
Poisson´s Ratio	0.33
Tensile Yield Strength (MPa)	228
Ultimate Tensile Strength (MPa)	317
Thermal Conductivity (W/mK)	117
Coefficient of Thermal Expansion ($°C^{-1}$)	$23.8x10^{-6}$
Density (kg/m^3)	2660
Specific Heat Capacity (J/Kg °C)	900

The material of the tool is steel 155CrVMo121. The material of the backing plate is steel 42CrMo4.

4.2.2 Model Description - Geometry and finite element mesh

The model consists of a deformable workpiece, a rigid stir welding tool and a rigid backing plate. The welding plate in the numerical model is dimension 50 x 50 mm and 6 mm in thickness. For three-dimensional numerical model used is C3D8RT element type which is a thermo-mechanically coupled hexahedral element with 8-

nodes each having trilinear displacement and temperature degrees of freedom. This element produces uniform strain (first-order reduced integration) and contains hourglass control [36,47]. The mesh consists of 27,900 nodes and 25,166 elements.

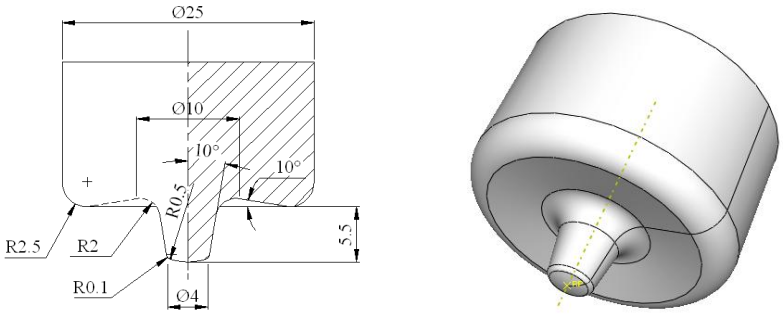

Figure 4—2 Conical shoulder tool with angle of 10°

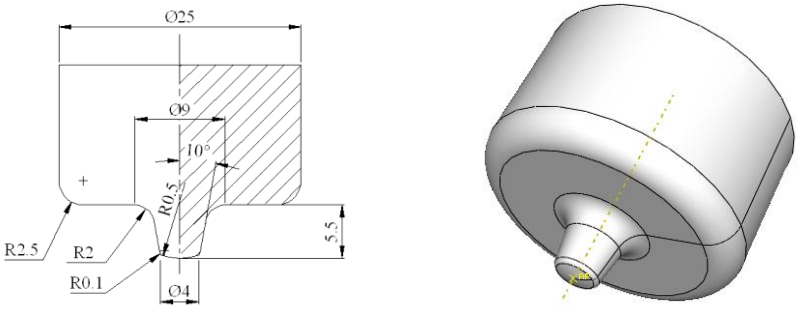

Figure 4—3 Welding tool with a flat shoulder

The tool and the backing plate is modelled as a rigid surface having no thermal degrees of freedom. The main tool geometry in the FE model is similar to the experimental tool. This numerical simulation of the plunge stage in friction stir welding using two different tools. The first tool have a conical shoulder with angle of 10° - figure 4-2 and the second tool have a flat shoulder – figure 4-3. The numerical model of welding plate, tool and backing plate is shown in figure 4-4.

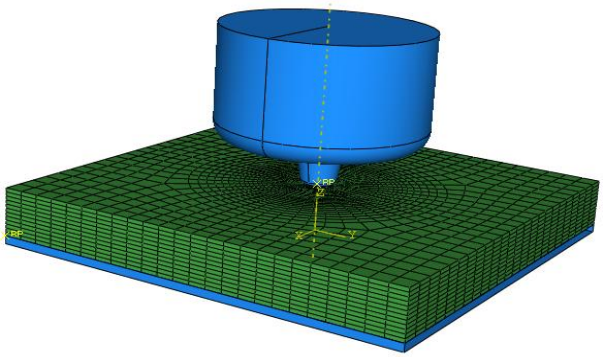

Figure 4—4 Numerical model of welding plate, tool and backing plate

4.2.3 Johnson-Cook elastic–plastic model

In order to avoid the unacceptable mesh distortion caused by the large deformation process, a thermo-mechanical finite element model based on the arbitrary Lagrangian-Eulerian formulations and the adaptive meshing were employed in this study. Adaptive meshing in ABAQUS/Explicit combines features of Lagrangian and Eulerian analyses and is referred to as an ALE analysis. The selection of an appropriate constitutive law to reflect the interaction of flow stress with temperature, plastic strain and strain rate is essential for modeling the FSW process. For this reason the temperature and strain rate-dependent elastic-plastic Johnson-Cook law is selected for this model. The elastic–plastic Johnson–Cook material law is given by:

$$\sigma_y = \left[A + B(\varepsilon_p)^n\right]\left[1 + C\left(\frac{\dot{\varepsilon}_p}{\dot{\varepsilon}_o}\right)\right]\left(1 - \left(\frac{T - T_{room}}{T_{melt} - T_{room}}\right)^m\right) \qquad (4.12)$$

where is Tmelt =620 °C the melting point or solidus temperature, Troom =20 °C the ambient temperature, T(°C) the effective temperature, A=167(MPa) the yield stress, B=596(MPa) the strain factor, n=0.551 the strain exponent, m=0.859 the temperature exponent, C=0.001 the strain rate factor. A, B, C, n, Tmelt, Troom and m are material/test constants for the Johnson-Cook strain rate dependent yield stress for AA5083-H116.

In brief, the coupled thermo-mechanical model was developed to study the temperature fields of alloy AA5083-H116 under rotating speed of 400 r/min, during the plunge stage in friction stir welding (FSW) process. The heat transfer through the bottom surface of the workpiece is controlled by the heat transfer coefficient of 1000 W/m2 K. A constant friction coefficient of 0.3 is assumed between the tool and the workpiece and the penalty contact method is used to model the contact interaction between the two surfaces. Heat convection coefficients on the surface of the workpiece are h=10 W/m2K with the ambient temperature of 20 0C.

4.3 Results and discussion

Figures 4-5 and 4-6 show the temperature fields in the transverse cross section near the tool/matrix interface after 28.5 s. This transient temperature field is symmetric. The maximum temperature is lower than the melting point of the welding material (Tmelt = 620 (°C)). The welding temperature created by FSW ranges from 80 to 90% of the melting temperature of the welding material.

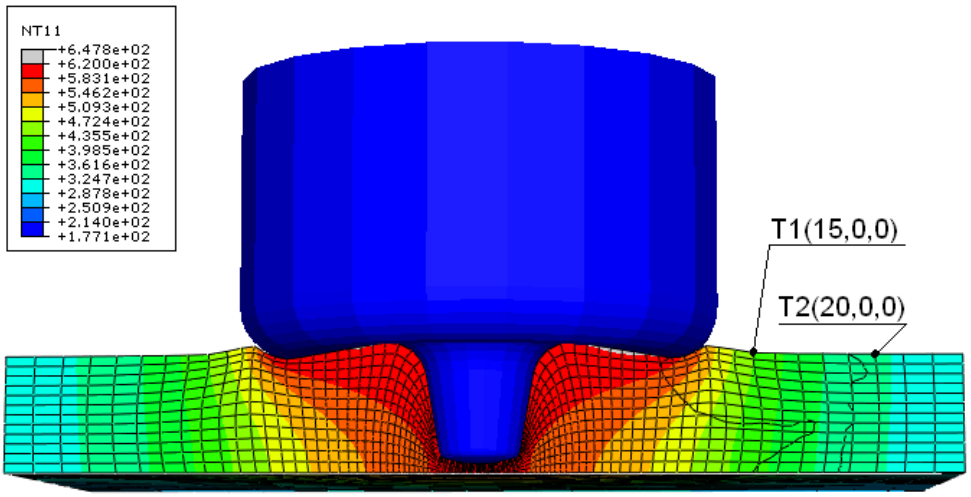

Figure 4—5 Temperature fields in the transverse cross section near the tool/matrix interface after 28.5 s, rotation speeds 400 r/min, conical shoulder tool with angle of 10°.

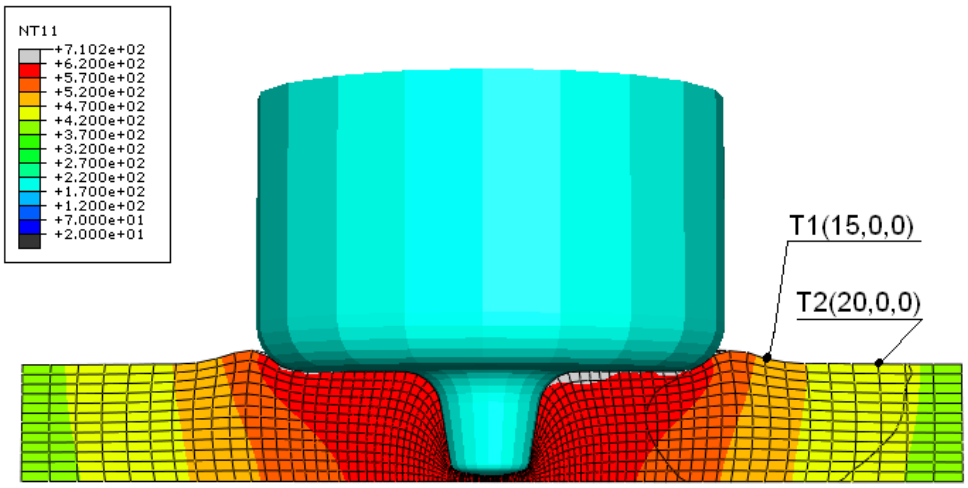

Figure 4—6 Temperature fields in the transverse cross section near the tool/matrix interface after 28.5 s, rotation speed 400 r/min, flat shoulder tool.

Tools have a different shoulder and same a pin. At the start of FSW, during plunging of the pin, until the moment of contact between tool shoulder and the welding plate, the heat generated is same for both tools. Tool with a flat shoulder is the first made contact between shoulder and the welding plate. This is longer the time of friction between the tool shoulder and welding plate which results in more heat generated in the plunge phase.

Figures 4-7 and 4-8 shows typical temperature distribution over one-half of the workpiece obtained by cutting along transverse directions. It's the temperature field of the plunge stage after 28.5 s when rotation speeds is 400 r/min. The plunge depth is 5.7 mm. The tool plunge velocity is set to a uniform value of 0.2 mm/s.

This temperature field is symmetric. The concavity is designed to provide a reservoir of material above the original crown surface of the weld, facilitate transport of material around the tool and reduce plate thinning in the weld zone. The plastically deformed material is extruded from the leading to the trailing side of the tool but is trapped by the conical shoulder which moves along the weld to produce a smooth surface finish. On the advancing side of the crown of the weld, a lip forms where weld metal is rolled over onto the base metal. This lip is often called "flash" and can be minimized, but not eliminated, by a proper choice of welding parameters and tool design - with a conical shoulder.

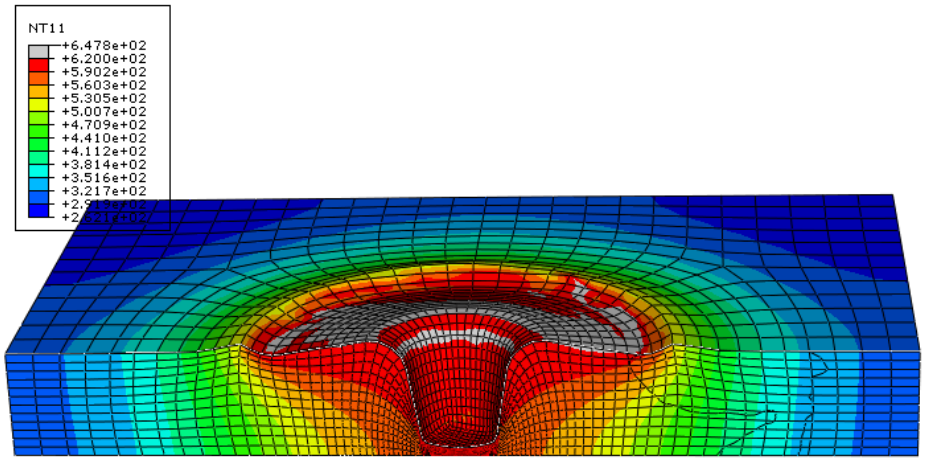

Figure 4—7 Temperature distribution in aluminum AA5083-H116 at the end of a 28.5 s plunge. Conical shoulder tool with angle of 10°.

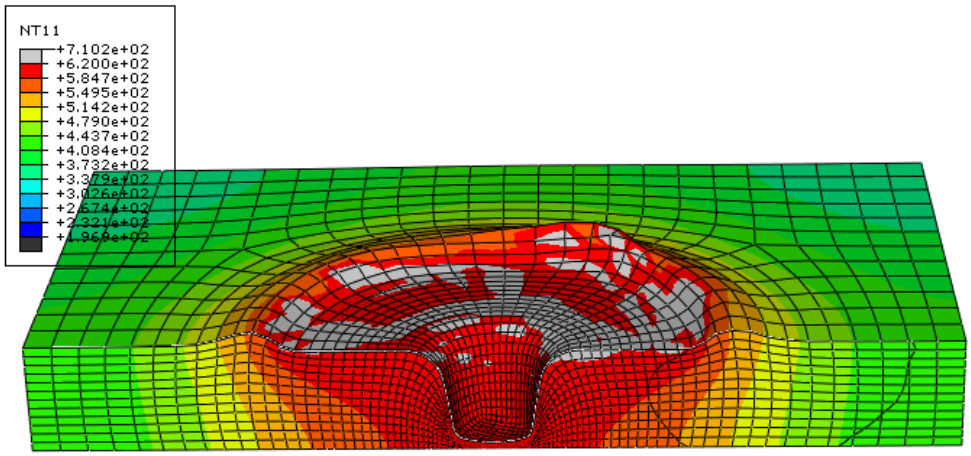

Figure 4—8 Temperature distribution in aluminum AA5083-H116 at the end of a 28.5 s plunge. The welding tool with a flat shoulder.

Figures 4-9 and 4-10 shows the temperature dependence of the time for plunge stage, when rotation speeds is 400 r/min in the points T1 (15,0,0) and T2(20,0,0). Numerical results indicate that the maximum temperatures of the plunge stage in friction stir welding are higher by using tool with a flat shoulder than by using tool with a conical shoulder for the same rotation speed.

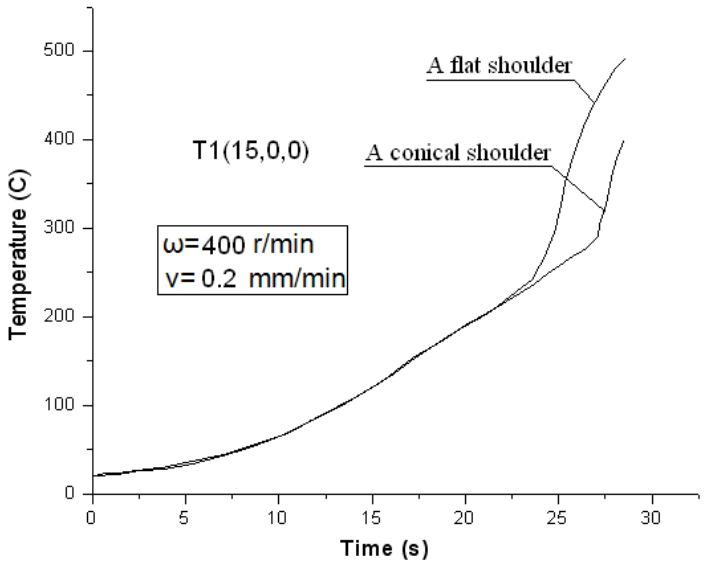

Figure 4—9 Temperature dependence of the time (point T1)

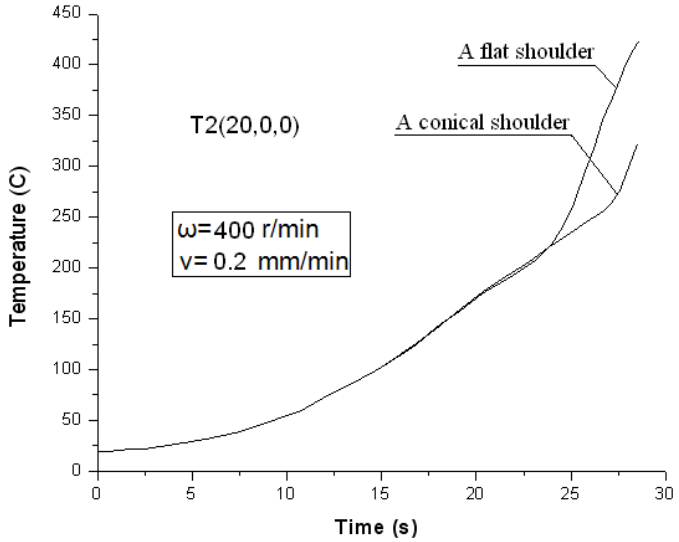

Figure 4—10 Temperature dependence of the time (point T2)

4.4 Concluding remarks

Based upon results and discussion one can make following conclusions:

- The finite element method is capable of simulating the plunge phase of FSW, if applied correctly, as shown here, and also verified by experiments, as shown in [40]. The linear phase of FSW, as a simpler one, has not been analysed here, but has been also verified by Veljic et al, [40], using the same approach as presented here.
- The temperature in the matrix is lower than the melting temperature.
- The concavity is designed to provide a reservoir of material above the original crown surface of the weld, facilitate transport of material around the tool and reduce plate thinning in the weld zone.
- The "flash" can be minimized, but not eliminated, by a proper choice of welding parameters and tool design - using tool with a conical shoulder.
- The maximum temperatures of the plunge stage in friction stir welding are higher by using tool with a flat shoulder than by using tool with a conical shoulder for the same rotation speed. Therefore, the conical shoulder is more suitable for most of the practical use, since it enables smaller temperature gradients and more favourable stress-strain state.
- The finite element method can used to replace expensive experiments, once the model is verified.

5 FATIGUE CRACK GROWTH

5.1 Introduction

Long history of application of Finite Element Method - FEM, greatly contributed to solving of numerous complex engineering problems. Calculation and analysis of stress-strain state within the structure enables high quality assessment of structural integrity. This contribution is especially significant for structural analysis of important structural parts, i.e. load-bearing components. Long and expensive laboratory tests have been replaced with considerably cheaper software packages for calculation of structures. The application of numerical methods to discretized 2D and 3D structure models, along with laws of fracture mechanics, enabled solving of problems mentioned above in a comfortable way, as shown in [53-58].

In the case of non-stationary crack calculation, i.e. when its propagation within the structure is observed, application of this method is not a simple task. This is due to the need to perform "splitting" of a finite element at the previously formed crack tip for each propagation step and then generate a new finite element mesh in the same region. Hence, applying FEM becomes far more complicated. However, the method was impro-ved by developing the so-called eXtended Finite Element Method (XFEM), [53, 59]. This new method found wide application in some of the existing finite element software packages (including ABAQUS, which is used in this work), and it made a significant contribution to structural integrity assessment, [60, 61].

5.2 The xFEM

The extended finite element method, Xfem, does not require the finite element mesh to conform to cracks, on one hand side, and provides usage of higher-order elements or special finite elements without significant changes in the FEM formulation, on the other hand side. Basis of the method is proposed by Belytchko and Black [53], and presented in [54] for the two-dimensional cracks.

The Xfem simply sub-divides a model problem into two parts, [55]: mesh generation for the geometric domain (cracks not included), and enriching the finite element approximation by additional functions, to model the crack singularity. Modeling crack growth in a traditional finite element framework is complicate because the mesh has to match the geometry of the discontinuity, what typically requires re-meshing of the domain at each time step. In the Xfem the mesh is not changed as the crack grows since it is independent of the location and geometry of the crack. The enriching functions are divided into two distinct types: discontinuity functions and asymptotic crack-tip function. The discontinuities across the crack faces are modeled by Heaviside step function. While

the displacement field near crack tip simulates using trigonometry functions derivates from the basic formulation of Westergaard for the displacement field in Near of the crack Tip. Near Tip (NT) functions are defined by linear elastic crack tip displacement field, i.e., asymptotic crack tip stress field (broken line in Figure 5-1).

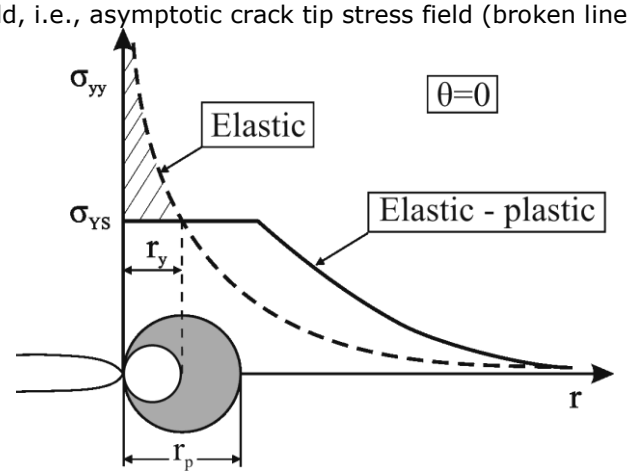

Figure 5—1 Stress field near the crack

5.2.1 The method of discontinuous enrichment

The method of discontinuous enrichment is presented here to illustrate how the two-dimensional formulation can be enriched for the crack model. The concept of incorporating local enrichment in the finite element partition of unity was introduced in Melenk and Babuska [56]. The essential feature is multiplication of the enrichment functions by nodal shape functions. The approximation for a vector-valued function $\mathbf{u}^h(\mathbf{x})$ with the partition of unity enrichment has the general form [56]:

$$\mathbf{u}^h_{\text{enr}}(\mathbf{x}) = \sum_{I=1}^{N} N_I(\mathbf{x}) \left(\sum_{\alpha=1}^{M} F_\alpha(\mathbf{x})\, \mathbf{b}_I^\alpha \right) \tag{5.1}$$

where N_I, $I=(1,N)$ are the finite element shape functions, $F_\alpha(\mathbf{x})$, $\alpha=(1,M)$ are the enrichment functions and $\mathbf{b}_I^\alpha$ is the nodal enriched degree of freedom vector associated with the elastic asymptotic crack-tip function that has the form of the Westergaard field for the crack tip. In particular case, for the crack, the enriched displacement approximation, using Heaviside and Near Tip functions, following [5-6], is written as:

$$\mathbf{u}^h(\mathbf{x}) = \sum_{I\in N_{\text{all}}} N_I(\mathbf{x}) \left(\mathbf{u}_I + \underbrace{H(\mathbf{x})\mathbf{a}_I}_{I\in N_{\text{sd}}} + \underbrace{\sum_{\alpha=1}^{4} F_\alpha(\mathbf{x})\, \mathbf{b}_I^\alpha}_{I\in N_{\text{tip}}} \right) \tag{5.2}$$

where $\mathbf{u}_I$ is the nodal displacement vector associated with the continuous part of the finite element solution, $\mathbf{a}_I$ is the nodal enriched degree of freedom vector associated with the Heaviside (discontinuous) function. The $\mathbf{x} \equiv (x, y)$ denotes Cartesian coordinates in 2D space. We denote by N_u the set of all nodes in the domain, and N_a the subset of nodes enriched with the Heaviside function, and N_b is the subset of nodes enriched with the NT (Near Tip) functions.

5.2.2 Enrichment Functions

The enrichment is able to take a local form only by enriching those nodes whose support intersects a region of a crack. Two distinct regions are identified for the crack geometry, precisely, one of them is the crack interior and the other is the near tip region as it is shown in Fig. 5-2. In the Figure is shown a region of a crack for enrichment by H and NT functions. The circled nodes are enriched with a discontinuous function, while the squared nodes are enriched with NT functions.

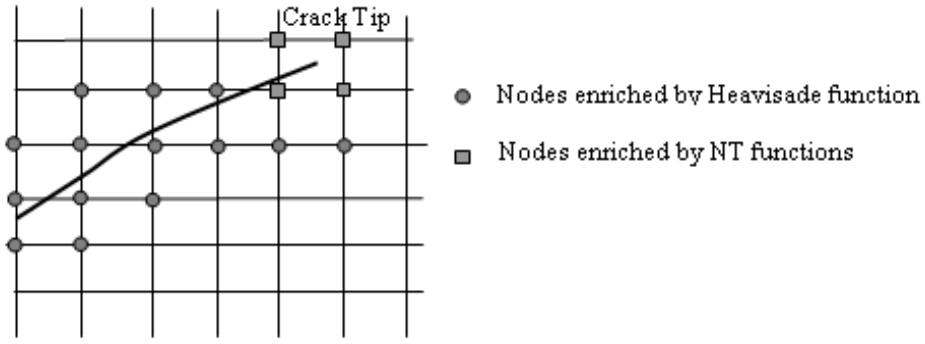

Figure 5—2 Regions for standard enrichment near the edges of the crack [56]

5.2.3 Generalized Heaviside Function

The interior of the crack (Γ_c is the enrichment – domain) is modeled by the generalized Heaviside enrichment function $H(\mathbf{X})$, where $H(\mathbf{X})$ takes the value +1 above the crack and −1 below the crack [5-6]:

$$H(\mathbf{X}) = \begin{cases} 1 \text{ if } (\mathbf{X} - \mathbf{X}^*) \cdot \mathbf{n} \geq 0 \\ -1 \text{ if } (\mathbf{X} - \mathbf{X}^*) \cdot \mathbf{n} < 0 \end{cases} \tag{5.3}$$

where $\mathbf{X}$ is the sample (Gauss) point, $\mathbf{X}^*$ (lies on the crack) is the closest point to $\mathbf{X}$, and $\mathbf{n}$ is unit outward normal to crack at $\mathbf{X}^*$ (Fig. 5-3). It can be seen that in the first published works [53,54], above shape modeling of the discontinuity was not used. The formulation (5-3) was introduced due to practical numerical reasons.

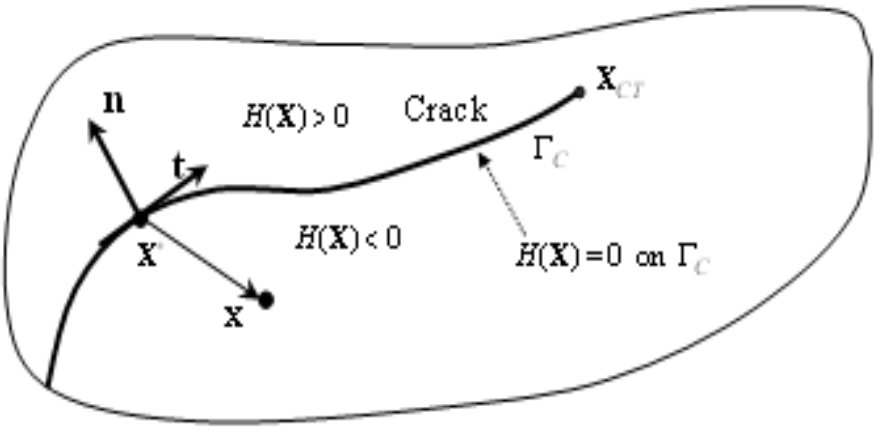

Figure 5—3 Values of the Heavisade function above and below the crack

The crack tip enriched functions ensure that the crack terminates precisely at the location of the crack-tip. The linear elastic asymptotic crack-tip fields serve as suitable enrichment functions for providing the correct near-tip behavior, [54,56].

The crack tip enrichment functions in isotropic elasticity have form of the Westergaard field for the crack tip:

$$F(\mathbf{x}) = \{F_1, F_2, F_3, F_4\} = \left[\sqrt{r}\cos\frac{\theta}{2}\ , \sqrt{r}\sin\frac{\theta}{2}\ , \sqrt{r}\sin\frac{\theta}{2}\sin\theta,\ \sqrt{r}\cos\frac{\theta}{2}\sin\theta \right] \tag{5.4}$$

where r and θ denote polar coordinates in the local system at the crack tip. It can be noted that the second function in eqn. (5-4) is discontinuous over there crack faces [53, 54].

The discontinuity over the crack faces can be obtained using other functions like Heaviside function (5.3), which have discontinuity. Let the element which contain the crack tip is denoted as CT element. In the papers [56,57] the discontinuity behind the tip in the CT element is accomplished by second function of the eqn. (5.4). In this paper (Fig. 5-4), the discontinuity in the CT element we have achieved with Heaviside function (5.3).

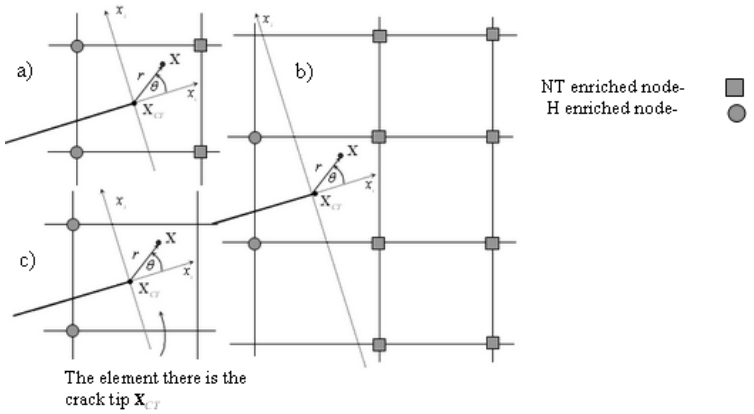

Figure 5—4 The local enriched nodes of an element with crack tip: a) standard (H+NT) enriched; b) enlarged (H+NT)* enriched; c) only (H) enriched

5.2.4 The Weak Form of the Governing Equations, [55]

To introduce a concept of discontinuous enrichment, we begin by considering the domain of the problem Ω bounded by Γ, with an internal boundary Γ as it is shown in Fig. 5-5. The boundary Γ is subdivided into two parts: Γ_u and Γ_t. The displacement is prescribed on Γ_u, and traction is prescribed on Γ_t. In addition to the external boundary, the crack surface presents an additional boundary inside Ω. The crack surface is denoted by Γ_c and is traction free; Γ_c consists of: Γ_c^+ and Γ_c^-, two coincident surfaces and crack surface is traction free.

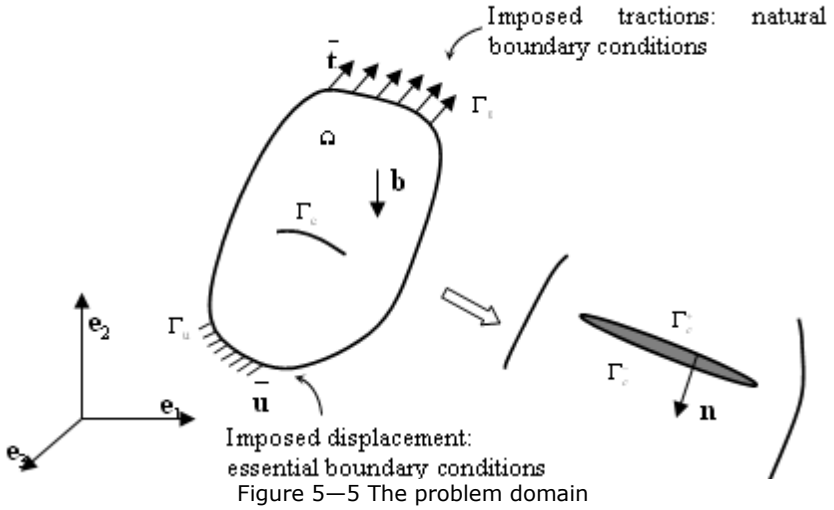

Figure 5—5 The problem domain

The discrete weak form is:

$$\int_{\Omega^h} \sigma_{ij}\, \delta\varepsilon_{ij}^h \, \mathrm{d}\Omega = \int_{\partial\Omega^h} \bar{t}_i \;\; \delta u_i^h \, \mathrm{d}\Gamma \qquad \forall \delta u_i^h \in U_0^{hh} \tag{5-5}$$

where: Ω^h is the finite element domain, σ_{ij} is the Cauchy stress tensor, u_i are the displacement components $u_i^h \in U_0^h$ and $\delta u_i^h \in U_0^{hh}$, are the approximating trial and test functions used in the X-FEM, are traction components and the sum has repeated indices. The space U^{hh} is the enriched finite element space that satisfies the Dirichlet boundary conditions, and which include the base functions that are discontinuous across the crack surfaces. The space U_0^{hh} is the corresponding space with homogeneous Dirichlet boundary conditions.

Substituting the X-FEM trial and test functions in to the above equations, and using the arbitrariness of nodal variations, the following discrete system of linear equations on an element-by-element is:

$$\begin{bmatrix} \mathbf{k}_{ij}^{uu} & \mathbf{k}_{ij}^{ua} & \mathbf{k}_{ij}^{ub} \\ \mathbf{k}_{ij}^{au} & \mathbf{k}_{ij}^{aa} & \mathbf{k}_{ij}^{ab} \\ \mathbf{k}_{ij}^{bu} & \mathbf{k}_{ij}^{ba} & \mathbf{k}_{ij}^{bb} \end{bmatrix} \begin{Bmatrix} \mathbf{d}_i^u \\ \mathbf{d}_i^a \\ \mathbf{d}_i^b \end{Bmatrix} = \begin{Bmatrix} \mathbf{f}_i^u \\ \mathbf{f}_i^a \\ \mathbf{f}_i^b \end{Bmatrix} \tag{5-6}$$

where: $\left\{ \mathbf{d}_i^u \;\; \mathbf{d}_i^a \;\; \mathbf{d}_i^b \right\}^T$ is the vector of nodal unknowns, $\left\{ \mathbf{f}_i^u \;\; \mathbf{f}_i^a \;\; \mathbf{f}_i^b \right\}^T$ the external force vector, $\mathbf{K}_e$ - elemental tangent stiffness matrix. The sub-matrices and vectors that appear in Eq. (5-6) are defined as:

$$\begin{aligned} \mathbf{k}_{ij}^{rs} &= \int_{\Omega_e} \left(\mathbf{B}_i^r \right)^T \mathbf{C}\, \mathbf{B}_j^s \, \mathrm{d}\Omega \\ \mathbf{f}_i^u &= \int_{\partial\Omega_i^h \cap \partial\Omega_e} N_i \, \bar{\mathbf{t}} \, \mathrm{d}\Gamma \\ \mathbf{f}_i^a &= \int_{\partial\Omega_i^h \cap \partial\Omega_e} N_i \, \mathrm{H}\bar{\mathbf{t}} \, \mathrm{d}\Gamma \\ \mathbf{f}_i^{b_\alpha} &= \int_{\partial\Omega_i^h \cap \partial\Omega_e} N_i \, F_\alpha \, \bar{\mathbf{t}} \, \mathrm{d}\Gamma, \quad (\alpha = 1,4) \end{aligned} \tag{5-7}$$

In the above equations, N_i is the standard finite element shape function that is defined by $i\left(i = 1, nen\right)$ of the finite element, where nen is the number of

nodes in the connectivity of the finite element. In eq. (5-7), $\mathbf{B}_i^u$, $\mathbf{B}_i^a$, and $\mathbf{B}_i^{b_\alpha}$ are the standard strain interpolation matrices.

5.3 Modelling

5.3.1 Material

Friction Stir welded joint is shown schematically in Fig. 5-6, indicating four different zones: the base metal (BM) or parent zone (PZ), the weld metal (WM) - nugget, the heat affected zone (HAZ), the thermo-mechanically affected zone (TMAZ). Mechanical properties, are given as follows:

- in Tab. 5-1 for Young's Modulus and Poisson's coefficient, the same value in the whole welded joint;
- elasto-plastic: different stress-strain relations for different zones, Tab. 5-2, taken from the experimental results, as shown in Ch. 3.10;
- fatigue crack propagation: Paris law constants, C and n, Tab. 5-3, taken from the experimental results, as shown in Ch. 3.9.

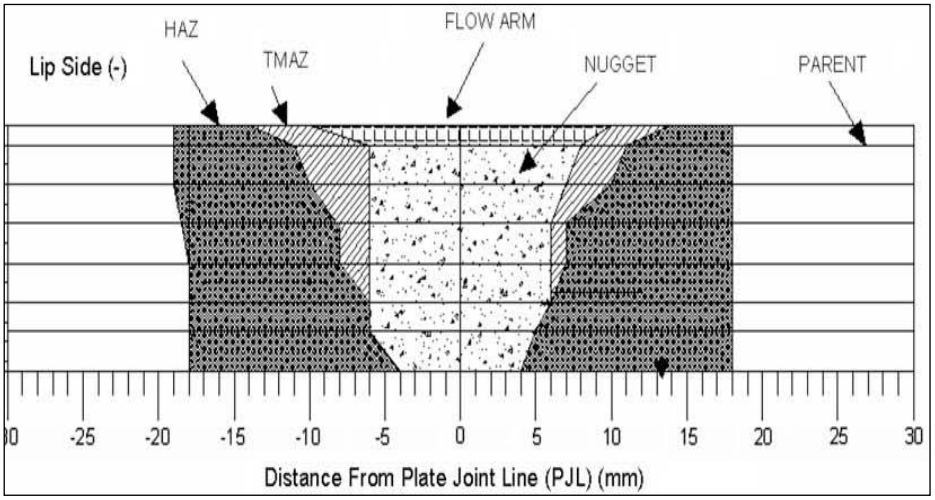

Figure 5—6 Schematic presentation of zones in friction stir welded joint

Table 5-1 Tensile properties of different zones in friction stir welded joint made of Al

FSW zone	nugget	TMAZ	HAZ	PZ
Young's modulus E (GPa)	68	68	68	68
Poisson's coefficient v	0.33	0.33	0.33	0.33

Table 5-2 Stress-strain data for different zones in friction stir welded joint

nugget		TMAZ		HAZ		PZ	
σ/MPa	**ε/-**	**σ/MPa**	**ε/ -**	**σ/MPa**	**ε/ -**	**σ/MPa**	**ε/ -**
22.82	0.000330	37.76	0.000525	18.75	0.000300	15.00	0.000225
38.48	0.000600	56.90	0.000923	43.50	0.000750	33.75	0.000675
52.17	0.000900	80.18	0.001200	62.25	0.000945	67.50	0.001050
68.48	0.001125	98.27	0.001500	71.25	0.001125	93.75	0.001575
97.82	0.001575	139.66	0.002325	97.50	0.001500	165.00	0.002550
140.21	0.002400	201.72	0.003375	131.25	0.002100	225.00	0.003750
215.22	0.003225	248.27	0.004275	210.00	0.003285	240.00	0.004350
248.93	0.004125			247.50	0.004185	330.00	0.012600
				360.00	0.006735	365.25	0.024000

Table 5-3 Constants in Paris equation for different zones in friction stir welded joint

FSW zones	**Paris's model constants**	**value**
nugget	*C*/ cycles^{-1}	$1.28 \cdot 10^{-10}$
	n	3.1
TMAZ	*C*/ cycles^{-1}	$1.18 \cdot 10^{-10}$
	n	2.85
HAZ	*C*/ cycles^{-1}	$1.32 \cdot 10^{-10}$
	n	2.95
PZ	*C*/ cycles^{-1}	$1.22 \cdot 10^{-10}$
	n	2.9

5.3.2 Numerical modelling of crack propagation in plate with two FSW T joints

Numerical simulation of crack propagation in a structure with welded joints consists of the following stages:

1. Creating 2D or 3D models, including the modelling of an initial crack (shape, dimensions and location within the structure).
2. Defining the materials, i.e. mechanical properties for each welded joint zone, including the base metal.
3. Determining the loading (its intensity and type, as well as location).
4. Defining the boundary conditions (e.g. connection with the rest of the structure-assembly).
5. Generating the finite element mesh, whereby it is important to select the appropriate element type and mesh density. Therefore, the mesh is refined around the initial crack and in the region of its expected further growth.
6. Analysing the results obtained by the calculation.

As an example of calculation of reinforced thin-walled structure, a plate model with dimensions of 1x20x144 mm was analysed. The model consists of plates connec-ted by two friction stir welded T joints, [62, 63]. An initial crack with length of a_0 = 3 mm is introduced into the structure between two T welded joints, in the

way not to disturb the symmetry (Fig. 5-7). Within the friction stir welded T joint, four zones are represented:

a) parent zone-PZ or base material-BM,
b) heat affected zone-HAZ,
c) thermo-mechanically affected zone-TMAZ,
d) nugget - N-part of TMAZ.

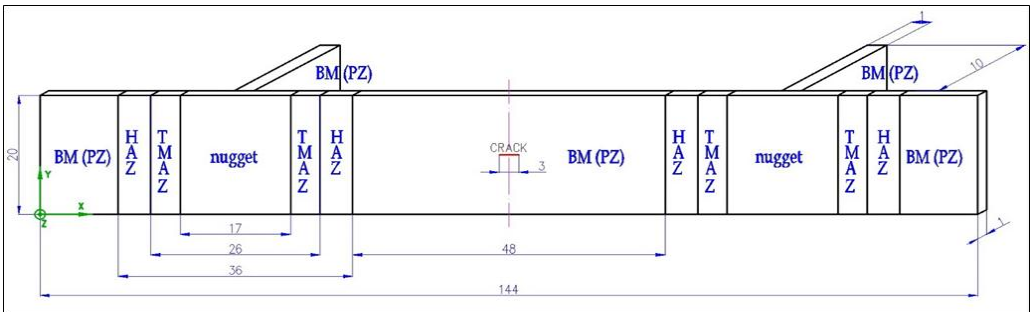

Figure 5—7 Plate with two FSW joints

Modelling of the plate was performed in ABAQUS (Fig. 5-8). The behaviour of a structure with two friction stir welded joints, subjected to tensile fatigue load with maxi-mum value of applied stress σ_{max}=10 MPa and 20 MPa, stress ratio R=0, was analysed.

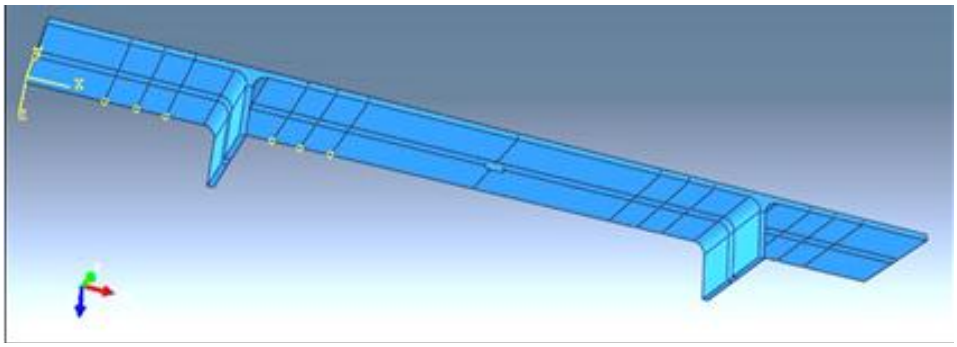

Figure 5—8 The 3D model of a plate with two FSW joints and stiffeners

5.4 Results

Based on the calculation performed in ABAQUS/Morfeo software, the stress intensity factors are obtained for each step of crack propagation and shown in Table 5-4 and Fig. 5-9 for the amplitude loading with σ_{max}=10 MPa, as well as in Table 5-5 and Fig. 5-10 for the amplitude loading with σ_{max}=20 MPa.

Table 5-4 Results for the stress intensity factor, σ_{max}=10 MPa

step 1	73.5	10	44.74066	0.249796	-0.03825	44.77718
step 2	73.99598	10.00557	53.09481	-0.12527	0.004101	53.1852
step 3	74.49237	10.00873	59.32194	0.421639	-0.28715	59.3377
step 4	74.98152	10.01883	66.61981	-0.04595	0.082233	66.80764
step 5	75.46649	10.02822	74.01138	0.534345	0.223502	74.06794
step 6	75.96372	10.04479	80.40281	0.386723	0.247323	80.55934
step 7	76.45908	10.06639	88.25304	0.168236	0.238515	88.474
step 8	76.95379	10.08963	95.92792	0.828494	0.271111	96.07948
step 9	77.44731	10.12151	102.6459	1.637369	-0.06386	102.9315
step 10	77.94328	10.16938	109.6072	-0.39937	-0.22513	109.9776
step 11	78.43517	10.21296	117.4896	2.126424	-0.036278	117.5976
step 12	78.92818	10.27241	125.716	-0.17293	0.399078	126.1686
step 13	79.42214	10.33047	132.6272	2.116308	0.614938	133.3584
step 14	79.91178	10.40296	142.6642	3.119213	0.568641	142.4658
step 15	80.40298	10.48753	149.2978	0.747148	2.261803	150.4325
step 16	80.8958	10.57468	158.2423	3.801537	1.747067	157.5585
step 17	81.38382	10.67961	160.2235	0.627794	-3.769832	162.7062
step 18	81.86188	10.78256	173.7621	6.570444	-7.30424	174.5758
step 19	82.33756	10.89028	178.1682	3.73438	-11.52091	182.6527
step 20	82.81642	11.01197	186.0681	3.042736	-16.2908	191.087
step 21	83.28052	11.13558	182.6384	2.160914	-26.5633	199.1402
step 22	83.724	11.2518	180.3635	-5.48977	-35.8463	201.762
step 23	84.13789	11.33751	171.0435	-10.9944	-49.9356	200.9496
step 24	84.60988	11.27776	166.8216	10.32666	-60.5944	193.1033
step 25	85.0328	11.40625	174.5365	-14.7956	-61.1439	212.2865
step 26	85.51514	11.38652	212.8656	18.54021	-45.0571	224.8229
step 27	85.8897	11.55482	224.5858	-14.202	-60.3045	233.2572
step 28	86.31182	11.61732	253.5383	15.61516	-40.0119	250.432
step 29	86.75583	11.82891	257.0886	-11.0672	-40.9182	260.0929
step 30	87.2564	11.93117	210.1495	5.96441	-57.0319	250.1929
step 31	87.62273	11.96657	187.7985	-11.3692	-94.54545	265.2111
step 32	88.02841	12.06409	158.1191	14.00738	-84.4629	225.8488
step 33	88.44536	12.32484	149.2553	-1.280876	-84.55649	239.3974

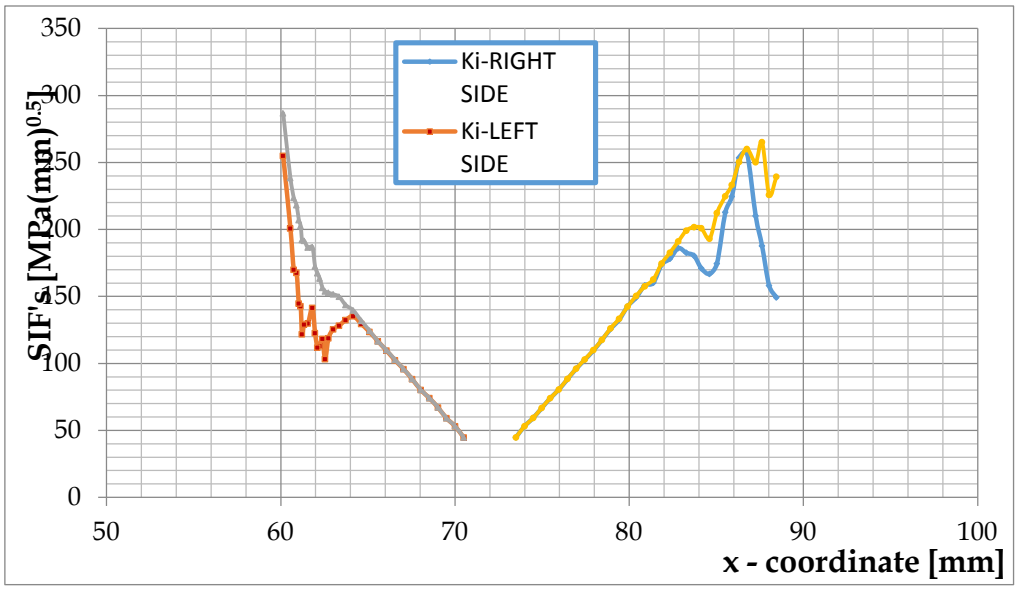

a) SIF

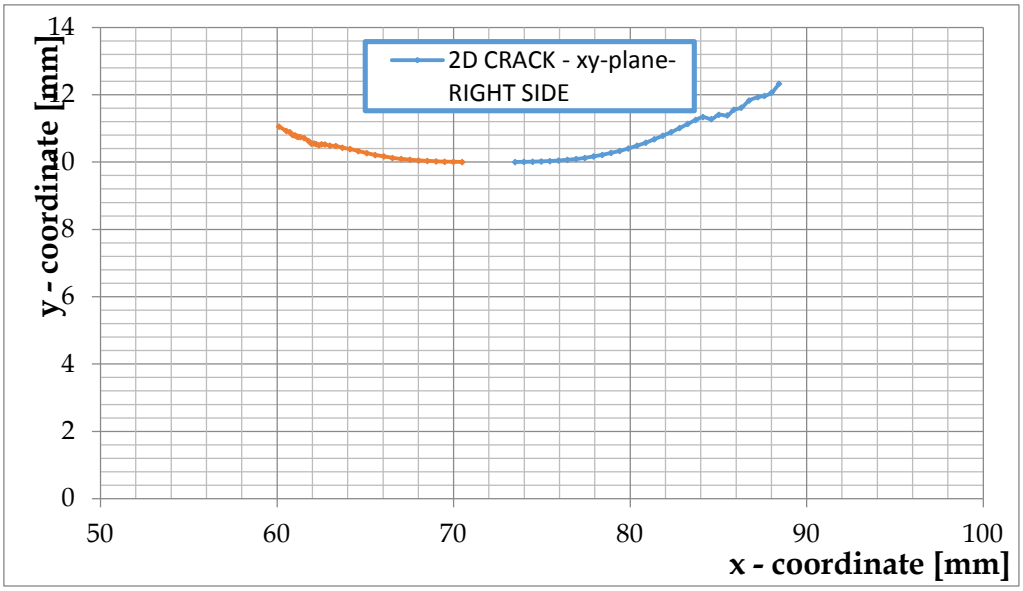

b) xy plane

Figure 5—9 Change of the stress intensity factor with crack growth, σmax=10 MPa

Table 5-5 Results for the stress intensity factor, σ_{max}=20 MPa

step 1	73.5	10	92.1935	0.562254	-0.07807	92.26901
step 3	74.49203	10.00961	123.0566	0.884819	-0.59409	123.0732
step 5	75.46016	10.0293	152.7088	1.396812	0.230092	152.8427
step 7	76.44979	10.0689	180.1188	0.9671	0.518671	180.5908
step 9	77.44031	10.12669	208.5568	3.444636	-0.54838	209.1461
step 11	78.42203	10.22005	237.5223	4.425143	0.821024	237.8891
step 13	79.39942	10.33713	272.1856	4.756197	3.47939	272.9732
step 15	80.37971	10.48937	305.0326	1.808999	8.518187	306.4335
step 17	81.36085	10.66033	327.8418	11.69952	22.38865	336.3664
step 19	82.19608	10.9075	308.4412	-7.30204	91.2949	344.5981
step 21	83.10617	11.07646	327.8628	-7.09106	127.8274	386.1931
step 23	83.98887	11.28869	451.9948	14.31202	38.06138	471.1605
step 25	84.83582	11.6581	449.7386	-19.3019	34.31638	496.4468
step 27	85.70185	11.86529	390.6566	72.86478	-34.5042	473.6136
step 29	86.46742	12.13403	305.592	-48.9512	-219.973	465.1993
step 31	87.2275	12.331	596.7682	-9.12624	-123.509	647.416
step 33	87.92509	12.44096	575.8809	48.399	-79.6617	659.9891
step 35	88.77516	12.78428	626.7779	-66.2465	-52.9749	715.9955
step 37	89.48838	12.98834	681.2229	-40.9825	-21.0667	716.9998
step 39	90.34291	13.3548	810.1723	-21.4108	-10.953	857.2148
step 41	91.44496	13.73945	812.5606	39.28242	20.06795	970.7244
step 43	92.51488	13.69447	794.2246	28.94655	-1.19815	965.9387
step 45	92.90292	13.85582	675.8754	-13.6808	84.22295	867.304
step 47	93.17775	14.41324	528.0636	67.59256	154.133	771.3716
step 49	93.74551	14.91624	930.8125	9.82215	355.636	1114.126
step 51	94.57059	15.45589	1282.788	-255.285	103.0798	1326.704
step 52	95.07039	15.63358	1427.987	48.26699	84.43383	1566.56

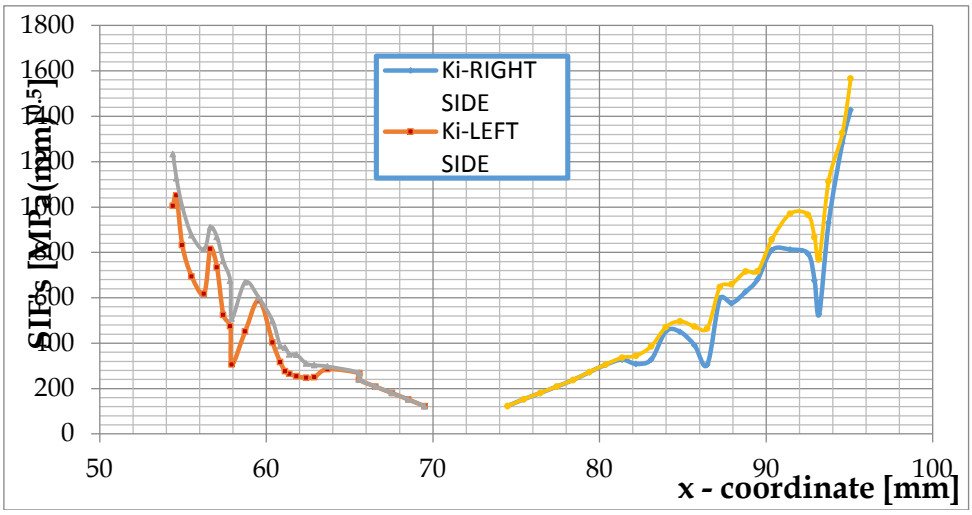

a) SIF

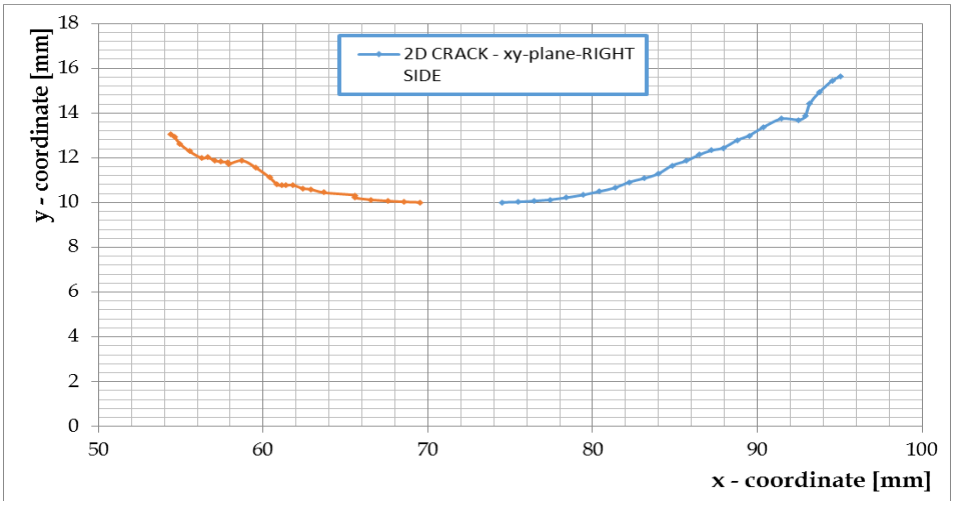

b) xy plane

Figure 5—10 Change of the stress intensity factor with crack growth, σ_{max}=20 MPa

The crack propagation data, given as the function of number of load cycles, is shown in Table 5-6 and Fig. 5-10 for the amplitude loading with σ_{max}=10 MPa, as well as in Table 5-7 and Fig. 5-11 for the amplitude loading with σ_{max}=20 MPa. Number of cycles is determined by the numerical integration of Paris law, as defined in MORFEO.

Table 5-6 Number of cycles, N, and crack elongation at given steps

1	0	0
2	53396	53396
3	34636	88033
4	24663	112696
5	17982	130678
6	13783	144461
7	10682	155144
8	8240.5	163384
9	6620.5	170005
10	5452.3	175457
11	4473.1	179930
12	3678.5	183609
13	3082.4	186691
14	2565.4	189256
15	2159.1	191416
16	1861.2	193277
17	1658.2	194935
18	1435.6	196371
19	1221	197592
20	1102.7	198694
21	1022.4	199717
22	987.12	200704
23	967.25	201671
24	1010.6	202682
25	963.07	203645
26	707.84	204353
27	472.14	204825
28	406.66	205231
29	382.48	205614
30	409.37	206023
31	434.37	206458
32	508.66	206966
33	481.78	207448

Table 5-7 Number of cycles, N, and crack elongation at given steps

1	0	0
3	4191	10720
5	2162	15839
7	1323	18845
9	834	20713
11	565	21972
13	388	22824
15	279	23431
17	207	23873
19	163	24198
21	149	24537
23	88.4	24740
25	60.8	24863
27	89.7	25038
29	76.1	25187
31	27.6	25270
33	26.1	25320
35	24	25372
37	20.8	25414
39	13.4	25444
41	11.6	25468
43	2.58	25477
45	12.5	25497
47	17.6	25534
49	7.31	25551
51	3.02	25559
52	2.7	25561

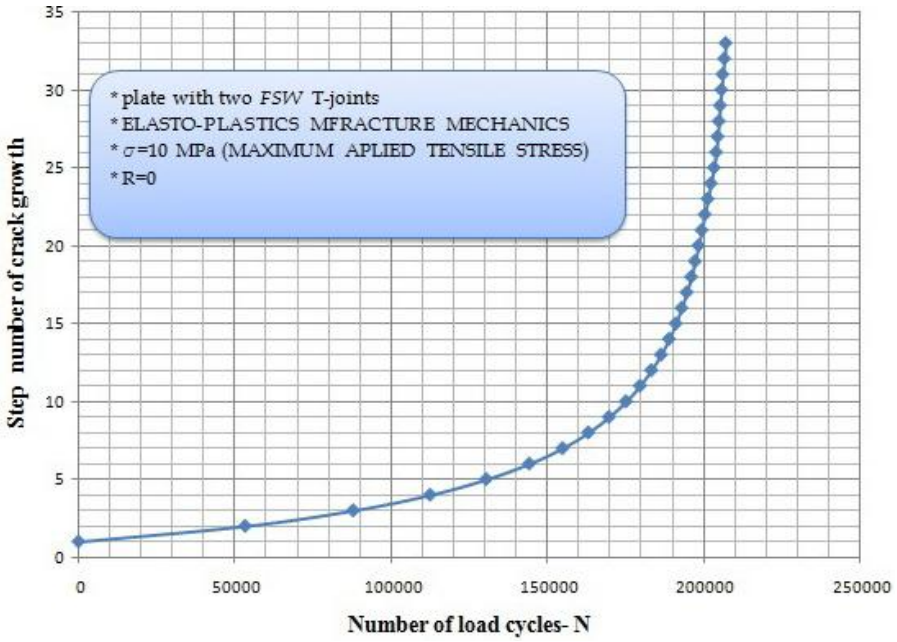

Figure 5—11 Crack propagation as a function of number of load cycles, 10 MPa

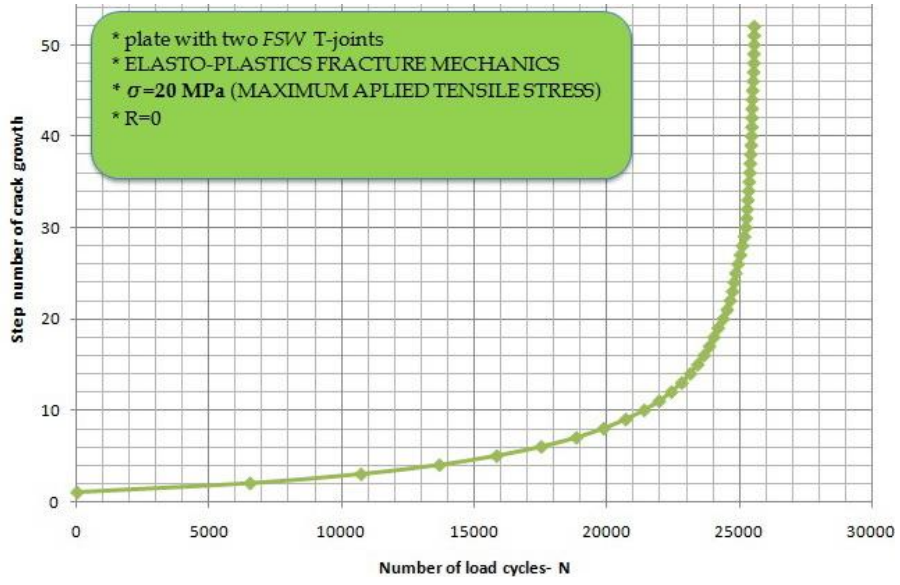

Figure 5—12 Crack propagation as a function of number of load cycles, 20 MPa

Finally, von Mises stress distribution is shown for different crack propagation steps in Fig. 5-12 for 10 MPa and in Fig. 5-13 for 20 MPa, with the appropriate scale factor, so that the crack opening becomes clearly visible.

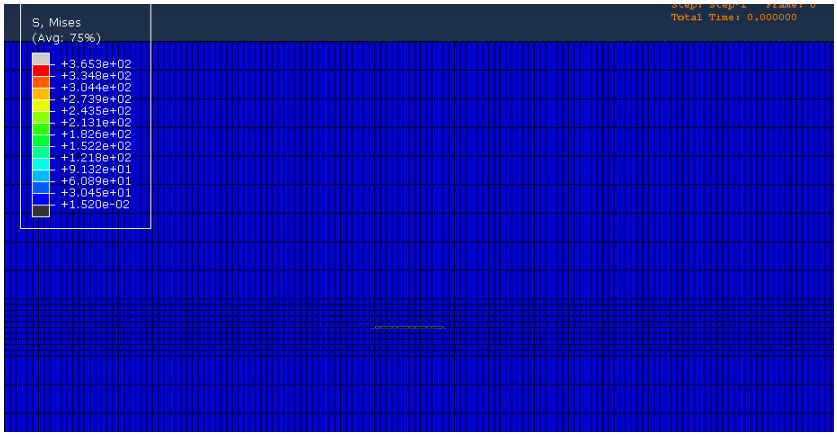

a) 4 steps

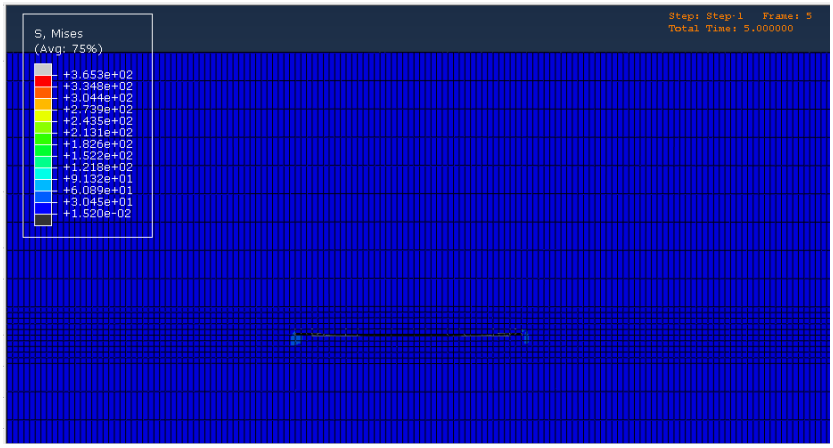

b) 9 steps

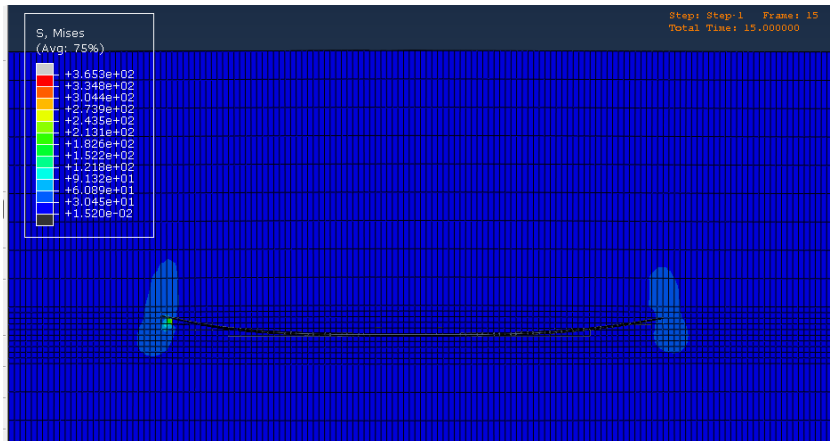

c) 15 steps

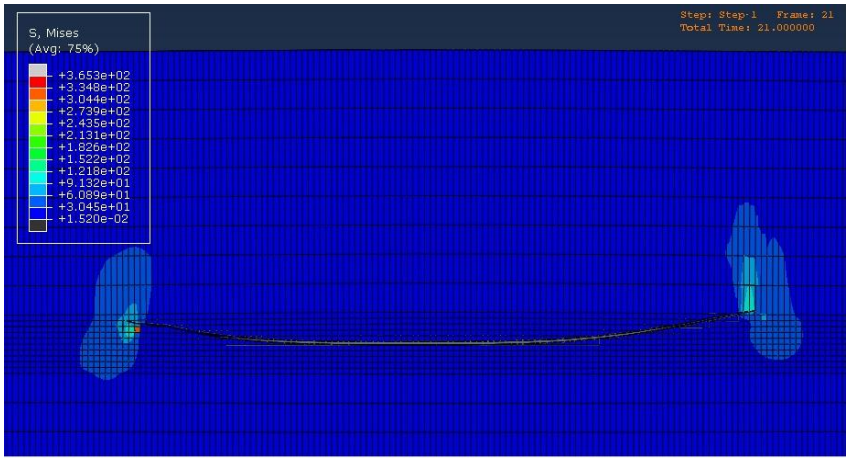

d) 20 steps

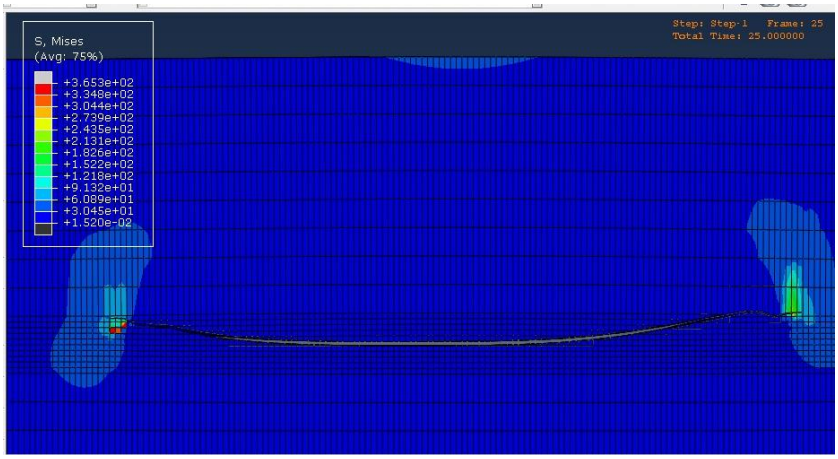

e) 25 steps

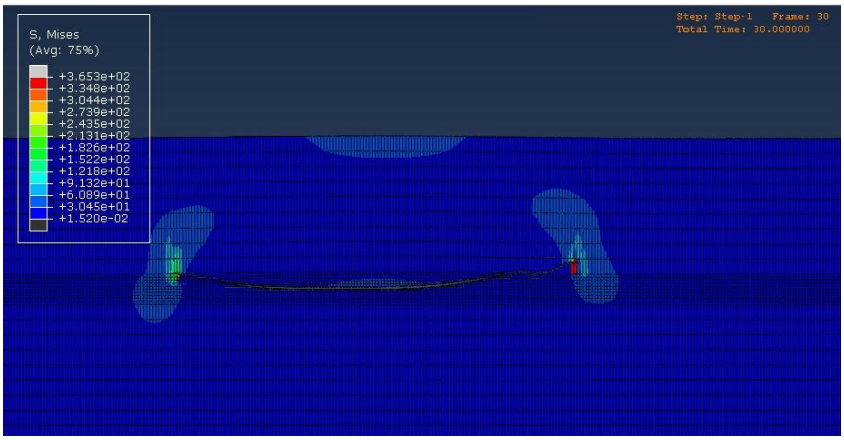

f) 30 steps

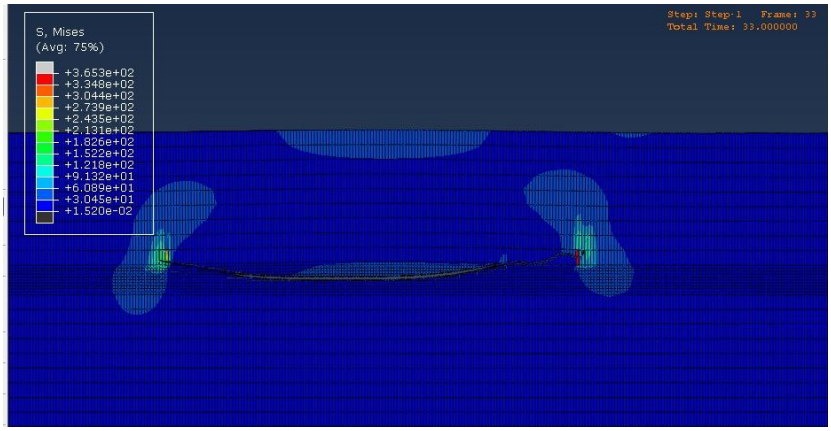

g) 33 steps

Figure 5—13 Distribution of von Mises stress for different crack growth steps Δσ=10 MPa

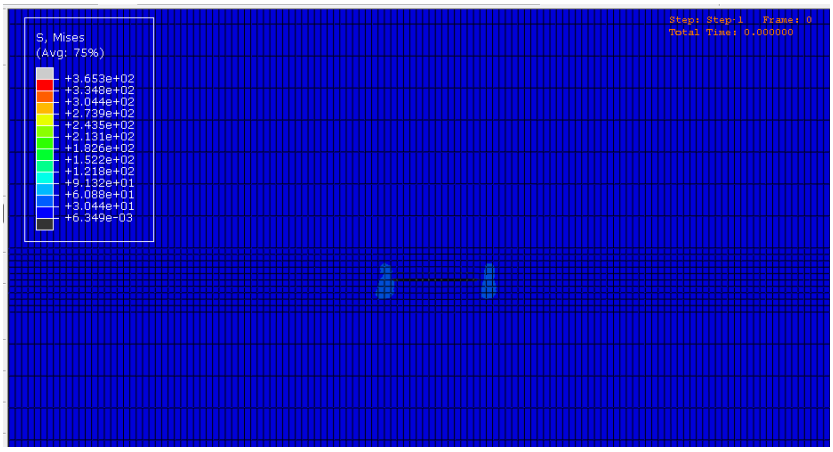

a) 0 steps

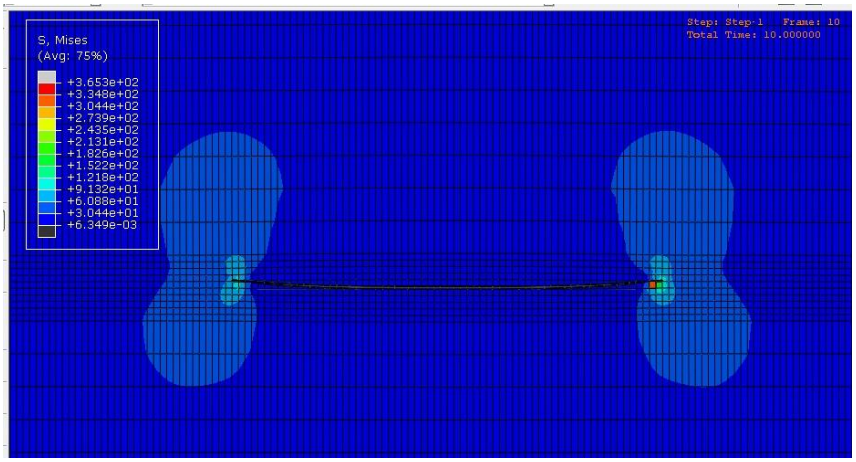

b) 10 steps

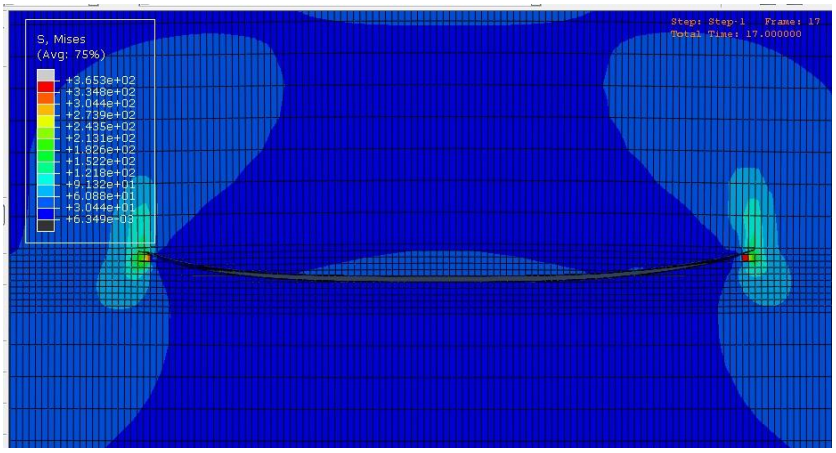

c) 17 steps

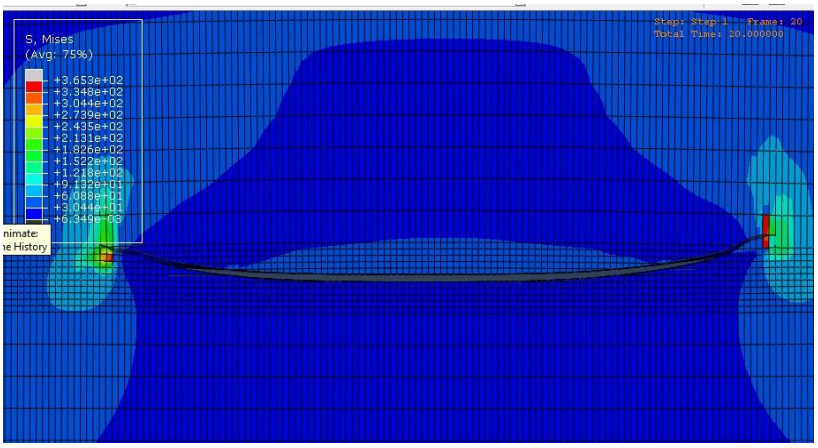

d) 20 steps

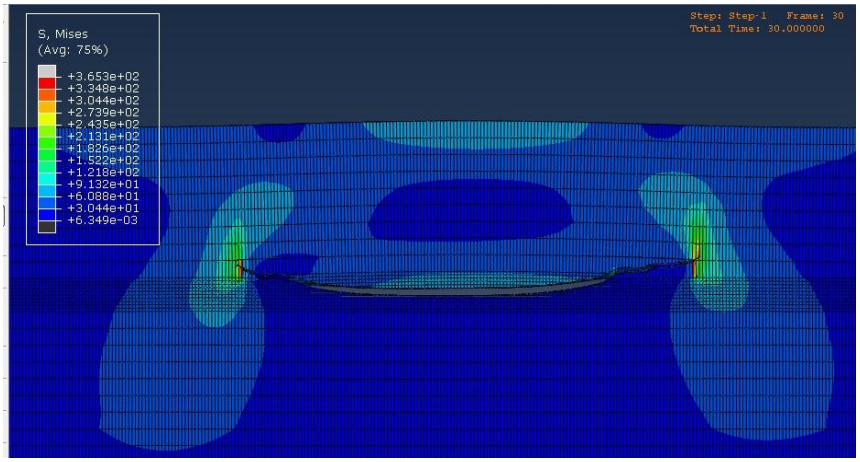

e) 30 steps

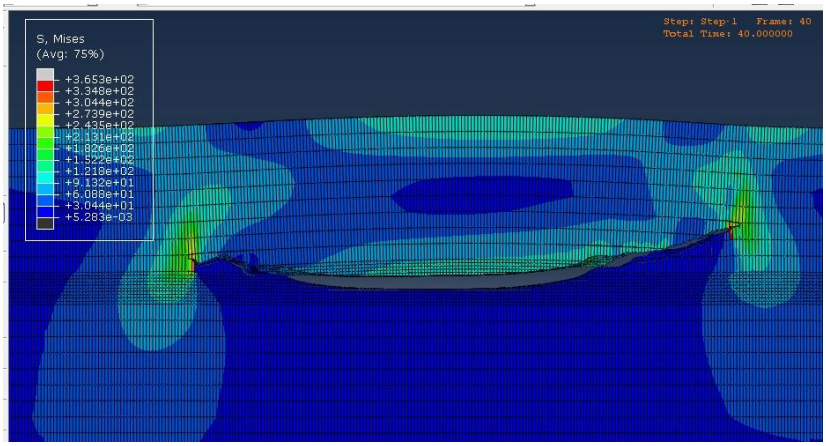

f) 40 steps

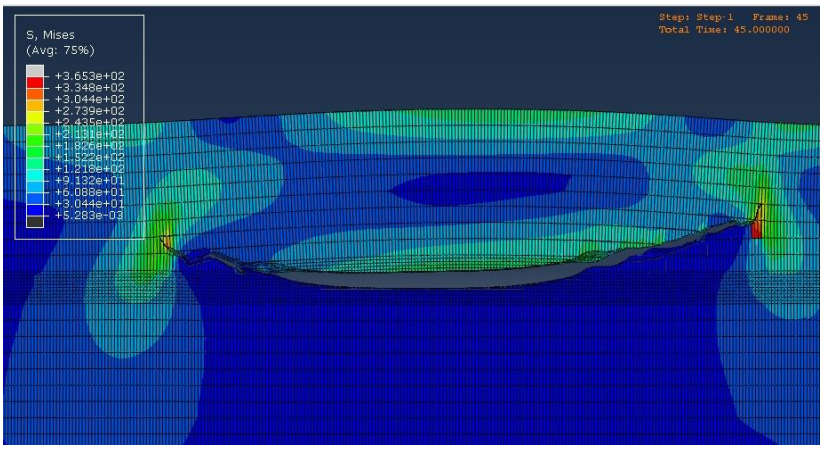

g) 45 steps

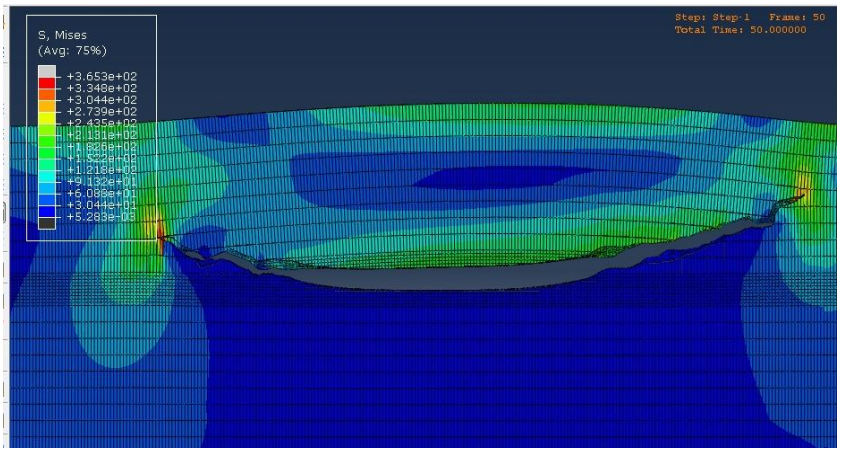

h) 50 steps

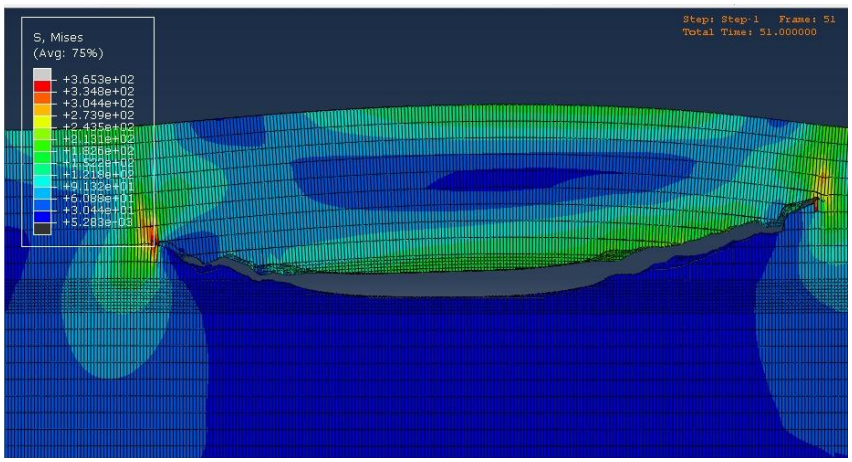

i) 51 steps

Figure 5—14 Distribution of von Mises stress for different crack growth steps Δσ=20 MPa

5.5 Concluding remarks

As one can see from the data given in this Chapter, the crack propagates only within the parent material, and does not reach the remaining zones of the two friction stir welded T joints.

Following a certain number of steps, i.e. the period of the stable crack propagation, the faster, unstable crack propagation occurs, leading to failure. In the case considered here, faster crack propagation occurred after a number of load cycles of ≈ 200,000 for stress amplitude 10 MPa, and 25,000 for stress amplitude 20 MPa (these numbers are defined by the change of the curve slope). Anyhow, the structure maintains its integrity, since the stress intensity factor is still smaller than the fracture toughness. This enables safe use of such a structural component until the number of load cycles in service reaches the value predicted as described, when its replacement should be considered.

During the propagation of the crack through the structure, change of its direction can be noticed. This phenomenon is related to shear stresses appearing in the structure, and the two additional fracture modes are quantified by corresponding stress intensity factors KII and KIII, although it is not complete clear if this is only due to real 3D effect or there were some unreal numerical effects, as well.

The 3D effects are clearly visible also from the data given in this Chapter (different values of crack elongation from the left and the right side). This effect is more pronounced for KI than for Keff.

By analysing the problems of crack propagation in a plate with stiffeners, i.e. two friction stir welded T joints, the following conclusions have been reached:

- Numerical simulation, as presented here, can be used to assess the right time to withdraw the component from exploitation, since it provides data for the stress intensity factors, von Mises stress distribution and number of cycles for each crack propagation step, enabling prediction of the number of cycles needed for stable to unstable crack propagation.

• During its propagation, the crack remained within the base metal in the analysed case, leaving more detailed analysis for future work, including crack propagation through different welded joint zones and the effect of stiffeners.

• During the propagation of the crack through the structure, change of its direction can be noticed. This phenomenon is related to shear stresses appearing in the structure, requiring further analysis of 3D effects, but possible unrealistic behaviour due to numerical effects should also be investigated.

In further research, it is necessary to devote particular attention to the following:

• Modelling of different properties of materials, i.e. different welded joint zones, and their use as input data.

• Accurate defining of a real load spectrum during the exploitation period.

• The 3D vs. numerical effects.

• Experimental verification of numerical simulation.

6 CONCLUDING REMARKS

6.1 Conclusions of PhD study

Chapter 1 - Introduction

The objective of thesis is defined, being the Friction Stir Welding of 5083 Al alloy, and its cracking behaviour, including resistance to crack growth. On the engineering level, the thesis is directed toward optimum welding parameters (rotational speed, welding speed and tilt angle of the tool), as well as design of tool and clamping system. On the scientific level, thesis is focused on welded joint behavior and more particularly, on its crack resistance. Finally, the FEM will be used to model welding process, i.e. to determine temperature fields, and to estimate fatigue crack growth rate, i.e. number of cycles to reach unstable crack growth.

Chapter 2

Since Year 2000, the researches for friction stir welding process were included in scientifical program of ISIM Timisoara. Applying the innovative FSW-TIG hybrid welding, relative to classical FSW enabled higher productivity through increase of welding speed and reduction of forces during FSW process, significantly reducing wear of welding tools at the same time.

Two innovative methods for monitoring in real time of the welding process were developed. These evidenced that there are the real possibilities, qualitative and quantitative for detection of defects from FSW welded joints through infrared thermography. Also, good results can be achieved by monitoring of functioning behaviour for engine that assure rotation speed of welding tool, obtaining of information about current consumption in the main sequences of FSW process: start rotation - contact between pin tool and welding materials - contact between tool shoulder and welding materials - effective welding process - completion of process and remove of welding tool from welded joint.

Friction Stir Welding of T joints has also been successfully performed, as the latest contribution, in cooperation with GOSA, Smederevska Palanka, Serbia. Sound welded joint, with full penetration, have been obtained and tested, providing good results and indicating strong potential for further developments.

Chapter 3

In the scope of the experimental investigation, hot rolled plates, 6 mm thick, cut into a 500 x 100 mm sections have been welded. The experimental plan was as follows: rotational speed (ω) was in a range 500-700 rpm, welding speed 75-125 mm/sec and, advancing tilt angle of the tool 1-3 deg. The tool is designed as a 25 mm shoulder diameter with 6 mm high pin. This design is already proofed in previous FSW experiments and also checked numerically to compare the effect of shoulder shape (conical vs. flat) on temperature field. It was shown that the temperature field is more favourable with conical design.

Taguchi Design of Experiment method has been applied to reduce number of experiments, so that 9 instead of 81 trials have been chosen in accordance with orthogonal array rule.

Charpy testing was conducted on a high-speed data acquisition instrument, using instrumented pendulum to separate energies for crack initiation and propagation. Two specimens were used, providing results close enough, so that the average value was used as the relevant one, without noise analysis. This has simplified application of DoE method, since it was possible to make it without calculating (S/N) ratio.

Average values of the total impact energy, as obtained for the 9 experiments, chosen according to the orthogonal matrix, indicated that the travel (welding) speed has the biggest effect (56%), followed by significant effect of the rotational speed (43%), whereas the tool angle has very small effect (1%).

Different effects are obtained when separated energies are considered. In the case of the initiation energy, the rotational speed is the most influential (42%), closely followed by the tool angle (39%), whereas the effect of the welding speed if smaller (19%), but not negligible. In the case of the propagation energy, the rotational speed is still the most influential, even more pronounced (63%), whereas both the tool angle and welding speed effects are significantly lower (21% and 16%, respectively). The effects of tool angle on the individual energies cancel each other, so the effect on the total energy is negligible.

Another crack resistant property, fracture toughness, has shown similar behaviour, as in the case of the propagation energy, which was reasonable to expect, since in both cases it is crack dominated behaviour, whereas the influence of loading type is obviously small (also reasonable for material which is not exactly brittle). Anyhow, one should notice more pronounced effects, since the rotational speed was rated at 88%, whereas the welding speed and tool angle were rated only at 4% and 8%, respectively. One can conclude that the rotational speed has almost exclusive effect for crack resistance under static loading, keeping its dominance in the case of crack resistnace under impact loading, but at the smaller scale.

Microstructural examination revealed all typical characteristics of FSW fracture surface, like onion rings, dimples, shear and cleavage marks, micropores and microvoids, specific grain shape and size. Also, characteristic appearance of different zones were identified (WM-NZ, TMHAZ, HAZ, PM). From the microstructural point of view, the effect of input parameters on crack resistance is not of any significance (min. and max. toughness is 15.05 to 23.75 J, and fracture toughness is even in the smaller range, 55 to 75 MPa$\sqrt{m}$, both indicating mixed mode of fracture with some characteristics of ductile behaviour.

Fatigue crack growth revealed surprisingly small differences meaning that crack resistance fatigue loading is not sensitive to different microstructure…Contrary to other crack resistance testing, where crack was positioned in the WM-NZ, as the most critical region, for different welding conditions, in this case the same welding conditions were chosen (trial 1) to evaluate the effect of microstructure. Anyhow, not only was this effect small, but it also turned out that the resistance to crack growth in the BM is sufficient for the example used in this thesis, since the crack growth was limited to BM only.

Digital Image Correlation technique has been applied as the most suitable for local measurements in order to obtain true stress – true strain curves, needed as an input in the numerical simulation. Characteristic local points in all four regions of welded joint (WM, TMAZ, HAZ, BM) have been used to obtain local true stress – true strain data.

Chapter 4

Detailed mathematical model of FSW has been developed taking into account as many variables as possible, in order to simulate welding process and obtain temperature fields. Based upon results and discussion one can make conclude that the finite element method is capable of simulating the plunge phase of FSW, if applied correctly, as shown here, and also verified by experiments, as shown elsewhere. The same applies to the linear phase of FSW, as a simpler one, which has not been analysed here, but also verified elsewhere, using the same approach as presented here. Therefore, the finite element method can used to replace expensive experiments, once the model is verified.

Another important conclusions are, that the temperature in the matrix is lower than the melting temperature, that the concavity is designed to provide a reservoir of material above the original crown surface of the weld, facilitate transport of material around the tool and reduce plate thinning in the weld zone, and that the "flash" can be minimized, but not eliminated, by a proper choice of welding parameters and tool design - using tool with a conical shoulder.

The maximum temperatures of the plunge stage in friction stir welding are higher by using tool with a flat shoulder than by using tool with a conical shoulder for the same rotation speed. Therefore, the conical shoulder is more suitable for most of the practical use, since it enables smaller temperature gradients and more favourable stress-strain state.

Chapter 5

Numerical simulation of fatigue crack growth was made to estimate number of cycles before unstable crack growth, under two different stress amplitude. Although no experimental results were available for the comparison, the main aim was achieved, i.e. to evaluate the effect of stress amplitude (loading) on the number of cycles before unstable crack growth. Anyhow, some other results for experimental and numerical investigation indicated reasonable agreement, even with complicated crack growth path.

As one can see from the data given in this Chapter, the crack propagates only within the parent material, and does not reach the remaining zones of the two friction stir welded T joints.

Following a certain number of steps, i.e. the period of the stable crack propagation, the faster, unstable crack propagation occurs, leading to failure. In the case considered here, faster crack propagation occurred after a number of load cycles of ≈ 200,000 for stress amplitude 10 MPa, and 25,000 for stress amplitude 20 MPa (these numbers are defined by the change of the curve slope). Anyhow, the structure maintains its integrity, since the stress intensity factor is still smaller than the fracture toughness. This enables safe use of such a structural component until the number of load cycles in service reaches the value predicted as described, when its replacement should be considered.

During the propagation of the crack through the structure, change of its direction can be noticed. This phenomenon is related to shear stresses appearing in the structure, and the two additional fracture modes are quantified by corresponding stress intensity factors K_{II} and K_{III}, although it is not complete clear if this is only due to real 3D effect or there were some unreal numerical effects, as well.

The 3D effects are clearly visible also from the data given in this Chapter (different values of crack elongation from the left and the right side). This effect is more pronounced for K_I than for K_{eff}.

By analysing the problems of crack propagation in a plate with stiffeners, i.e. two friction stir welded T joints, the following conclusions have been reached:

• Numerical simulation, as presented here, can be used to assess the right time to withdraw the component from exploitation, since it provides data for the stress intensity factors, von Mises stress distribution and number of cycles for each crack propagation step, enabling prediction of the number of cycles needed for stable to unstable crack propagation.

• During its propagation, the crack remained within the base metal in the analysed case, leaving more detailed analysis for future work, including crack propagation through different welded joint zones and the effect of stiffeners.

• During the propagation of the crack through the structure, change of its direction can be noticed. This phenomenon is related to shear stresses appearing in the structure, requiring further analysis of 3D effects, but possible unrealistic behaviour due to numerical effects should also be investigated.

In further research, it is necessary to devote particular attention to the following:

• Modelling of different properties of materials, i.e. different welded joint zones, and their use as input data.

• Accurate defining of a real load spectrum during the exploitation period.

• The 3D vs. numerical effects.

• Experimental verification of numerical simulation.

6.2 Contribution of the author

Contribution of the author is mostly pronounced in the following:

- Development of FSW technology for Al 5083 alloy, both for butt and T joints. Toward this aim the author has contributed in choosing the optimal welding parameters to avoid defects, as well as in design of supporting plates and clamping devices.

- Experimental investigation of crack resistance, both under impact loading (Charpy toughness) and under static loading (fracture toughness). Innovative technique for separating the energies for crack initiation and propagation, using change of slope of force in diagramme force-time, as recorded on the instru-mented Charpy pendulum.

- Design of Experiments, according to Taguchi's method, applied to 3x3 scheme, with 9 trails chosen to replace 81 trials needed for the „full-scale" experiment. This was applied for toughness and fracture toughness testing, enabling precise evaluation of effects of 3 input parameters (rotational speed, welding speed and tool angle) on crack resistance.

- Evaluation of number of cycles to achieve unstable crack growth, by applying the innovative numerical procedure, based on stress-strain analysis and fatigue crack propagation according to Paris law.

6.3 Dissemination of results

The main results are published in scientific papers and conferences, as follows:

1. A. Živković, A. Đurđević, A. Sedmak, H. Dascau, I. Radisavljević, Đ. Đurđević, Friction Stir Welding of T-joints, accepted for the Int. Conf. SEE IIW, Timisoara, 2015

2. Sedmak Aleksandar S, Eramah Abdsalam M, Tadic Srdjan S, Perkovic Srdja, Dascau Horia, Impact Toughness of Friction Stir Welded Al-Mg Alloy, MATERIALS TESTING 2014 56 (10):837-841

3. Veljić, D., Perović, M., Sedmak, A., Rakin, M., Bajić, N., Medjo, B., Dascau, H., Numerical Simulation of the Plunge Stage in Friction Stir Welding, Structural integrity and life, 11 (2011), 2, pp. 131-134

4. Veljic, D., Perovic, M., Medjo, B., Rakin, M., Sedmak, A., Dascau, H., Thermo-mechanical modeling of Friction Stir Welding. The 4th International Conference, Innovative technologies for joining advanced materials, Timisoara, 2010, p 171-176.

5. Danijela Živojinović, Horia Dascau, Aleksandar Sedmak, Aleksandar Grbović, Integrity assessment of a structure made of two FSW T-welds, Proc. 6th International Scientific and Expert Conference TEAM 2014,

   Technique, Education, Agriculture & Management, Kecskemét, November 10-11, 2014, p. 456-459.

6. A.Djurdjevic, D.Zivojinovic, A.Grbovic, A. Sedmak, M.Rakin, H.Dascau, S.Kirin, Numerical simulation of fatigue crack propagation in friction stir welded joint made of Al 2024 T351 alloy, submitted to Engineering Failure Analysis

7. H.Dascau, D.Zivojinovic, A.Sedmak, V.Grabulov, Fatigue crack growth in friction stir welded AA 5083 joint by using the finite element method, Structural Integrity and Life, 2015, Vol. 15, No. 1, p. 33.

6.4 Acknowledgements

The author wishes to acknowledge the contributions of the laboratories in Military-Technical Institute in Zarkovo (Mechanical testings), Serbia, as well in .the Institute Vinca, Belgrade, Serbia (metallography).

7 BIBLIOGRAFIE

1. W. M. Thomas et al, Friction stir butt welding, International Patent Application, PCT/GB92/02203, December 1991
2. C. J. Dawes, W. H. Thomas: Friction stir process welds aluminum alloys. The process produces low-distortion, high-quality, low-cost welds on aluminum, Weld. J. 75 (1996), pp. 41-45.
3. J. D. Cost, J. A. M. Ferrira and L.P. Borrego; "Fatigue Behaviour of AA6082-T6 Alumnium Alloy Friction Stir Welds Under Amplitude Loading", CEMUC, University of Coimbra, Portugal.
4. H. Larsson, L. Karlsson, L-E. Svensson, ESAB AB, Gotehorg and V. T. Utreckling; "Friction Stir Welding of AA5083 and AA6082 Aluminium", Svestsaren No 2, 2000.
5. http://www.esab.de/de/de/support/upload/FSW-Technical-Handbook.pdf
6. T. Lorentzen; http://www.bayards.nl/Meriad-CMS-New/store/files/1265221220_Bayards Friction Stir Welding presentation.pdf
7. www.Sapagroup.com/us/profiles.
8. A. M. M. Eramah: Friction stir welding parameters influencing the fracture resistance of an Al5083 alloy welded joint, Doctoral thesis, University of Belgrade, 2014.
9. M. M. Attallah; "Microstructure- Property Development in Friction Stir Welds of Aluminum Based Alloys", University of Birmingham Research Archive, Unit Kingdom, September, 2007.
10. P. Threadgill, A. Leonard, H. Shercliff and P. Withers; International Materials Reviews, vol.54. no.2, March 2009, PP. 49-93 ,.
11. R. S. Mishra, Z.Y. Ma; Materials Science and Engineering, Report 50, 2005 ,PP. 1–78.
12. M. Kutz; "Handbook of Mechanical Engineeing, John Wiley & Sons, Inc John Wiley & Sons, Inc., Second Edition, Washington, D.C, 1998.
13. R. Johnson; "Force in Friction Stir Welding of Aluminium Alloys", TWI Members Report, Vol. 716, 2000, pp. 1-18.
14. Fuller, C.B. – Friction Stir Tooling: Tool Materials and Designs, Friction Stir Welding and Processing, ASM International, 2007
15. Arbegast, W. J. - Friction Stir Welding: After a Decade of Development, Friction Stir Welding and Processing IV, TMS Publications, 2007
16. Fleming, P.A. -Monitoring and control in friction stir welding, Dissertation Thesis, Vanderbilt University, Nashville, Tennessee, May, 2009
17. Boldsaikhan, E. , A.M. Logar, A.M. , Corwin, E.M. - Real-Time Quality Monitoring in Friction Stir Welding: The Use of Feedback Forces for

Nondestructive Evaluation of Friction Stir Welding, Lambert Academic Publishing, ISBN-10: 383835298X , ISBN-13: 978-3838352985, June 2010
18. Murariu, A., Bîrdeanu, V., Cojocaru, R., Safta, V., Dehelean, D., Boţilă, L.,Ciucă, C – Application of Thermography in Materials Science and Engineering, Chapter in the book "Infrared Thermography", pp. 27-52, http://www.intechopen.com/books/infrared-thermography, ISBN: 978-953-51-0242-7, Publisher InTech, March, 2012.
19. Safta, V. - Application of infrared thermography in the non-destructive examination of friction stir welds, Welding & Material Testing BID ISIM, No.1/2010, pp.29-40, ISSN 1453-0392
20. Dehelean, D., Cojocaru, R., Radu, R., Safta, V. - Monitoring the friction stir welding process of aluminum and magnesium alloys, International Conference Welding And Related Technologies Into The Third Millennium, 24–26 November, 2008 Kyiv, Ukraine
21. A. Živković, A. Đurđević, A. Sedmak, H. Dascau, I. Radisavljević, Đ. Đurđević Friction Stir Welding of T-joints, accepted for the Int. Conf. SEE IIW, Timisoara, 2015
22. Buffa G., ratini L., Micari F., Shivpur, R., "Material Flow in FSW of T-joints: Experimental and Numerical Analysis", Springer, No.1, pp. 1283-1286, 2008.
23. Fratin, L., Buffa G., Filice L., Gagliardi F., "Friction stir welding ofAA6082-T6 T-joints: process engineering and performance measurement", Proc. IMechE, Vol. 220, pp. 669-676, 2005.
24. ASTM E399-89, Standard Test Method for Plane-Strain Fracture Toughness of Metallic Materials, Annual Book of ASTM Standards, Vol. 03.01. p. 522. 1986.
25. ASTM E813-89, Standard Test Method for J_{Ic}, A Measure of Fracture Toughness, Annual Book of ASTM Standards, Vol. 03.01. p. 651, 1993.
26. P M V Subbarao, Design Of Experiments, Professor, Indian Institute Of Technology Delhi, Mechanical Engineering Department.
27. Optimization Of Welding Parameters For Maximization Of Weld Bead Widths For Submerged Arc Welding Of Mild Steel Plates. International Journal Of Engineering &Technology (Ijert) Issn: 2278-0181 Vol.1 Issue 4, June-(2012).
28. Sedmak Aleksandar S, Eramah Abdsalam M, Tadic Srdjan S, Perkovic Srdja, Dascau Horia, Impact Toughness of Friction Stir Welded Al-Mg Alloy, MATERIALS TESTING 2014 56 (10): 837-841
29. A. M. M. Eramah, S. Tadić, A. Sedmak: Impact fracture response of friction stir welded Al-Mg alloy, Structural Integrity and Life 13 (2013), pp. 171-177.
30. A. M. M. Eramah, D.Sc. thesis, Influence Parameters of Friction Stir Welding on Fracture Resistance Al 5083 Alloy, University of Belgrade, 2014
31. J. Schneider, R. Beshears, A. C. Nunes Jr.: Interfacial sticking and slipping in the friction stir welding process, Mater. Sci. Eng. A 435 (2006), pp. 297-304.

32. D. P. P. Booth, M. J. Starink, I. Sinclair: Analysis of local microstructure and hardness of 13 mm gauge 2024-T351 AA friction stir welds. Mater. Sci. Technol. 23 (2007), pp. 276-284.
33. G. M. Xie, Z. Y. Ma, L. Geng: Development of a fine-grained microstructure and the properties of a nugget zone in friction stir welded pure copper, Scripta Mater. 57 (2007), pp. 73-76.
34. L. Ke, L. Xing, J. E. Indacochea: Material flow patterns and cavity model in friction-stir welding of aluminum alloys, Metall. Mater. Trans. B 35 (2004), pp. 153
35. Milos Milosevic, Nenad Mitrovic, Radomir Jovicic, Aleksandar Sedmak, Tasko Maneski, Aleksandar Petrovic, Tarek Aburuga, Measurement of local tensile properties of welded joint using Digital Image Correlation method, Chemicke Listy 106 (2012), pp. 485-488.
36. Veljić, D., Perović, M., Sedmak, A., Rakin, M., Bajić, N., Medjo, B., Dascau, H., Numerical Simulation of the Plunge Stage in Friction Stir Welding, Structural integrity and life, 11 (2011), 2, pp. 131-134
37. Zhang, H. W., Zhang, Z., Chen, J. T.,The Finite Element Simulation of the Friction Stir Welding Process, Materials Science and Engineering A, 403 (2005), 1-2, pp. 340-348
38. Zhang, H. W., Zhang, Z., Numerical Modeling of Friction Stir Welding Process by using Rate-dependent Constitutive Model, Journal of Materials Science & Technology, 23 (2007), 1, pp. 73-80
39. Xu, S., Deng, X., Reynolds, A. P., Seidel, T. U., Finite Element Simulation of Material Flow in Friction Stir Welding, Science and Technology of Welding and Joining, 6 (2001), 3, pp. 191-193
40. Veljic Darko M, Sedmak Aleksandar S, Rakin Marko P, Bajic Nikola S, Medjo Bojan I, Bajic Darko R, Grabulov Vencislav K, Experimental and Numerical Thermo - Mechanical Analysis of Friction Stir Welding of High - Strength Alluminium Alloy, Suppl. THERMAL SCIENCE 2015, 18, S29-S38
41. Song, M., Kovačević, R., Numerical and Experimental Study of the Heat Transfer Process in Friction Stir Welding, Journal of Engineering Manufacture, 217 (2003), 1, pp. 73-85
42. Chen, C. M., Kovačević, R., Finite Element Modeling of Friction Stir Welding – Thermal and Thermomechanical Analysis, International Journal of Machine Tools & Manufacture, 43 (2003), 13, pp. 1319-1326
43. Chen, M. C., Kovačević, R., Joining of Al 6061 Alloy to AISI 1018 Steel by Combined Effects of Fusion and Solid State Welding, International Journal of machine Tools and Manufacture, 44 (2004), 11, pp. 1205-1214
44. Dong, P., Lu, F., Hong, J. K., Cao, Z., Coupled Thermomechanical Analysis of Friction Stir Welding Process using Simplified Models, Science and Technology of Welding and Joining, 6 (2001), 5, pp. 281-287
45. Soundararajan, V., Zeković, S., Kovačević, R., Thermo-Mechanical Model with Adaptive Boundary Conditions for Friction Stir Welding of Al 6061,

International Journal of Machine Tools & Manufacture, 45 (2005), 14, pp. 1577-1587
46. Kim, D., Badarinarayan, H., Kim, J. H., Kim, C., Okamoto, K., Wagoner, R. H., Chung, K., Numerical Simulation of Friction Stir Butt Welding Process for AA5083-H18 Sheets, European Journal of Mechanics A/Solids, 29 (2010), 2, pp. 204-215
47. Veljic, D., Perovic, M., Medjo, B., Rakin, M., Sedmak, A., Dascau, H., Thermo-mechanical modeling of Friction Stir Welding. The 4th International Conference, Innovative technologies for joining advanced materials, Timisoara, 2010, p 171-176.
48. Zhang, H., Zhang, Z., Chen, J. (2007). 3D modeling of material flow in friction stir welding under different process parameters. Journal of Materials Processing Technology 183 (2007) p. 62–70.
49. M. W. Mahoney, R. Mishra, T. Nelson, ''High Strain Rate Superplasticity in Thick Section 7050 Aluminium Created by Friction Stir Processing'' in Proceedings of the Third International Symposium on Friction Stir Welding, Kobe Exhibition Center, Port Island, Kobe, Japan, September 2001
50. Rajiv S. Mishra, Murray W. Mahoney, Friction stir welding and processing, http://books.google.com
51. Schmidt H, Hattel J, "A local model for the thermomechanical conditions in friction stir welding". Model Simul Mater Sci Eng 13: 77–93, 2005.
52. Abaqus Inc., Analysis – User's Manual v.6.7, 2007
53. Belytschko T., Black T.: Elastic crack growth in finite elements with minimal remeshing. Int. J. for Num. Meth. in Engng. 45(5), 601-620 (1999).
54. Moes N., Dolbow J., Belytschko T.: A finite element method for crack growth without remeshing. Int. J. for Num. Meth. in Engng. 46(1), 131-150 (1999).
55. Jovicic, G., Zivkovic, M., Sedmak, A., Jovicic, N., Milovanovic, D., Archives of Civil and Mechanical Engineering, Vol. 10, 3, pp. 19-35 2010.
56. Melenk J. M., Babuska I.: The partition of unity finite element method: Basic theory and applications. Comp. Meth. in App. Mech. and Engng. 39, 289-314 (1996).
57. Daux C., Moes N., Dolbow J., Sukumur N., Belytschko T.: Arbitrary cracks and holes with the extended finite element method, Int. J. for Num. Meth. in Engng. 48(12), 1741-1760 (2000).
58. Sukumur N., Prevost J.H., Modeling quasi-static crack growth with the extended finite element method, Part I: Computer implementation. Int. J. of Solids and Struct. 40, 7513-7537 (2003).
59. Giner E., Sukumar N., Tarancón J.E., Fuenmayor F.J., 2009. An Abaqus implementation of the extended finite element method. Engineering Fracture Mechanics 76, 347–368.
60. Golestaneh, A.F., Ali, A., Voon, W.S., Faizal, M., Mohammadi, M.Z., 2009. Simulation of fatigue crack growth in friction stir welded joints in 2024-T351 Al alloy. Suranaree Journal of Science and Technology 16, 35–46.

61. Golestaneh, A.F., Ali, A., Zadeh, M., 2009, Modelling the fatigue crack growth in friction stir welded joint of 2024-T351 Al alloy, Materials and Design 30, 2928-2937
62. Danijela Živojinović, Horia Dascau, Aleksandar Sedmak, Aleksandar Grbović, Integrity assessment of a structure made of two FSW T-welds, Proc. 6th International Scientific and Expert Conference TEAM 2014, Technique, Education, Agriculture & Management, Kecskemét, November 10-11, 2014, p. 456-459.
63. H.Dascau, D.Zivojinovic, A.Sedmak, V.Grabulov, Fatigue crack growth in friction stir welded AA 5083 joint by using the finite element method, Structural Integrity and Life, 2015, Vol. 15, No. 1, p. 33.

8 APPENDIX

A1. Force-deflection diagrammes

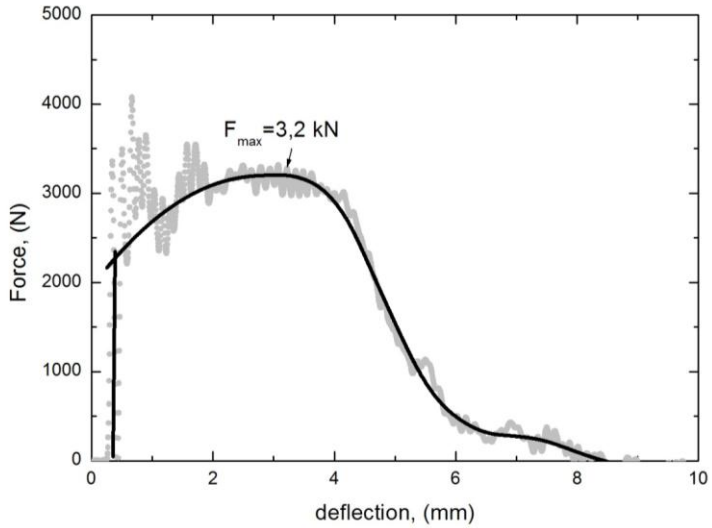

Figure 8—1 Force-deflection diagramme for sampe 1a (1 1 1)

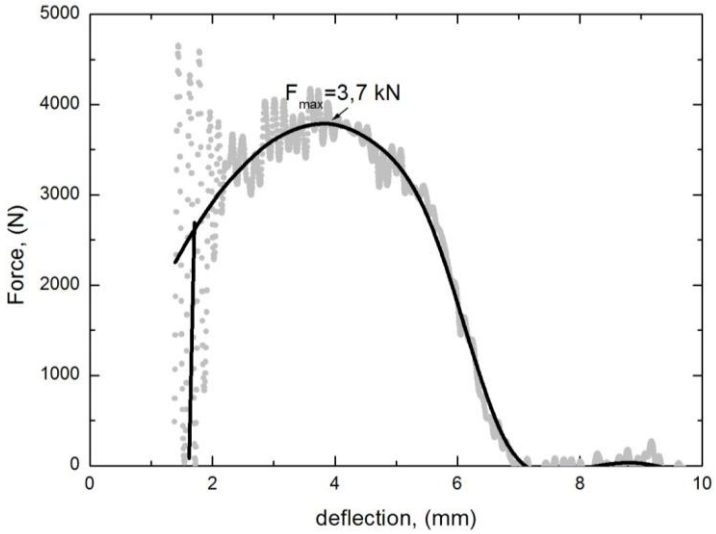

Figure 8—2 Force-deflection diagramme for sampe 1b (1 1 1)

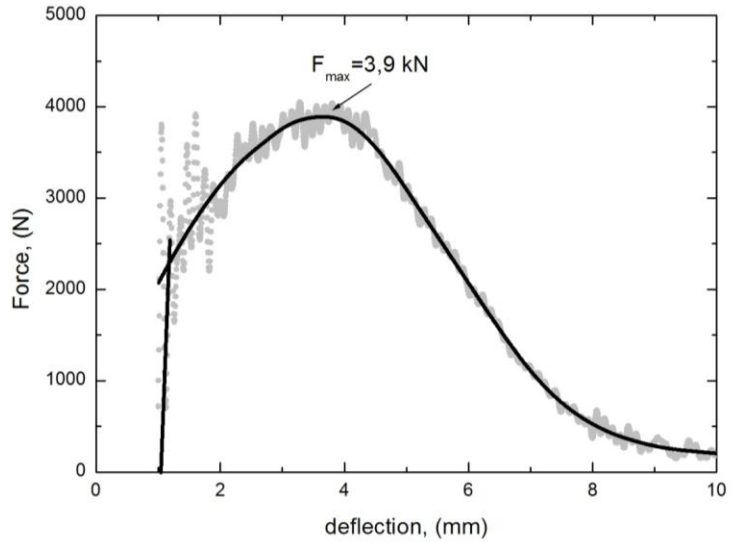

Figure 8—3 Force-deflection diagramme for sampe 2a (1 2 2)

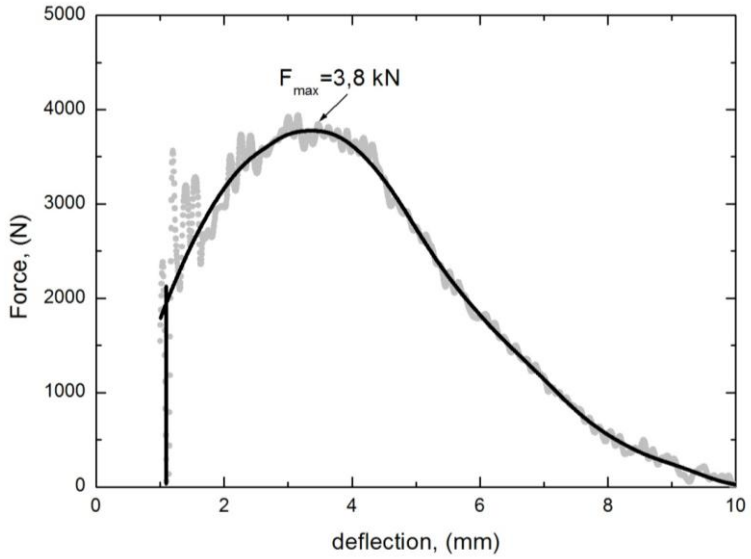

Figure 8—4 Force-deflection diagramme for sampe 2b (1 2 2)

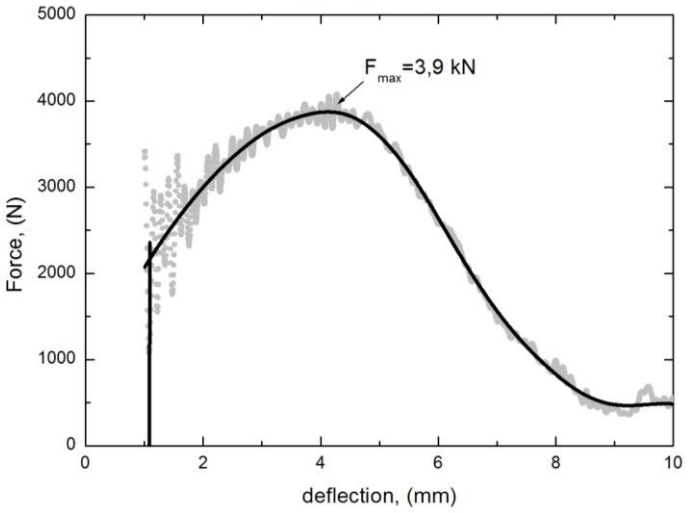

Figure 8—5 Force-deflection diagramme for sampe 3a (1 3 3)

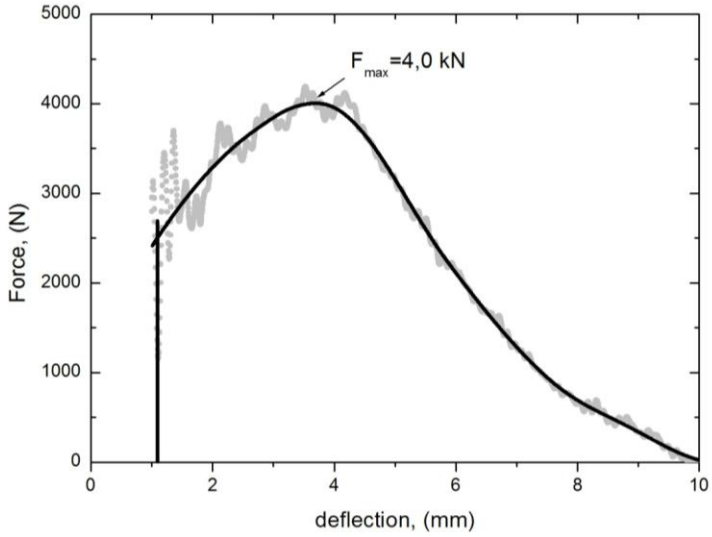

Figure 8—6 Force-deflection diagramme for sampe 3b (1 3 3)

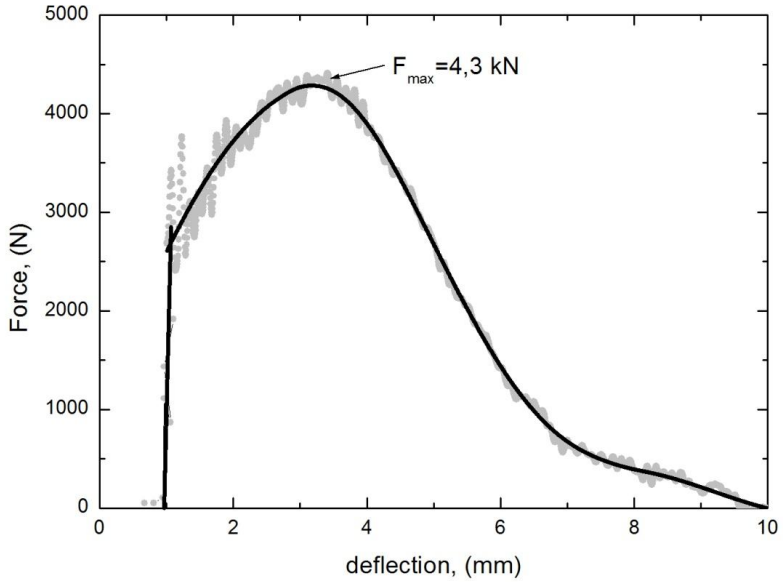

Figure 8—7 Force-deflection diagramme for sampe 4a (2 3 2)

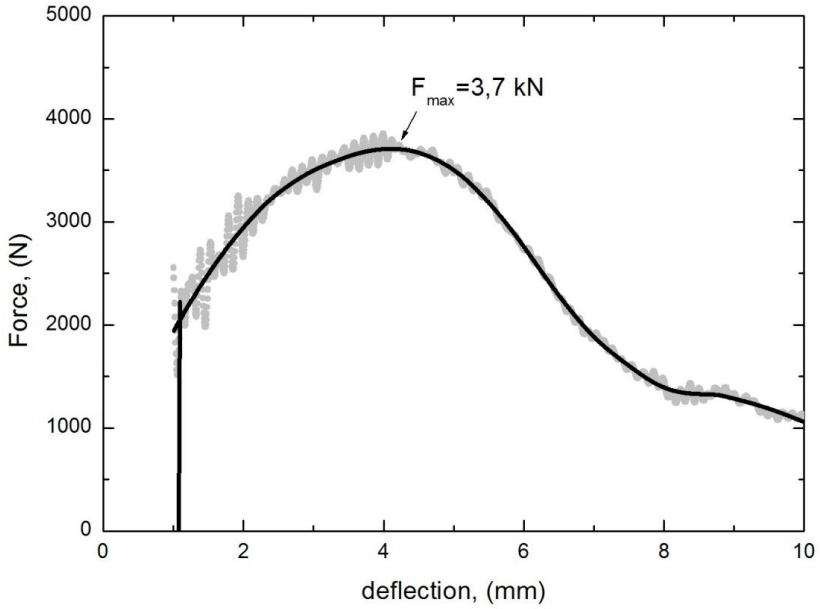

Figure 8—8 Force-deflection diagramme for sampe 4b (2 3 2)

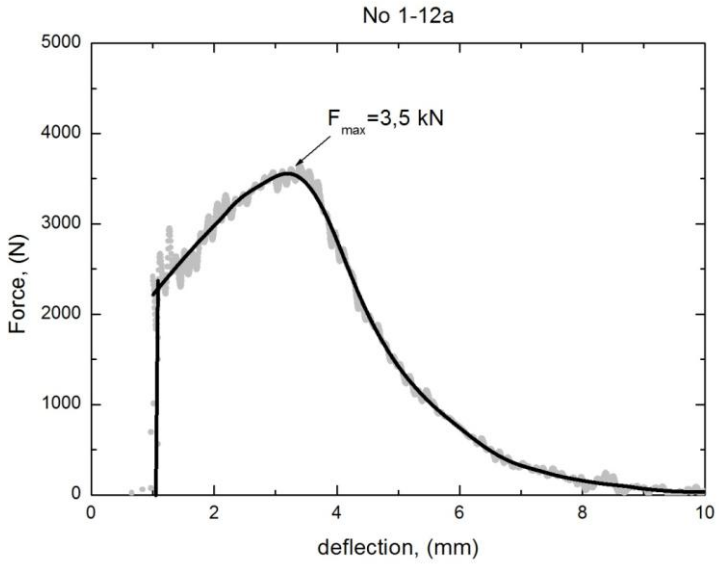

Figure 8—9 Force-deflection diagramme for sampe 5a (2 2 1)

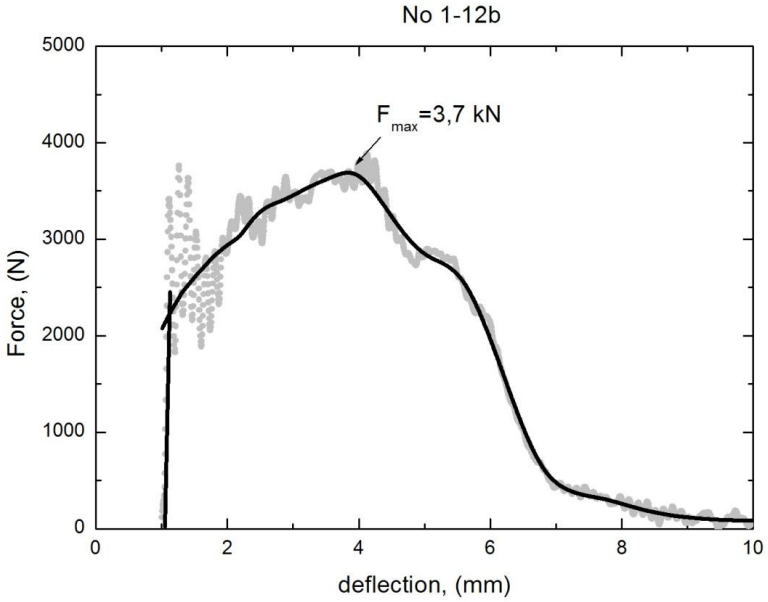

Figure 8—10 Force-deflection diagramme for sampe 5b (2 2 1)

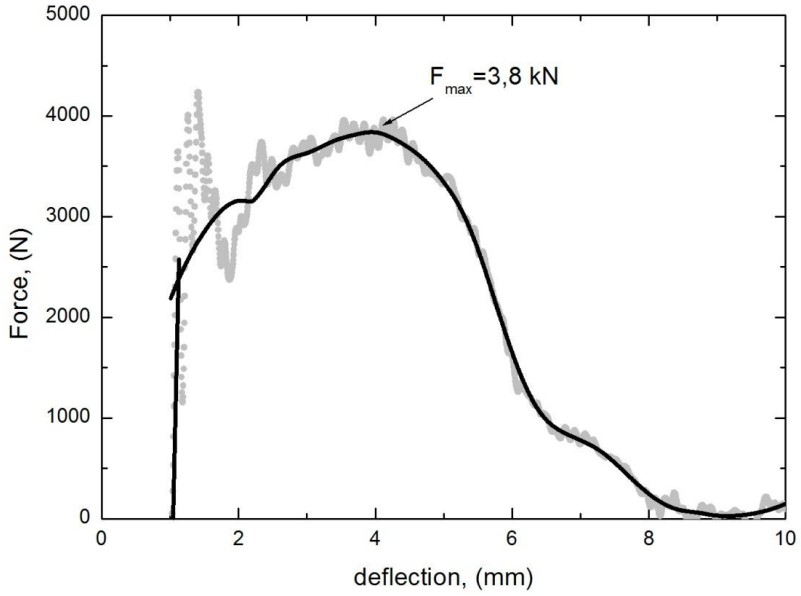

Figure 8—11 Force-deflection diagramme for sampe 6a (2 1 3)

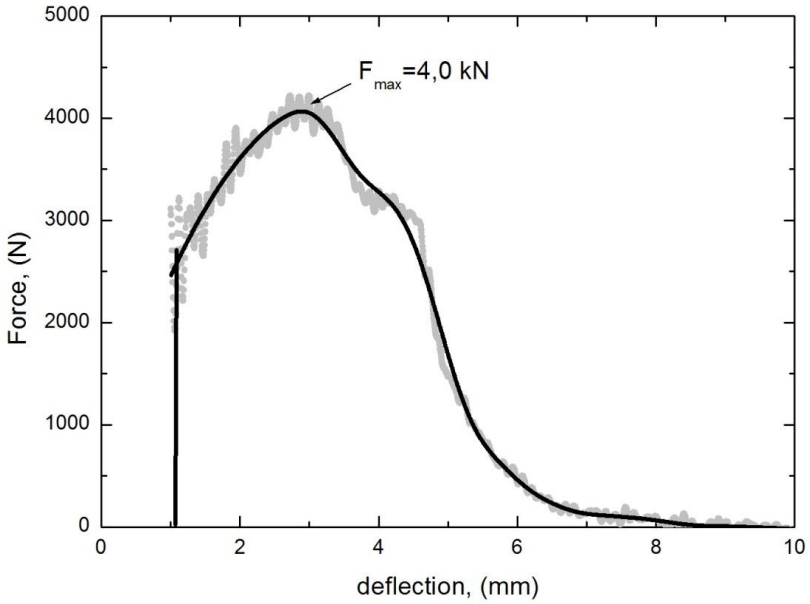

Figure 8—12 Force-deflection diagramme for sampe 6b (2 1 3)

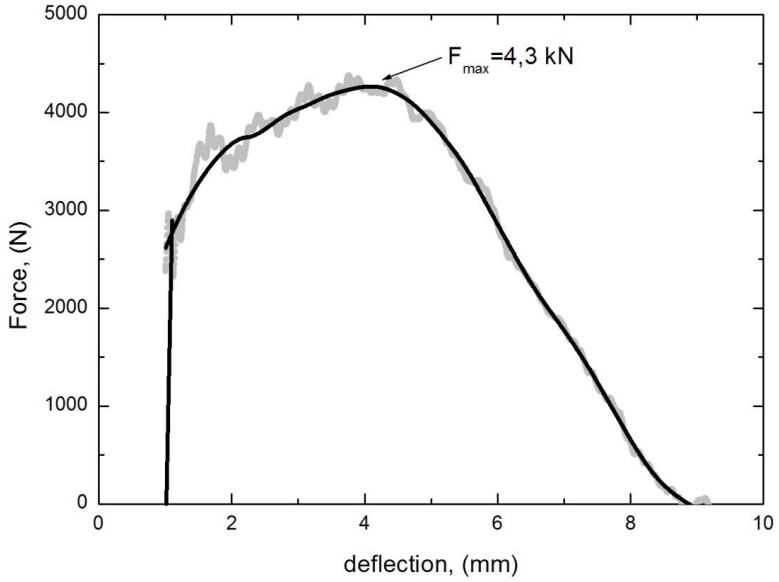

Figure 8—13 Force-deflection diagramme for sampe 7a (3 2 3)

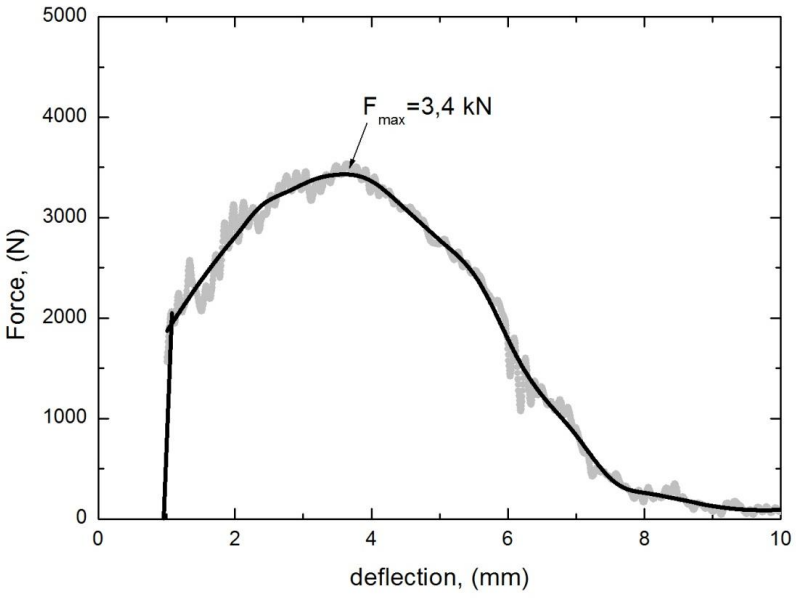

Figure 8—14 Force-deflection diagramme for sampe 7b (3 2 3)

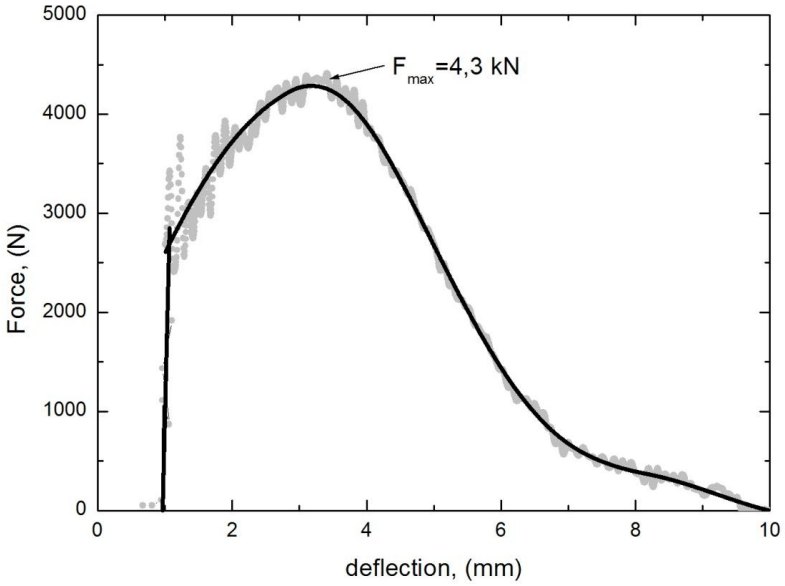

Figure 8—15 Force-deflection diagramme for sampe 8a (3 1 2)

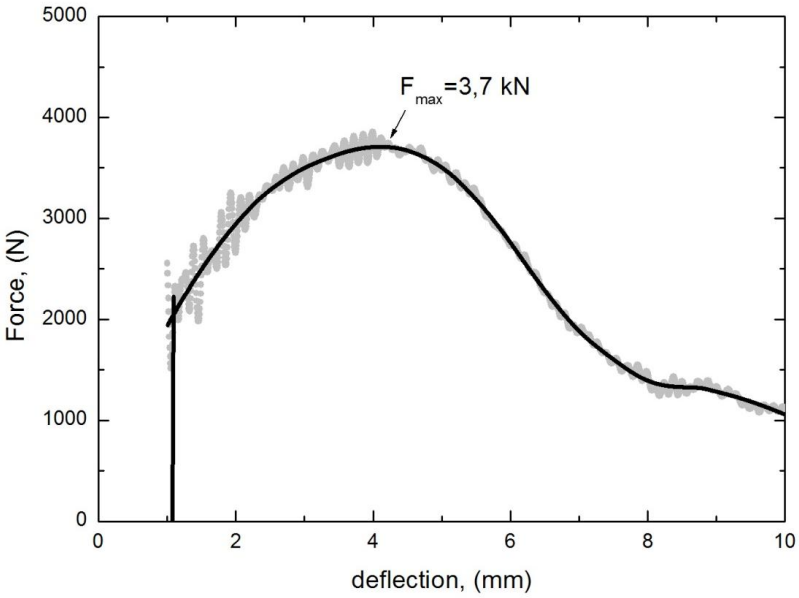

Figure 8—16 Force-deflection diagramme for sampe 8b (3 1 2)

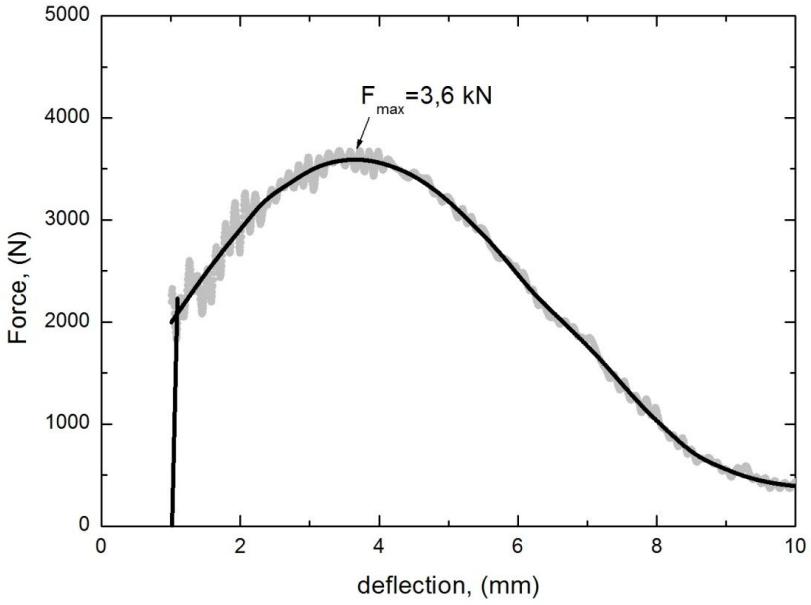

Figure 8—17 Force-deflection diagramme for sampe 9a (3 3 1)

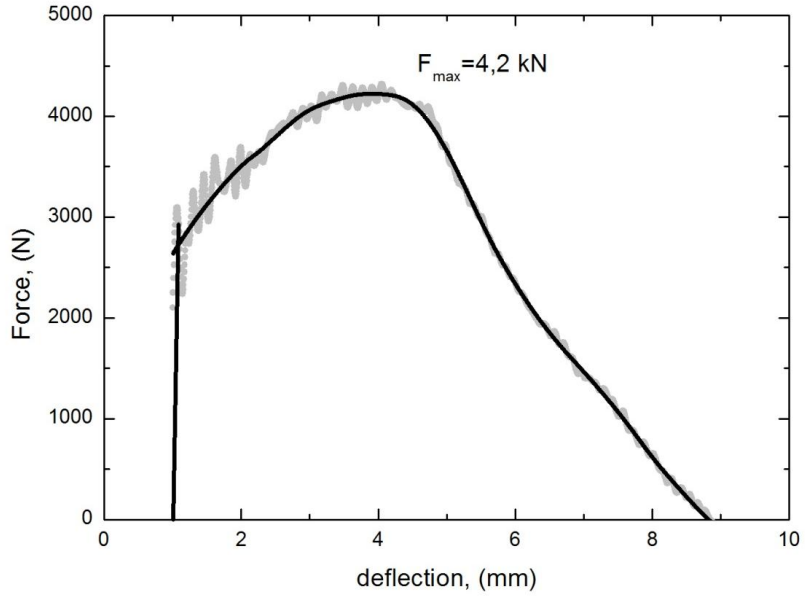

Figure 8—18 Force-deflection diagramme for sampe 9b (3 3 1)

A2. The J-Δa curves

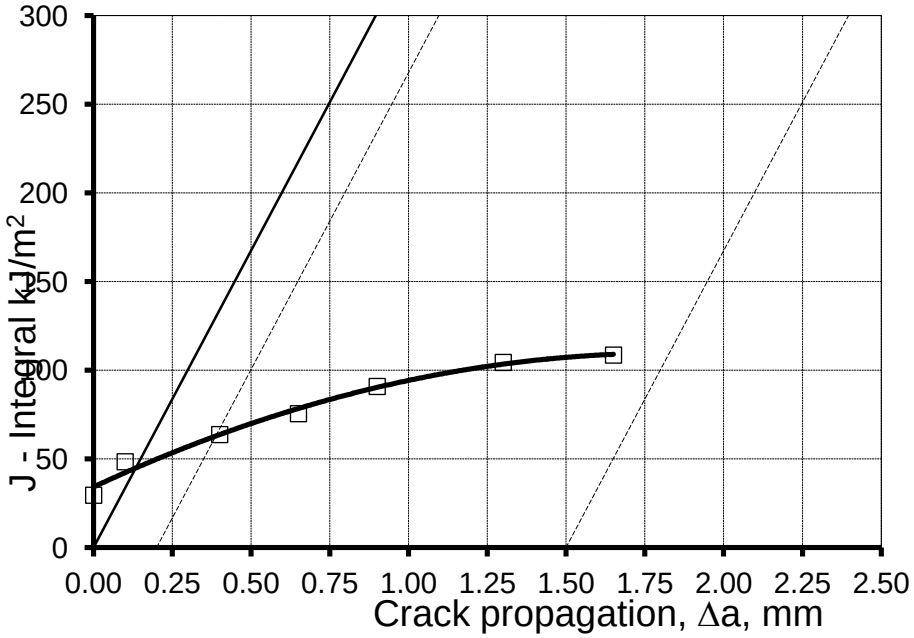

Figure 8—19 The J-Δa curve for sample 1a (1 1 1)

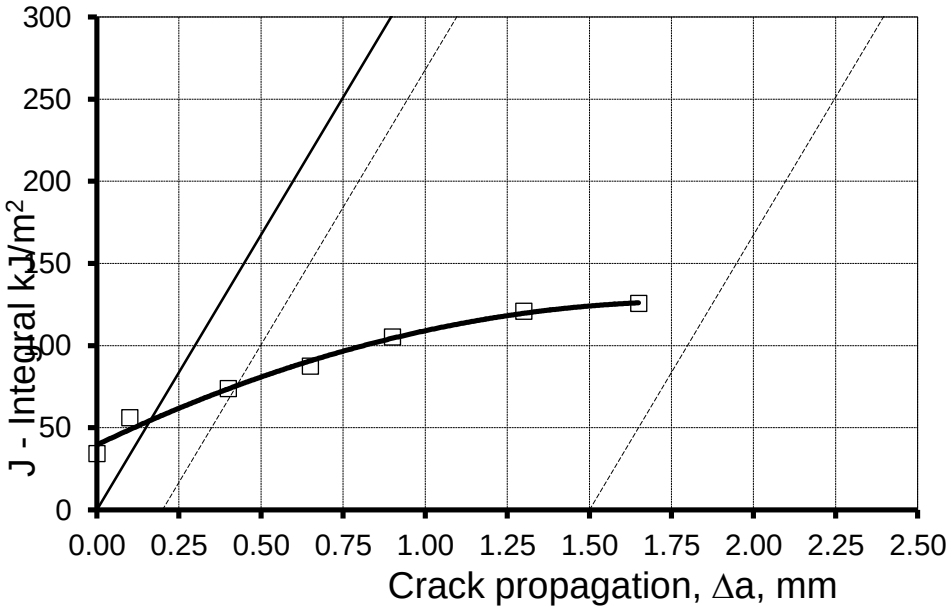

Figure 8—20 The J-Δa curve for sample 1b (1 1 1)

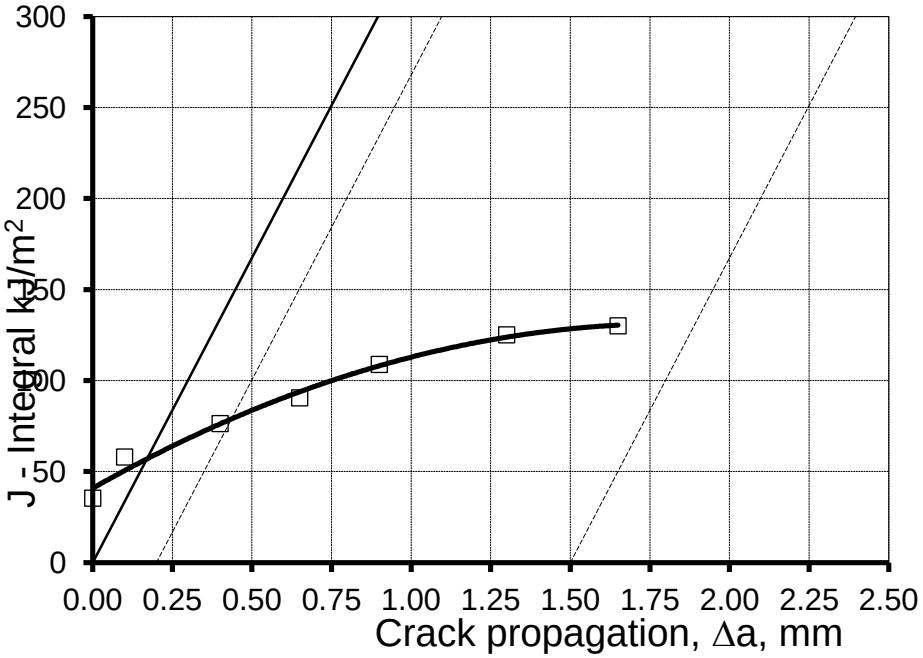

Figure 8—21 The J-Δa curve for sample 2a (1 2 2)

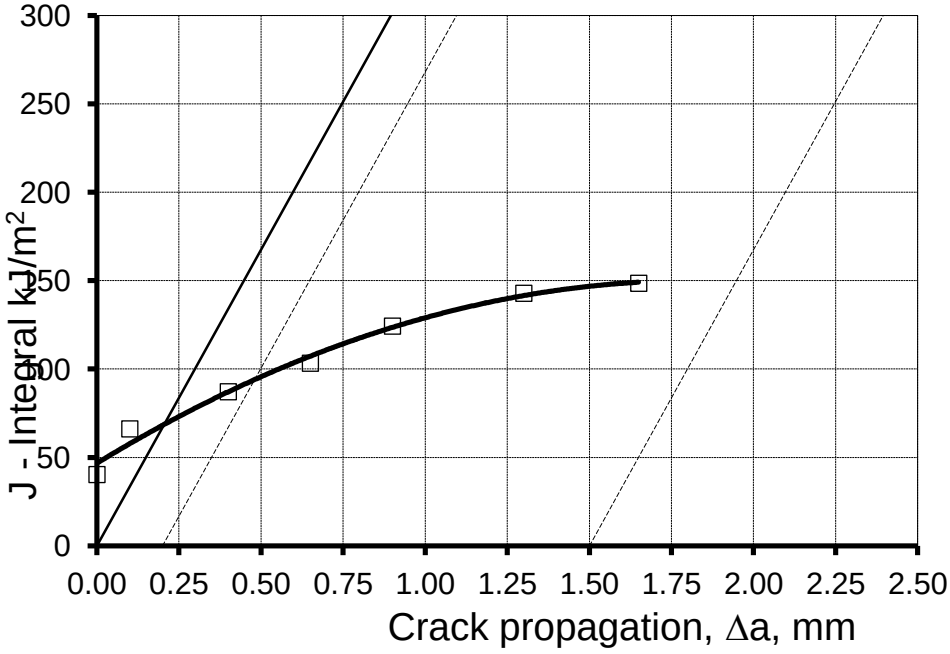

Figure 8—22 The J-Δa curve for sample 2b (1 2 2)

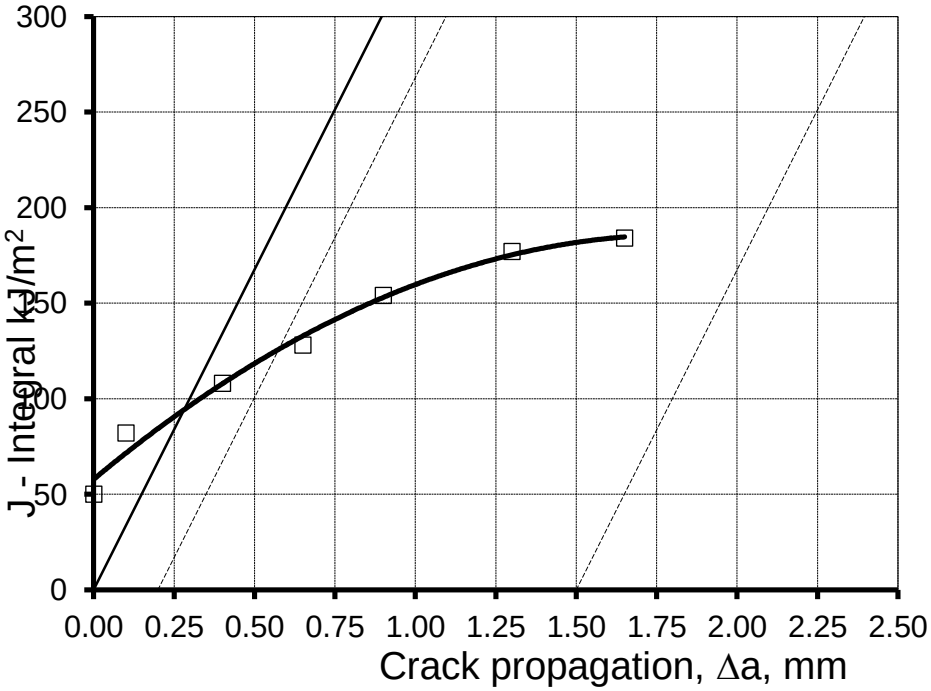

Figure 8—23 The J-Δa curve for sample 3a (1 3 3)

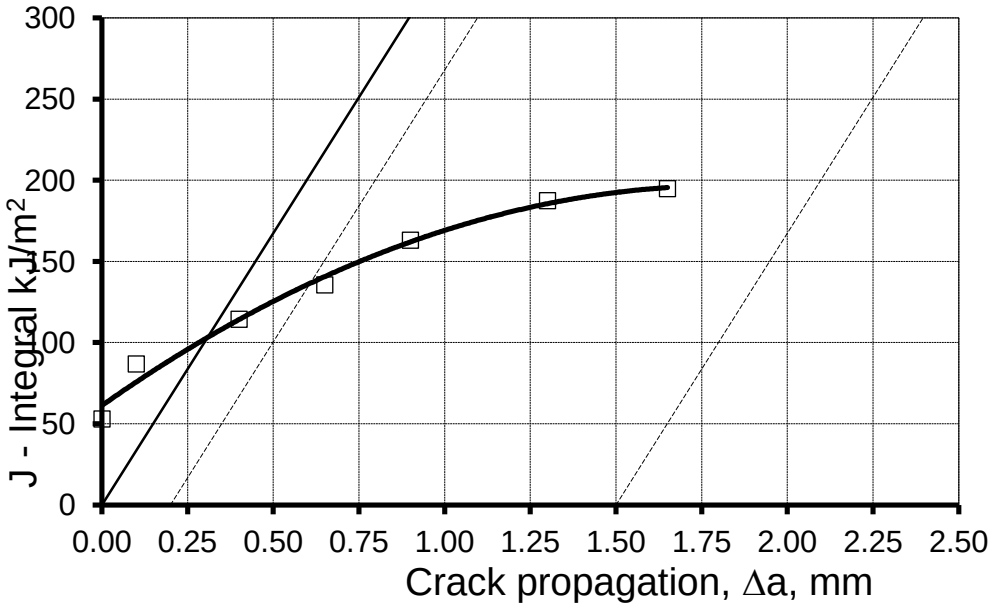

Figure 8—24 The J-Δa curve for sample 3b (1 3 3)

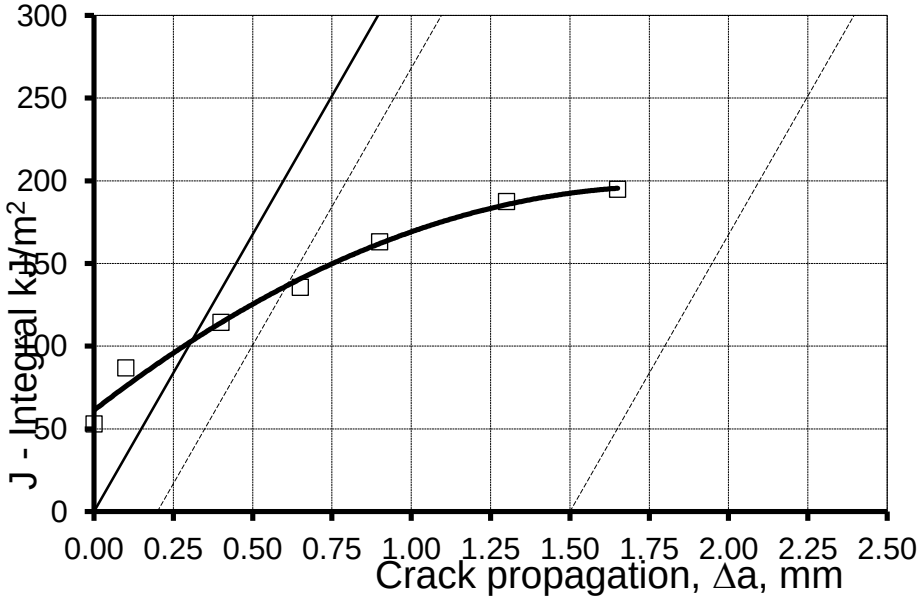

Figure 8—25 The J-Δa curve for sample 4a (2 3 2)

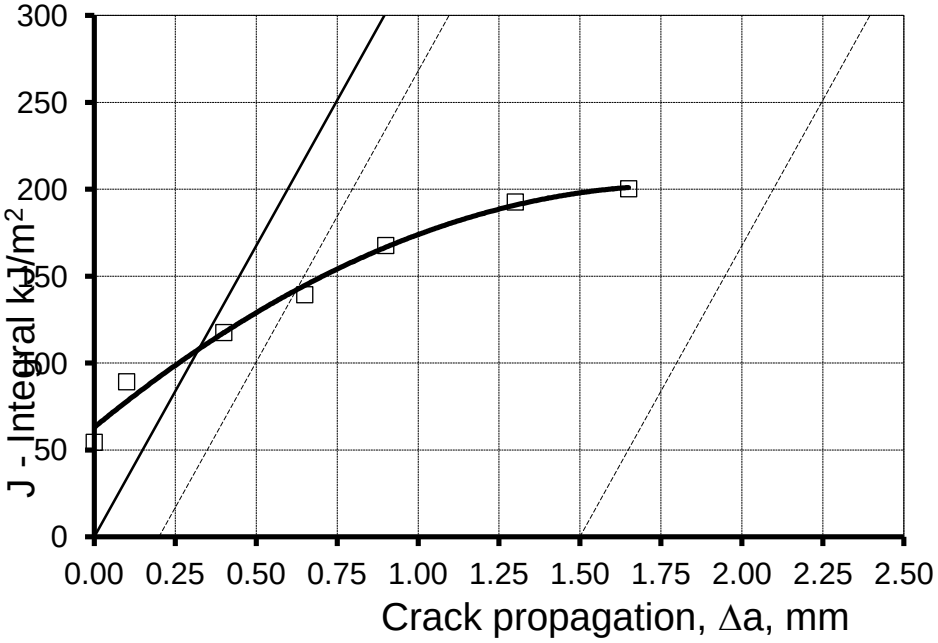

Figure 8—26 The J-Δa curve for sample 4b (2 3 2)

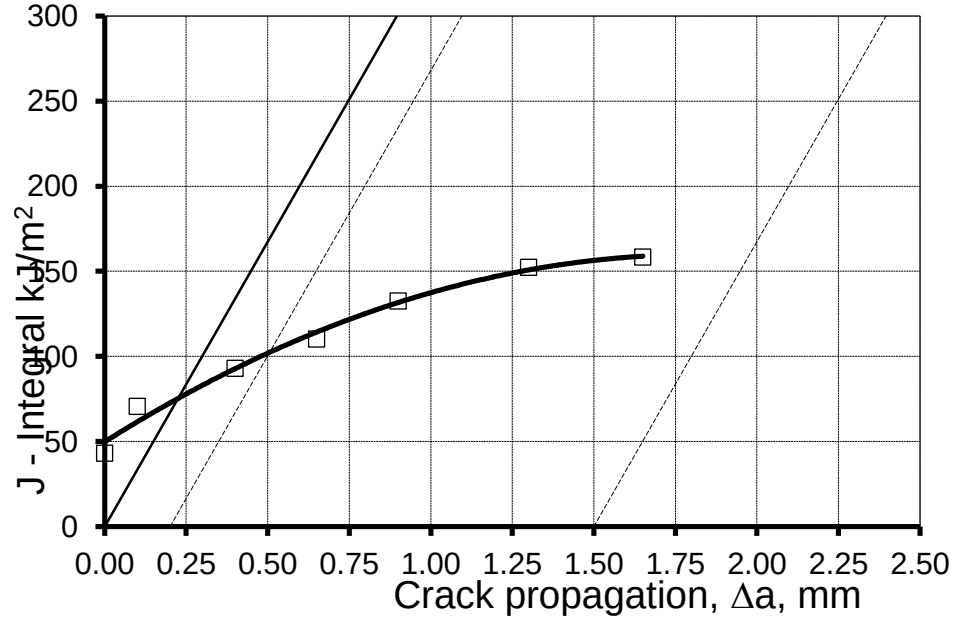

Figure 8—27 The J-Δa curve for sample 5a (2 2 1)

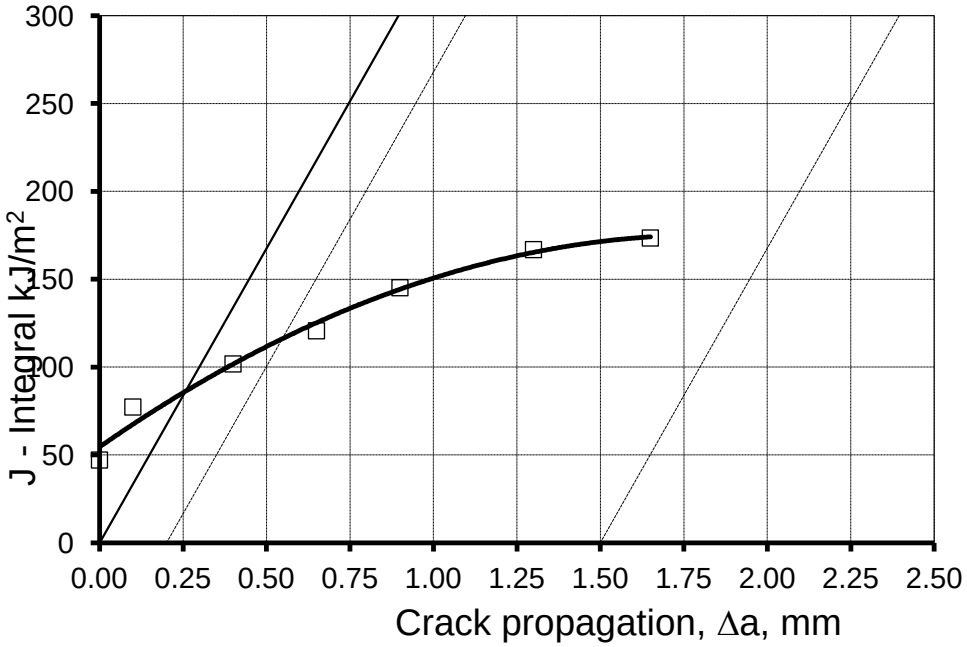

Figure 8—28 The J-Δa curve for sample 5b (2 2 1)

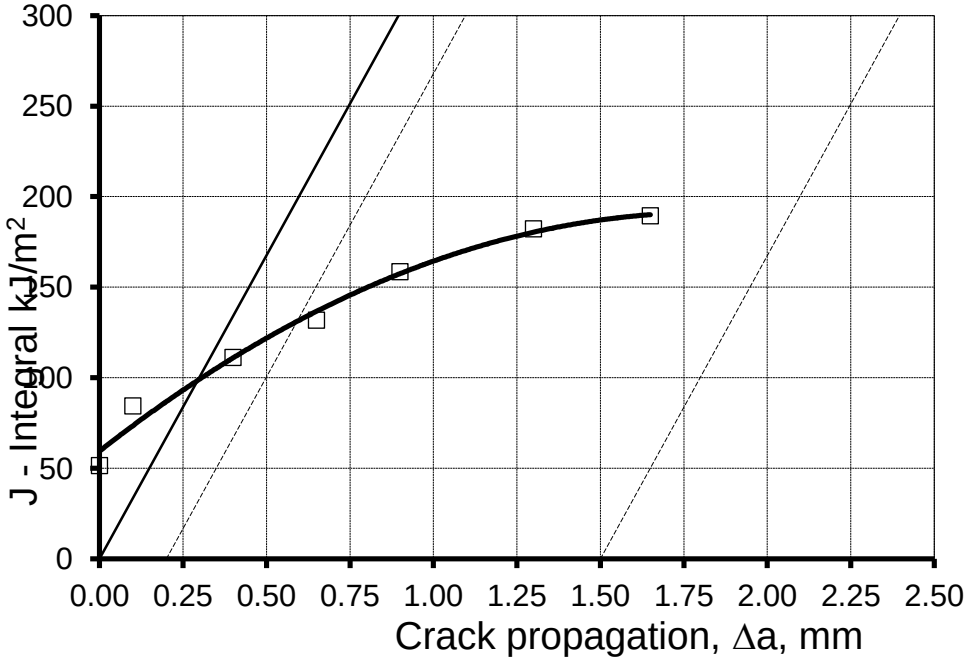

Figure 8—29 The J-Δa curve for sample 6a (2 1 3)

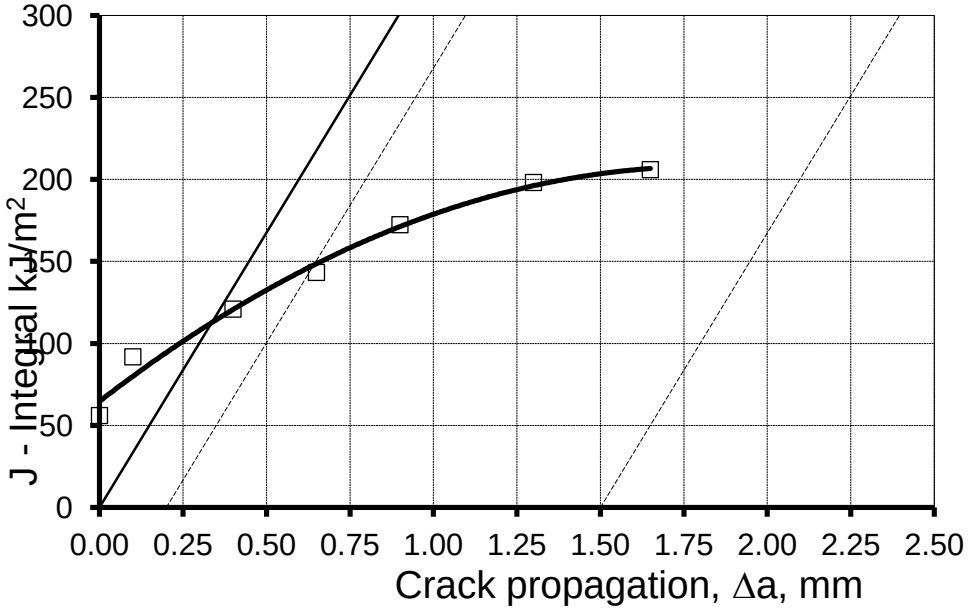

Figure 8—30 The J-Δa curve for sample 6b (2 1 3)

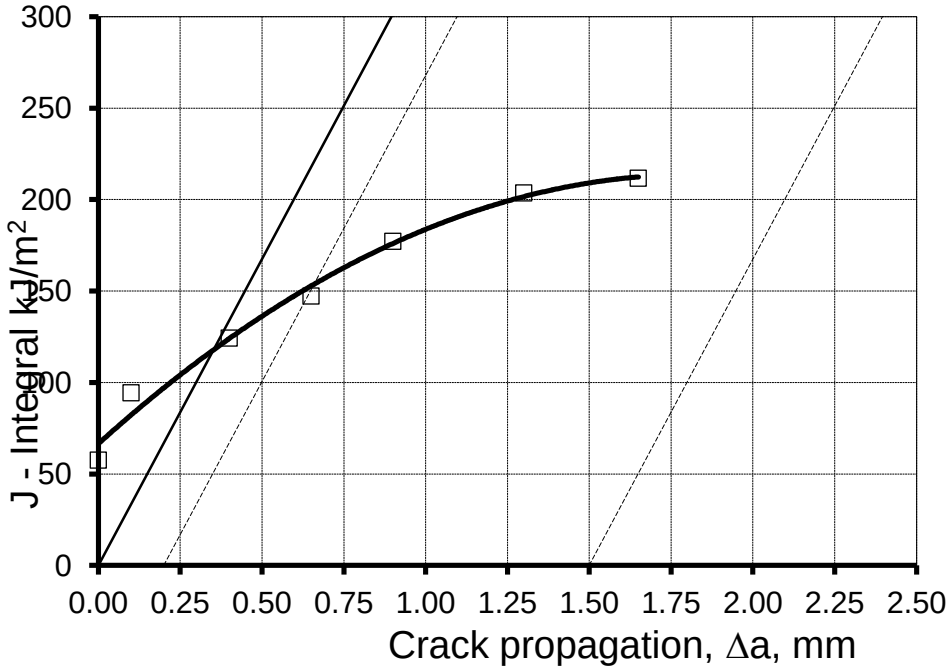

Figure 8—31 The J-Δa curve for sample 7a (3 2 3)

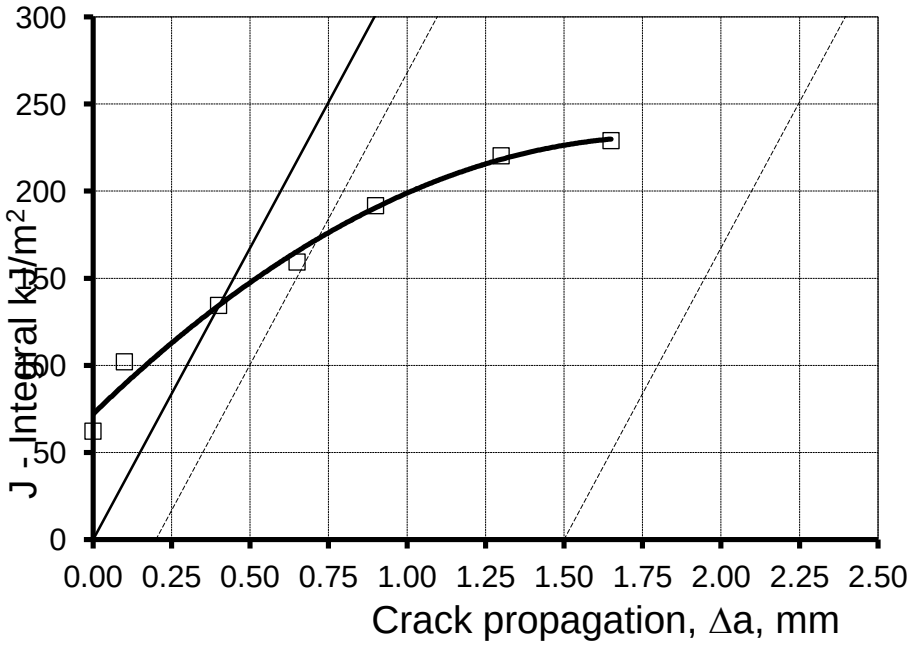

Figure 8—32 The J-Δa curve for sample 7b (3 2 3)

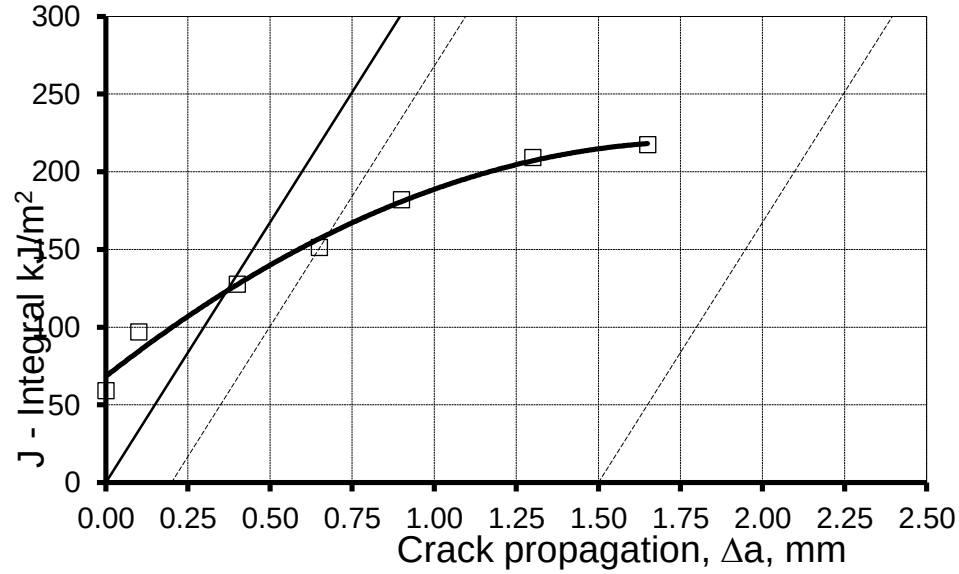

Figure 8—33 The J-Δa curve for sample 8a (3 1 2)

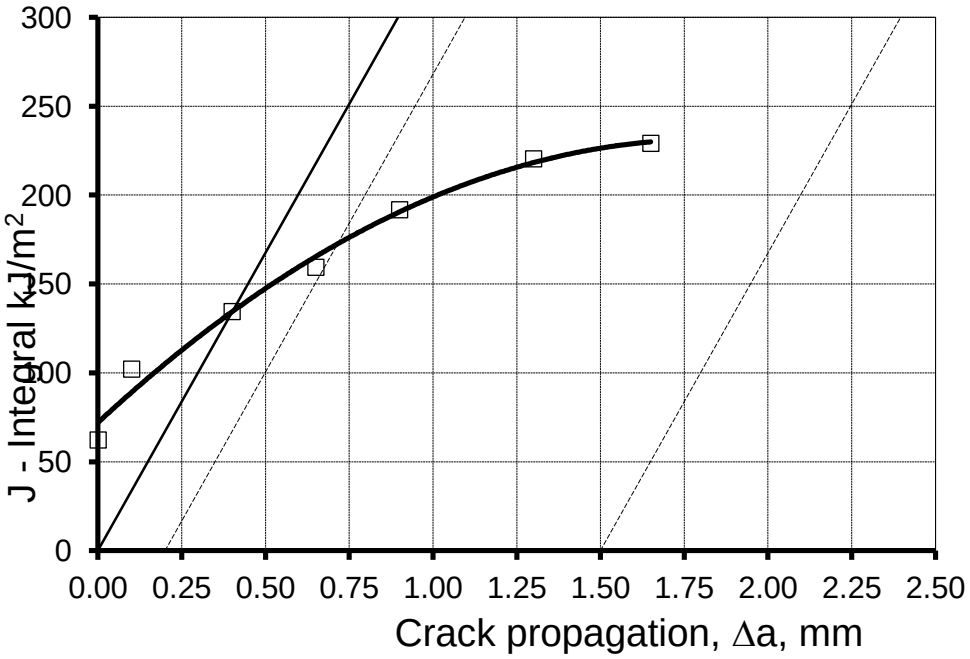

Figure 8—34 The J-Δa curve for sample 8b (3 1 2)

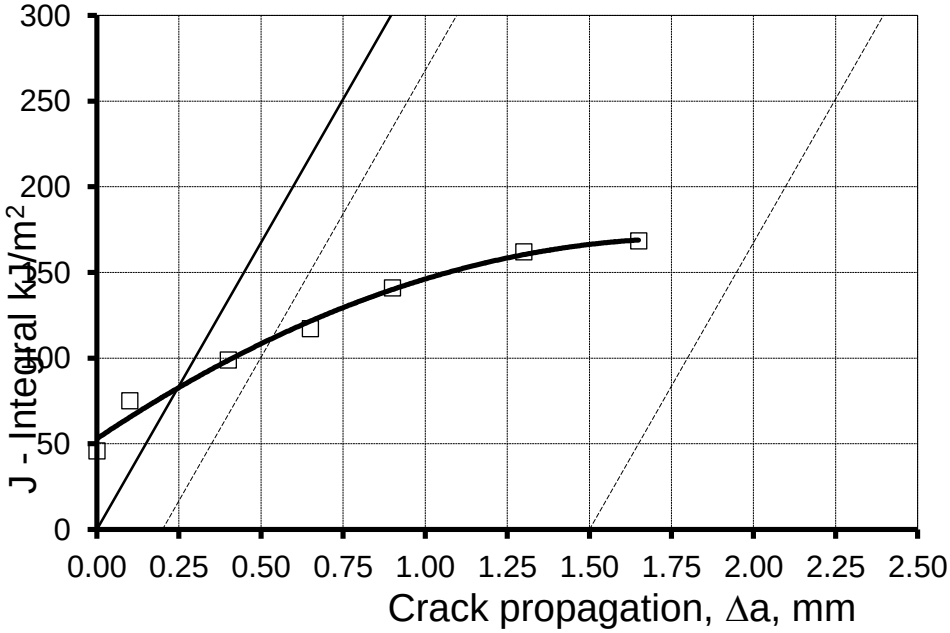

Figure 8—35 The J-Δa curve for sample 9a (3 3 1)

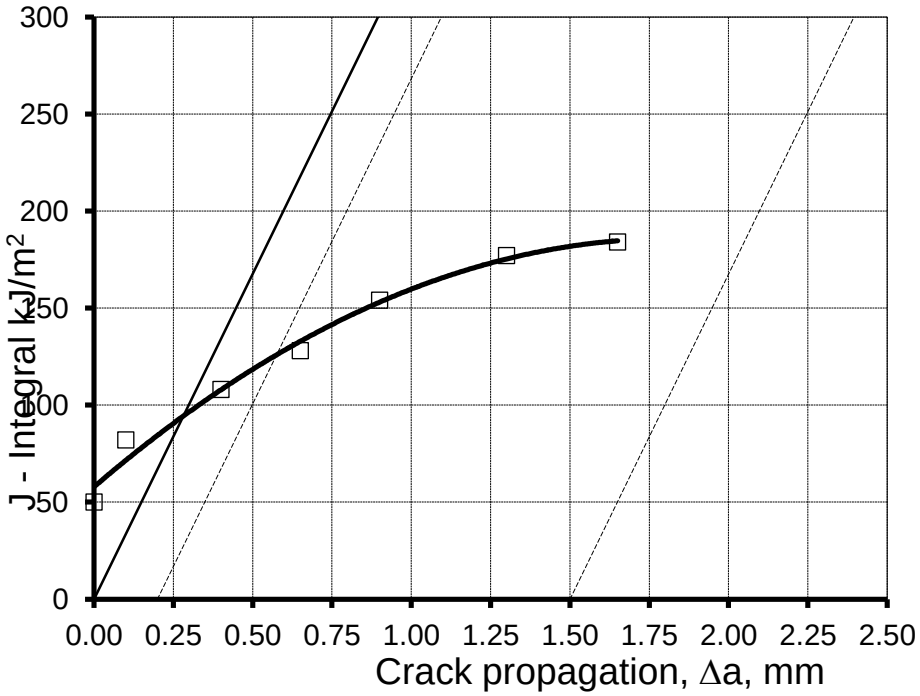

Figure 8—36 The J-Δa curve for sample 9b (3 3 1)